Unifying laminar and turbulent dynamics of plumes

Daniel Robert Ward

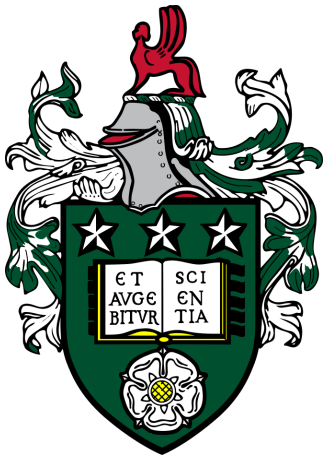

Submitted in accordance with the requirements for
the degree of Doctor of Philosophy

The University of Leeds
EPSRC Centre for Doctoral Training in Fluid Dynamics

April 2022

Declaration of Authorship

The candidate confirms that the work submitted is their own, except where work which has formed part of jointly authored publications has been included. The contribution of the candidate and the other authors to this work has been explicitly indicated below. The candidate confirms that appropriate credit has been given within the thesis where reference has been made to the work of others.

Chapters 2, 3 and 5 contain work from jointly authored 'A universal description of plume instability'. Authors: Daniel R. Ward, Dr. Samuel S. Pegler. Journal of Fluid Mechanics, in preparation.

Chapter 4 contains work from jointly authored 'Unified laminar-turbulent dynamics of plumes in a stratification'. Authors: Daniel R. Ward, Dr. Samuel S. Pegler, Dr. Som Dutta. Details tbc., in preparation.

Development of the theoretical and numerical models, direct numerical simulations, and data analysis is attributable to Daniel R. Ward. Supervision of the research with suggestions on lines of enquiry and research techniques, manuscript re-vision, and suggested edits of the paper were carried out by Dr. Samuel S. Pegler. Consultation on numerical simulation setup and techniques in Nek5000 were provided by Dr. Som Dutta.

Acknowledgements

First and foremost, I would like to thank my lead supervisor Sam Pegler for his continuous support, encouragement, and unwavering enthusiasm throughout the duration of my PhD. Without you this thesis would probably have looked very different.

Thanks also to David Ferguson for his support to pursue the topics I wished, despite the work gradually and inexorably moving away from his field of expertise, and for being a grounding influence when Sam and I got carried away.

A big thank you also goes to Som Dutta, my unofficial supervisor, who hosted me at his home in Utah while on research placement and was always happy to field my questions about Nek5000.

I am grateful to EPSRC for providing me the funding to undertake this research as part of the Leeds CDT in Fluid Dynamics. The benefit of undertaking my PhD as a part of the CDT cannot be overstated, so thank you also to Claire Savy and Peter Jimack for providing support and guidance. Despite the lapse over the last two years due to 'unforeseen global circumstances', the cohort structure and camaraderie of the CDT was crucial in contributing to my success and my enjoyment of the process. Thanks also to all the friends I've made throughout my time in Leeds, both in and outside of university. I look forward to seeing you all again soon.

Finally, thank you to my family for always supporting me in my endeavours, even if sometimes it takes a bit longer than expected.

Abstract

Buoyant plumes are widespread physical phenomena, present across a large range of scales, from the plume generated by a candle to a mantle plume beneath the crust of the Earth, and spanning laminar to fully turbulent flow. In its most basic form, a plume is the vertical transport of heat emanating from a buoyancy source. Despite the ubiquity of plumes and their role in heat and mass transport, many aspects of their dynamics are still not fully understood.

In the literature, plumes are often separated into laminar and turbulent regimes and are yet to be combined into a cohesive theory of plume evolution and structure. In this thesis, I perform a theoretical and numerical analysis of pure plumes generated by a localised point source of heat in order to unify these separate theories in a description of a hybrid laminar-turbulent plume. The governing equations for a plume are shown to be dependent on only one dimensionless parameter, the Prandtl number Pr, which is the ratio of kinematic viscosity ν to thermal diffusivity κ. Using direct numerical simulations (DNS) combined with scaling analysis, I establish some universal properties of pure plumes. Following the laminar regime, the height at which instability occurs, hereafter referred to as height to instability, for the case $Pr = 1$, is found to be $z^* = f(Pr)(\kappa^3/F_0)^{1/2}$, where F_0 is the source buoyancy flux, and $f(Pr)$ is a Prandtl number dependent dimensionless prefactor. The turbulent regime is described using similarity scalings and a virtual origin $z_0 \neq z_*$ is found, implying that the transition region exists over a nonzero spatial range.

Expanding on this work, further DNS are undertaken to derive a unified laminar-turbulent theory of a plume in an unstratified environment emanating from a point source over a range of Prandtl numbers. The height to instability z^* is found to increase sublinearly with Pr and a formula for interpolating the height to instability within the range $Pr \in [0.1, 2.0]$ is fitted to the results.

My investigation into developing a unified laminar-turbulent theory of plume rise from a point source is further expanded by introducing a linear stratification to the background. This introduces another length scale to the problem and the relationship between height to instability and maximum rise height is investigated. I performed DNS of plumes across a wide spectrum of Reynolds numbers and developed a simplified theory of low-Re plumes, resulting in excellent agreement with the predictions of the DNS. Interestingly, the results

demonstrate a non-monotonic relationship between rise height and Reynolds number, with a global maximum at $Re \approx 1500$.

Finally, the unstratified results are applied to the transport (e.g. of pathogens) in the built environment by local sources of heat. A hybrid laminar-turbulent theory of particle transport in rooms is developed using the results of height to instability. Remarkably, a strongly non-monotonic relationship between transport rates of particles and the initial buoyancy flux, with two turning points, is discovered.

Contents

List of Figures

List of Tables

Chapter 1

Introduction

Contents

Buoyant plumes arise throughout the natural world, across a wide range of scales. In the atmosphere, erupting volcanoes produce buoyant plumes, the largest of which transport ash and smoke on a global scale (Woodhouse et al., 2013). Beneath the Earth's surface, mantle plumes transport heat and result in the movement of continents (Loper, 1991). In the ocean, sea-floor vents and volcanic eruptions produce plumes that can influence ocean currents and spread biota (Speer & Rona, 1989; Pegler & Ferguson, 2021) and deep-sea oil spills can lead to the spread of contaminants (Fabregat Tomàs et al., 2016). On smaller scales, smoke-stacks at power stations and factories outputting pollutants (Hewett et al., 1971), and forest fires producing ash and smoke (Henderson et al., 2008), are present across the planet, often in areas near to human habitation (Liu et al., 2014). On yet smaller scales, the heat

generated by a candle (Maxworthy, 1999), computer, or a human (Craven & Settles, 2006) warms the air above and generates convection, resulting in a plume with impact on ventilation in rooms and the potential transmission of airborne pathogens (Bhagat et al., 2020). As plumes are so widespread, it is not surprising that plumes have been researched extensively, using techniques such as physical observations, laboratory experiments, mathematical modelling, and more recently, computationally intensive numerical simulations. Despite extensive work on plumes covering the best part of the last century, there still remain numerous open questions. For example: What causes a plume to transition from laminar to turbulent flow, and where does this transition happen? What effect do material and environmental properties have on plume flow? Under what conditions can a plume be said to be independent of fluid viscosity? How does the viscosity of a plume in a stratified fluid affect the rise height? The work in this thesis addresses these questions by making use of scaling analyses, simplified theories, and direct numerical simulations (DNS) of the Navier-Stokes equations.

A plume is a fluid-dynamical phenomenon that occurs whenever a maintained source of buoyancy results in a rising region of fluid upward and away from the buoyancy source. It is a fundamental problem in fluid dynamics and a clear example can be readily witnessed in the smoke trail above a recently extinguished candle. The development and behaviour of a plume is dependent on the relationship between its source conditions and the environment it is in. There exist a number of different parameters that have varying effects on the flow, for example the size, velocity, and temperature of the source, background effects, and material properties such as viscosity and thermal diffusivity. Many plumes in nature occur in stratified environments. For many plumes in a stratification, there exists a laminar flow region near to the source behaving similarly to that of a plume in an unstratified environment. In some scenarios the size of the laminar region is negligible or not present due to external disturbances. As laminar flows transport heat much faster than turbulent flows, it is important to understand the behaviour of this region, to know in which circumstances it will be present, and to know how large it will be. In scenarios such as the transport of heat above a lit candle in a room, the laminar region can be a significant portion of the flow, as illustrated by the schlieren image in figure 1.1. Laminar plumes have relevance in the study of natural ventilation and in particular, due to recent events (i.e. the global Covid-19 pandemic), the spread of airborne pathogens in indoor environments

Figure 1.1: A schlieren image of the laminar to turbulent transition of a plume generated by a candle flame. The image illustrates the significance of the laminar region and the transition to turbulence. The image was made using a 1-metre-diameter schlieren mirror by Dr. Gary Settles and is licensed under the Creative Commons Attribution-Share Alike 3.0 Unported license (CC BY-SA 3.0).

(Bhagat et al., 2020). It is important to understand the behaviour of the laminar as well as the turbulent region, and the transition between them, as it can have a large impact when flows become more complicated, for example when the environment is stratified.

Modelling plumes from a point source of heat reduces the complexity of the problem, and can ensure the plume is 'pure', with neither a momentum deficit (lazy) or a momentum surplus (forced) (Morton & Middleton, 1973). In an unstratified environment, there is an initial region in which the diffusive heat source results in a movement of fluid vertically, resulting in the development of a laminar plume. The plume will continue to rise in a slender stem until it reaches a critical height at which it transitions to turbulence, after which the turbulent plume will continue to rise indefinitely. In this case, both laminar and turbulent regimes admit separate similarity solutions (Zeldovich, 1937). In a stratified ambient, however, there exists a neutral buoyancy level (NBL) where the buoyancy of the plume fluid becomes zero and beyond which the resultant forces on the fluid motion are no longer upward but downward

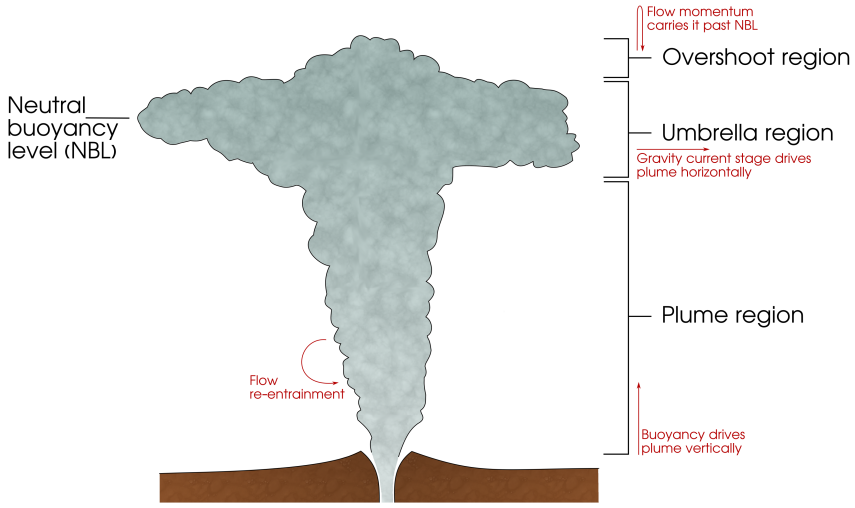

Figure 1.2: Illustration of a volcanic plume in a stratified ambient. In this example the plume is essentially turbulent from the offset. There is a turbulent plume stem, until the effect of the stratification becomes dominant and the direction of buoyancy reverses. The positive momentum at the neutral buoyancy level (NBL) results in an overshoot and subsequently the flow moves laterally outwards and forms an 'umbrella' region.

and horizontal. This causes a reversal in buoyancy and the flow subsequently spreads radially outwards along the NBL, forming a neutrally buoyant gravity current or intrusion (known as an umbrella region in volcanology). This behaviour is illustrated in figure 1.2 using the illustration of a volcanic eruption (although an initial laminar region does not exist for a volcanic eruption, the image is just used here for illustration). In the stratified case there are two possible scenarios. The transition to turbulence can occur lower than the NBL whereby the plume transitions to turbulence in the stem phase and reaches the NBL as a turbulent flow. Alternatively, the transition to turbulence can occur after the flow reaches the NBL whereby the flow will reach the NBL as a laminar flow.

There are a number of different ways to study the behaviour of a plume. In the case of something large like a plume generated by a volcanic eruption, travel to the volcano is required to take readings, observe the behaviour, and understand the effect on the environment. Direct observational studies can be challenging, however. If one wanted to study a large volcanic eruption, for example, it may be necessary to wait months or years before an eruption. If results obtained are applied to another volcanic eruption, differing buoyancy flux, wind profiles, elevation, fluid density and other parameters

between them may render predictions inaccurate. Despite these limitations, observations are critically important for the verification of numerical models.

One could also generate plumes experimentally in a laboratory (e.g. Shabbir & George, 1994; Kaminski & Jaupart, 2003; Xue et al., 2019). This requires certain assumptions in order to make observations. Length scales in a laboratory will never reach those present in a flow as large as a volcanic eruption or a mantle plume, and hence certain dimensionless numbers, such as the Reynolds number, will never be comparable to the physical counterpart. Other challenges can include accounting for the effect of the experimental setup on the plume, such as the fluid tank walls and the nozzle details, and taking flow measurements without disrupting the flow. Despite these challenges, laboratory experiments result in physically correct flow data and are vital for the verification of simple models and numerics.

Another way of studying a plume is by solving simplified differential equations, often making use of scaling arguments to make simplifying assumptions, to result in macroscopic descriptions of the flow. Despite these assumptions, comparisons to observations, often using empirically determined parameters, can result in extraordinarily accurate predictions of bulk flow properties, such as width-averaged fluxes or plume rise height in a stratified environment. An overview of the models used to make these predictions is presented in section 1.1. This method, of solving simplified differential equations, combined with that of making observations of the world and experiments, was the main way in which plumes were modelled until recent technological advances have resulted in large amounts of computing power being made available to scientific researchers.

This recent increase in computing power has made solving large problems with high-order numerical methods feasible. For some small parameter h, which for instance can be the grid size or time step, a numerical method has order p if the numerical error is bounded by Ch^p, for some constant C. Direct numerical simulations (DNS), one of the most computationally intensive forms of numerical fluids research, can be used to solve high-order methods and resolve every detail of a flow, down to the smallest eddy, on a numerical mesh. While requiring significant computing power, this technique enables the researcher to study the problem of a plume in its entirety, resulting in complete information about flow fields. This is the main technique used in this thesis,

along with scaling analysis, simpler numerical models, and comparisons to the work of previous authors.

In this chapter, the different techniques that have been used to study plumes in the past are discussed by giving a comprehensive overview of the literature on the topic. In section 1.1, previous work to create simplified theoretical models of both laminar and turbulent plumes is reviewed. Section 1.2 discusses high order computational methods and techniques for studying plume dynamics, and finally section 1.3 addresses open research questions and lays out an overview of the rest of this thesis.

1.1 Modelling plumes

The full motion of a plume, from laminar to turbulent flow and from unsteady development to a steady state, can be described using the Navier-Stokes equations (Navier, 1827; Stokes, 1849). The Navier-Stokes equations are a set of partial differential equations which describe the motion of fluids. They consist of conservation of momentum and mass equations, and can be combined with a conservation of temperature equation to model fluid flow and heat transfer in a wide range of applications. They are given by

$$\frac{D\boldsymbol{u}}{Dt} = -\frac{\boldsymbol{\nabla} p}{\rho_0} + \nu \nabla^2 \boldsymbol{u} + g\beta T \hat{\boldsymbol{z}}, \tag{1.1a}$$

$$\boldsymbol{\nabla} \cdot \boldsymbol{u} = 0, \tag{1.1b}$$

$$\frac{DT}{Dt} = \kappa \nabla^2 T, \tag{1.1c}$$

where $\boldsymbol{x} = (x, y, z)$ is the position vector, t is time, $\boldsymbol{\nabla}$ is the gradient operator, $\boldsymbol{u}(\boldsymbol{x}, t) = (u, v, w)$ is the fluid velocity, p is the fluid pressure, ρ_0 is a reference density, ν is the kinematic viscosity, $T(\boldsymbol{x}, t)$ is the temperature difference from the ambient, κ is the thermal diffusivity, β is the coefficient of thermal expansion, and g is acceleration due to gravity. In the equations above, the Boussinesq approximation has been made, i.e. that the density of the fluid does not vary significantly from the reference value ρ_0. This results in the density (in this case the temperature T) appearing only in the forcing term of the momentum equation (1.1a).

In order to model a plume emanating from a point source, the solution

to the equations above is considered in the semi-infinite region $z \geq 0$ subject to no-slip and insulation conditions at $z = 0$, given by

$$\boldsymbol{u}(x, y, 0, t) = \mathbf{0}, \qquad \frac{\partial T}{\partial n}(x, y, 0, t) = 0, \tag{1.2}$$

respectively. In the far-field of the domain (encompassing both the limits of $x, y \to \infty$ for $z \geq 0$ and $z \to \infty$), it is assumed that the fluid is stagnant and that the temperature is given by the ambient value, as specified by

$$\lim_{R \to \infty} \boldsymbol{u} = \mathbf{0}, \qquad \lim_{R \to \infty} T = 0, \tag{1.3}$$

where $R = \sqrt{x^2 + y^2 + z^2}$ is the spherical radial coordinate. To prescribe the source of buoyancy, a point-source condition of constant thermal flux is imposed at $z = 0$ by

$$\lim_{\varepsilon \to 0} \int_{S_\varepsilon} r \left(-\kappa \frac{\partial T}{\partial n} \right) \, \mathrm{d}S = F_0, \tag{1.4}$$

where $r = \sqrt{x^2 + y^2}$ is the cylindrical radial coordinate, S_ε is the hemisphere of radius $R = \varepsilon$ in the region $z \geq 0$, and F_0 is the prescribed constant source buoyancy flux.

Plumes have been well studied at the end member cases of asymptotically high and low Reynolds number regimes. In many previous studies, plumes have often been separated into two regimes. Namely, that of turbulent and laminar plumes. Chapters 2 and 3 discuss how these two regimes are asymptotic limits of a single, universal plume dependent only on the Prandtl number. The essentials of plume theory, describing both the laminar and turbulent similarity solutions, were developed by Zeldovich (1937) (an English translation is available in Zeldovich (1992)). In the following sub-sections the two topics are considered separately, since previous studies tended to focus on just one of the regimes.

1.1.1 Laminar plumes

For laminar plumes, similarity, boundary layer, and higher order numerical methods have been employed to study the flow regimes. The first work on laminar plumes proposed a similarity solution (derived in detail later), with

constant velocity w and height-multiplied temperature T, for an axisymmetric laminar plume (Zeldovich, 1937), given by

$$w = (F_0/\kappa)^{1/2} f\left(\left(F_0/\kappa^3\right)^{1/4} r z^{-1/2}\right), \tag{1.5a}$$

$$T = (F_0/g\beta\kappa) z^{-1} h\left(\left(F_0/\kappa^3\right)^{1/4} r z^{-1/2}\right), \tag{1.5b}$$

for radial coordinate r and vertical coordinate z, where f and h are structure functions that describe the shape of the velocity and temperature profiles, respectively (reviewed in detail below). The scaling between radius and height is derived from the assumption of a slender flow and predicts that the laminar plume rises in the shape of a parabola, illustrated in figure 1.3. Building from this, Yih (1951) provided a more detailed treatment of a laminar plume, determining a system of similarity equations dependent on Prandtl number, and solving them analytically for $Pr = 1$ and $Pr = 2$, to establish the spatial structure of the velocity and temperature fields (see Yih (1977) for a review, or Brand & Lahey (1967) for similar results).

In the laminar plume region, the studies above (Zeldovich, 1937; Yih, 1951; Brand & Lahey, 1967) make certain assumptions about the flow in order to simplify modelling. As a three-dimensional plume is axisymmetric when averaged over a sufficiently large time window, it is reasonable to assume the axisymmetric form of the system (1.1)–(1.4). As the laminar region is of a fixed height, and becomes steady after enough time, it can be reduced to a steady, axisymmetric problem by removing all terms with a time derivative $\partial/\partial t$, converting to cylindrical coordinates, and removing all terms with an azimuthal derivative from the equations. As a result, system (1.1) becomes

$$u\frac{\partial u}{\partial r} + w\frac{\partial u}{\partial z} = -\frac{1}{\rho_0}\frac{\partial p}{\partial r} + \nu\left(\frac{1}{r}\frac{\partial}{\partial r}\left(r\frac{\partial u}{\partial r}\right) + \frac{\partial^2 u}{\partial z^2}\right), \tag{1.6a}$$

$$u\frac{\partial w}{\partial r} + w\frac{\partial w}{\partial z} = -\frac{1}{\rho_0}\frac{\partial p}{\partial z} + \nu\left(\frac{1}{r}\frac{\partial}{\partial r}\left(r\frac{\partial w}{\partial r}\right) + \frac{\partial^2 w}{\partial z^2}\right) + g\beta T, \tag{1.6b}$$

$$\frac{1}{r}\frac{\partial (ru)}{\partial r} + \frac{\partial w}{\partial z} = 0, \tag{1.6c}$$

$$u\frac{\partial T}{\partial r} + w\frac{\partial T}{\partial z} = \kappa\left(\frac{1}{r}\frac{\partial}{\partial r}\left(r\frac{\partial T}{\partial r}\right) + \frac{\partial^2 T}{\partial z^2}\right), \tag{1.6d}$$

and the boundary conditions (1.2) and (1.3) become

$$\boldsymbol{u}(r, 0, t) = \mathbf{0}, \qquad \frac{\partial T}{\partial z}(r, 0, t) = 0, \tag{1.7}$$

and

$$\lim_{r\to\infty} \boldsymbol{u} = \boldsymbol{0}, \qquad \lim_{r\to\infty} T = 0, \tag{1.8}$$

respectively. Rather than using the point source condition specified in (1.4), a condition on the advective buoyancy flux is imposed (derived and justified later in section 2.1.1 and section 2.3.3, respectively),

$$2\pi \int_0^\infty g\beta r T(r, z_s, t) w(r, z_s, t)\ \mathrm{d}r = F_0, \tag{1.9}$$

where F_0 is a prescribed, constant buoyancy flux at $z = z_s$, and it is assumed that the flow starts at some displaced origin $z_s > 0$, directly in the laminar plume regime. This assumption is made in a large number of studies of laminar plumes (Zeldovich, 1937; Yih, 1951; Brand & Lahey, 1967; Worster, 1986). Finally, symmetry conditions along the plume centre at $r = 0$ are introduced

$$\frac{\partial \boldsymbol{u}}{\partial r}(0, z, t) = \boldsymbol{0}, \qquad \frac{\partial T}{\partial r}(0, z, t) = 0, \qquad \boldsymbol{u}(0, z, t) = \boldsymbol{0}. \tag{1.10}$$

Boundary layer theory

Boundary layer theory is used to further simplify the axisymmetric equations (1.6)–(1.10). The main assumption of a boundary layer (Schlichting & Gersten, 2003) is that the velocity gradients in the horizontal are large compared to those in the vertical ($\partial/\partial r \gg \partial/\partial z$). In the axisymmetric case (1.6)–(1.10), velocity gradients normal to the vertical axis of symmetry (i.e. in the radial direction) are assumed to be very large compared to those along the axis of symmetry.

In order to simplify the governing equations (1.6), boundary layer theory is used to estimate the relative sizes of certain terms (Yih, 1951; Brand & Lahey, 1967). Within the boundary layer, the radial length r scales with the width of the boundary layer $r \sim \delta$. The boundary layer is assumed to be slender and hence the ratio of radial to vertical length scales $\epsilon = \delta/L \ll 1$, where vertical length scales like $z \sim L$. Vertical velocity is also defined to scale like $w \sim W$. Hence, from mass conservation (1.6c), the radial velocity is of the order

$$u = O(\epsilon W). \tag{1.11}$$

Now the order of terms in the radial momentum equation (1.6a) can be written beneath each term to find that

$$\underbrace{u\frac{\partial u}{\partial r}+w\frac{\partial u}{\partial z}}_{=\mathcal{O}\left(\frac{\epsilon\mathcal{W}^2}{L}\right)}=-\frac{1}{\rho_0}\frac{\partial p}{\partial r}+\nu\left(\underbrace{\frac{1}{r}\frac{\partial}{\partial r}\left(r\frac{\partial u}{\partial r}\right)}_{=\mathcal{O}\left(\frac{\mathcal{W}}{\delta L}\right)}+\underbrace{\frac{\partial^2 u}{\partial z^2}}_{=\mathcal{O}\left(\frac{\epsilon^2\mathcal{W}^2}{L^2}\right)}\right). \tag{1.12}$$

By comparing the orders of each term in (1.12) the appearance of $\epsilon \ll 1$ in the advection and z-diffusion term render them much smaller than the r-diffusion term. Therefore, assuming that the remaining terms scale similarly results in the order of the partial derivative of the pressure with respect to r

$$\frac{\partial p}{\partial r}=\mathcal{O}\left(\rho_0\nu\frac{\mathcal{W}}{\delta L}\right), \tag{1.13}$$

and as a result, the order of the partial derivative of the pressure with respect to z is given by

$$\frac{\partial p}{\partial z}=\mathcal{O}\left(\rho_0\nu\frac{\mathcal{W}}{L^2}\right). \tag{1.14}$$

Now comparing the order of terms in the vertical momentum equation (1.6b) results in

$$\underbrace{u\frac{\partial w}{\partial r}+w\frac{\partial w}{\partial z}}_{=\mathcal{O}\left(\frac{\mathcal{W}^2}{L}\right)}=\underbrace{-\frac{1}{\rho_0}\frac{\partial p}{\partial z}}_{=\mathcal{O}\left(\nu\frac{\mathcal{W}}{L^2}\right)}+\nu\left(\underbrace{\frac{1}{r}\frac{\partial}{\partial r}\left(r\frac{\partial w}{\partial r}\right)}_{=\mathcal{O}\left(\frac{\mathcal{W}}{\delta^2}\right)}+\underbrace{\frac{\partial^2 w}{\partial z^2}}_{=\mathcal{O}\left(\frac{W^2}{L^2}\right)}\right)+g\beta T, \tag{1.15}$$

illustrating both that

$$-\frac{1}{\rho_0}\frac{\partial p}{\partial z}\ll\nu\frac{1}{r}\frac{\partial}{\partial r}\left(r\frac{\partial w}{\partial r}\right), \quad \text{and} \quad \frac{\partial^2 w}{\partial z^2}\ll\nu\frac{1}{r}\frac{\partial}{\partial r}\left(r\frac{\partial w}{\partial r}\right), \tag{1.16}$$

because $\delta \ll L$. As a result, both the pressure term and the z-diffusion term can be neglected from the vertical momentum equation (1.15). Similarly, the z-diffusion term can be neglected from the temperature conservation equation

(1.6d), resulting in the boundary layer equations at leading order

$$u\frac{\partial w}{\partial r} + w\frac{\partial w}{\partial z} = \nu\left(\frac{1}{r}\frac{\partial}{\partial r}\left(r\frac{\partial w}{\partial r}\right)\right) + g\beta T, \tag{1.17a}$$

$$\frac{1}{r}\frac{\partial (ru)}{\partial r} + \frac{\partial w}{\partial z} = 0, \tag{1.17b}$$

$$u\frac{\partial T}{\partial r} + w\frac{\partial T}{\partial z} = \kappa\left(\frac{1}{r}\frac{\partial}{\partial r}\left(r\frac{\partial T}{\partial r}\right)\right). \tag{1.17c}$$

At the centre of plume, the symmetry conditions (1.10) are

$$\frac{\partial w}{\partial r} = 0, \qquad \frac{\partial T}{\partial r} = 0, \qquad u = 0, \qquad \text{at } r = 0. \tag{1.18}$$

The far-field conditions (1.8) are

$$w \to 0, \qquad T \to 0, \qquad \text{as } r, z \to \infty, \tag{1.19}$$

and the buoyancy flux condition (1.9) remains

$$2\pi \int_0^\infty g\beta r T w \, \mathrm{d}r = F_0. \tag{1.20}$$

The system (1.17)–(1.20) forms a fifth order (2nd order from (1.17a) + 1st order from (1.17b) + 2nd order from (1.17c)) coupled diffusion problem with five boundary conditions. If desirable, the numerical solution of this system can be found using a time-marching procedure for z until the solution reaches a 'steady state'. This process will be used later in chapter 4 to predict the maximum rise height of a laminar plume in a stratification. Instead, however, in an unstratified environment, the boundary layer equations can be further simplified by making use of similarity scalings (Zeldovich, 1937).

Similarity theory

A similarity solution of a set of partial differential equations is a solution that depends on certain groupings of the independent variables, rather than on each variable separately. Similarity solutions occur when the system has no characteristic length or time scale. The unstratified plume will be shown to admit a similarity solution in the following.

Investigating the scalings between the advection and source terms (1.17a), the advection and diffusion terms in (1.17c), and the buoyancy flux condition (1.20) results in the scaling relationships

$$w\frac{\partial w}{\partial z} \sim g\beta T, \quad w\frac{\partial T}{\partial z} \sim \kappa\left(\frac{1}{r}\frac{\partial}{\partial r}\left(r\frac{\partial T}{\partial r}\right)\right), \quad 2\pi\int_0^\infty g\beta r T w \,\mathrm{d}r \sim F_0, \tag{1.21}$$

leading to $w^2 \sim g\beta T z$, $r^2 w \sim \kappa z$, and $g\beta r^2 T w \sim F_0$, respectively. Resolving these, one finds that the only intrinsic horizontal length scale in the system $r \sim (\kappa^3/F_0)^{1/4} z^{1/2}$ and is dependent only on z, revealing that the system exhibits a similarity solution. The scaling further reveals that the independent variable in the similarity solution can be defined as

$$\eta = \left(F_0/\kappa^3\right)^{1/4} r z^{-1/2}. \tag{1.22}$$

Using a similarity solution allows the problem to be reduced from two independent variables r and z, and three dependent variables u, w, and T, to a problem with one independent variable η and two dependent variables f and h (these will be defined shortly). This greatly reduces the complexity of the problem.

In order to derive the similarity system, the Stokes stream function ψ is first defined such that

$$w = \frac{1}{r}\frac{\partial \psi}{\partial r}, \qquad u = -\frac{1}{r}\frac{\partial \psi}{\partial z}. \tag{1.23}$$

Substituting the Stokes stream function into the boundary layer equations (1.17a) and (1.17c) results in

$$\begin{aligned}\frac{1}{r^3}\frac{\partial\psi}{\partial z}\cdot\frac{\partial\psi}{\partial r} - \frac{1}{r^2}\frac{\partial\psi}{\partial z}\cdot\frac{\partial^2\psi}{\partial r^2} + \frac{1}{r^2}\frac{\partial\psi}{\partial r}\cdot\frac{\partial^2\psi}{\partial z\,\partial r} \\ = \nu\left(\frac{1}{r^3}\frac{\partial\psi}{\partial r} - \frac{1}{r^2}\frac{\partial^2\psi}{\partial r^2} + \frac{1}{r}\frac{\partial^3\psi}{\partial r^3}\right) + g\beta T,\end{aligned} \tag{1.24a}$$

$$-\frac{1}{r}\frac{\partial\psi}{\partial z}\cdot\frac{\partial T}{\partial r} + \frac{1}{r}\frac{\partial\psi}{\partial r}\cdot\frac{\partial T}{\partial z} = \kappa\left(\frac{1}{r}\frac{\partial T}{\partial r} + \frac{\partial^2 T}{\partial r^2}\right), \tag{1.24b}$$

respectively. By investigating the scalings between terms in (1.24) and the buoyancy flux condition (1.20), the following scaling relationships between ψ,

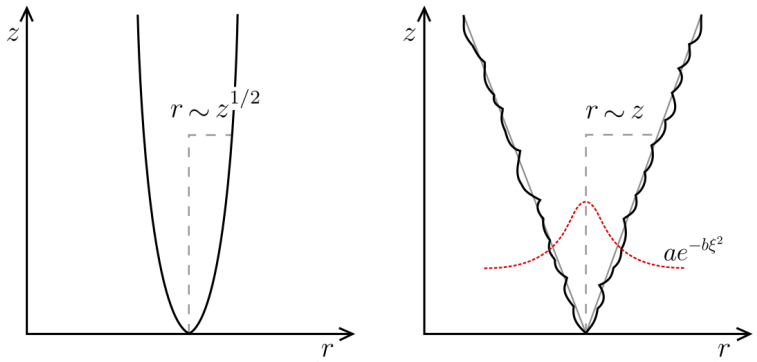

Figure 1.3: Schematic to compare the shapes of the laminar (left) and turbulent (right) similarity solutions of a plume. A laminar plume is shaped like a parabola according to the scaling in (1.5) and a turbulent plume is shaped like a cone according to the scaling in (1.35). A Gaussian curve of the form $a\exp(-b\xi^2)$ for $\xi = rz^{-1}$ is plotted over the turbulent plume to illustrate using Gaussians as the structure functions ϕ and ϑ in (1.35).

T, and z can be derived

$$\psi \sim \kappa z, \qquad T \sim \left(\frac{F_0}{g\beta\kappa}\right) z^{-1}. \tag{1.25}$$

As for the independent variable η in (1.22), the scalings (1.25) allow for the definition of the two dependent similarity variables $f(\eta)$ and $h(\eta)$ such that

$$\psi = \kappa z f(\eta), \qquad T = \left(\frac{F_0}{g\beta\kappa}\right) z^{-1} h(\eta), \tag{1.26}$$

where $f(\eta)$ and $h(\eta)$ are known as structure functions (Zeldovich, 1937) representing the height-independent radial profiles of velocity and temperature, respectively. By substituting the equation for ψ (1.26) into the definition of the stream function (1.23), the vertical velocity w is given by

$$w = \left(\frac{F_0}{\kappa}\right)^{1/2} \frac{f'(\eta)}{\eta}. \tag{1.27}$$

In accordance with (1.22), (1.26) and (1.27), the vertical velocity w is constant with height, the temperature $T \sim z^{-1}$ decays linearly with height, and the radius of the plume expands as $r \sim z^{1/2}$, resulting in the laminar plume exhibiting a parabolic shape, illustrated in figure 1.3. Substituting the relations (1.26) into (1.24) and rearranging using (1.22) to replace $rz^{-1/2}$ groupings results in the ODEs (Brand & Lahey, 1967)

$$\frac{1}{\eta}ff' - ff'' = Pr\left(\frac{1}{\eta}f' - f'' + \eta f'''\right) + \eta^2 h, \tag{1.28a}$$

$$-\frac{1}{\eta}fh' - \frac{1}{\eta}f'h = \frac{1}{\eta}h' + h'', \tag{1.28b}$$

where the Prandtl number $Pr = \nu/\kappa$ is the ratio of viscosity to thermal diffusivity. Note that (1.28b) can be simplified by multiplying through by η and using an application of the product rule of differentiation on both the left and right hand side of (1.28b) to result in

$$-\left(fh\right)' = \left(\eta h'\right)'. \tag{1.29}$$

Subsequently integrating (1.29) subject to the boundary conditions at $\eta = 0$, and rearranging (1.28a), results in the system (Yih, 1951)

$$-f\left(\frac{f'}{\eta}\right)' = Pr\left(\eta\left(\frac{f'}{\eta}\right)'\right)' + \eta h, \tag{1.30a}$$

$$h' = -\frac{1}{\eta}fh. \tag{1.30b}$$

The velocity boundary conditions defined in (1.18) are reframed in similarity form using (1.23), (1.26) and (1.27) to result in

$$\lim_{\eta\to 0}\left(-\frac{1}{\eta}f'(\eta) + f''(\eta)\right) = 0, \qquad \lim_{\eta\to 0}\left(f(\eta) - \frac{1}{2}\eta f'(\eta)\right) = 0. \tag{1.31}$$

As are the far-field conditions (1.19), to result in

$$f' = 0, \qquad h = 0, \qquad \text{as } \eta \to \infty. \tag{1.32}$$

Finally the buoyancy flux condition (1.20), is written in similarity form

$$2\pi \int_0^\infty hf' \, \mathrm{d}\eta = 1. \tag{1.33}$$

Since the introduction of the similarity solution (Zeldovich, 1937; Yih, 1951; Brand & Lahey, 1967) there have been a number of studies of both two-dimensional and axisymmetric laminar plumes. For example Morton (1967) proposed an entrainment model for laminar plumes for both high and low Prandtl numbers, Roberts (1977) studied convection from a heated strip in two dimensions, finding a scaling for the dimensionless heat flux in terms of

the Rayleigh number, and Loper & Stacey (1983) analytically investigated and described the structure of mantle plumes with temperature dependent viscosity.

Worster (1986) considered the asymptotic reduction of the similarity system (1.30)–(1.33) for large Prandtl number (large viscosity), matching an inner viscous region to an outer buoyancy-driven flow to develop asymptotic predictions for the velocity and temperature profiles. Worster (1986) determined the asymptotes for dimensionless centreline values of velocity w_0 and temperature h_0 to be

$$w_0 \equiv \lim_{\eta\to 0}\left(\frac{f'(\eta)}{\eta}\right) \sim 0.40\,\varepsilon^2\log(\varepsilon^{-2}), \tag{1.34a}$$

$$h_0 \equiv h(0) \sim 0.079, \tag{1.34b}$$

as $Pr \to \infty$, where ε is a small parameter defined implicitly by $\varepsilon^4\log(\varepsilon^{-2}) = Pr^{-1}$.

More recently, Kaminski & Jaupart (2003) used numerical simulations and laboratory experiments to study the temporal evolution of laminar plumes at high Prandtl number, showing that near the source plumes accelerate due to development of the viscous boundary layer, and outside of this layer, plumes ascend as predicted by steady plume theory. Whittaker & Lister (2006) addressed an axisymmetric laminar plume rising from a point source in a very viscous fluid. They found a vertical length scale on which advection becomes comparable with diffusion and derived an asymptotic solution for flow above this height.

1.1.2 Turbulent plumes

At the turbulent end of the spectrum, Zeldovich (1937) proposed, on the basis of scaling, that the vertical velocity w and temperature T fields of a turbulent plume fed by a constant source of buoyancy, decrease with height z in proportion to $z^{-1/3}$ and $z^{-5/3}$, respectively, given by

$$w = F_0^{1/3}z^{-1/3}\phi(rz^{-1}), \qquad T = (F_0^{2/3}/g\beta)z^{-5/3}\vartheta(rz^{-1}), \tag{1.35}$$

where, as in the laminar regime, ϕ and ϑ are structure functions that describe the shape of the velocity and temperature profiles. These scalings result from an assumption that both horizontal and vertical scales remain comparable, differing from the asymptotic assumption of a slender flow underlying the theories of laminar plumes, and predicting that a turbulent plume rises in a cone of fixed angle, illustrated in figure 1.3. While in a laminar plume the velocity remains constant throughout the height of the plume, in the turbulent case the vertical velocity decreases with height like $z^{-1/3}$. In both cases the temperature drops with height, however it does so faster in the turbulent regime. In the laminar plume the temperature falls with z^{-1} whereas in the turbulent regime it decreases like $z^{-5/3}$. These scalings for vertical velocity and temperature, first described by Zeldovich (1937), have been used widely in plume modelling since their initial description (Hunt & Van den Bremer, 2011). Separately, Schmidt (1941) presented a more detailed eddy-viscosity model of turbulent plumes, which preserves the scalings introduced by Zeldovich (1937) and further makes predictions for the approximate structure functions describing the transverse velocity and temperature profiles.

The forms of the structure functions ϕ and ϑ (1.35) were constrained directly using experiments by Rouse et al. (1952), who suggest they conform closely to Gaussians of the form $\phi(\xi) = a_w \exp(-b_w \xi^2)$ for vertical velocity w and $\vartheta(\xi) = a_T \exp(-b_T \xi^2)$ for temperature T, where the similarity variable $\xi = rz^{-1}$ and a and b are profile coefficients with subscripts w and T, for vertical velocity and temperature, respectively. A Gaussian is plotted over the schematic of the turbulent plume in figure 1.3 to illustrate using Gaussians as structure functions. Rouse et al. (1952) found values for $b_w = 96$ and $b_T = 71$ for vertical velocity and temperature respectively, in essence suggesting that the vertical velocity profile is thinner than the temperature profile. Papanicolaou & List (1988) agree, stating that authors who disagree, such as George Jr et al. (1977) and Nakagome & Hirata (1977), took measurements too close to the source. Later, Shabbir & George (1994) also found that the vertical velocity profile was wider than the the temperature profile, with exponential coefficients of $b_w = 58$ and $b_T = 68$, respectively. Since the widespread accessibility of computational resources, studies have been able to report Gaussian profiles more accurately by using numerical simulations to study plume flow. Plourde et al. (2008); Van Reeuwijk et al. (2016) both report approximate Gaussian profiles for vertical velocity and temperature, and Devenish et al. (2010) report the same value for both velocity and temperat-

ure of $b_w = b_T = 60 \pm 10$. Despite some of the variability in the coefficients a_w, a_T, b_w, and b_T, defining the structure functions and finding accurate values for the coefficients enables researchers to develop simple predictive models of plume rise, such as the well-known Morton et al. (1956) model.

Arguably the most widespread turbulent plume model is that described by Morton et al. (1956), so much so that it is often given its own nickname, the MTT model, for its authors: B. R. Morton, G. I. Taylor, and J. S. Turner. Their model describes an axisymmetric, turbulent plume rising from a point source. They proposed a width-averaged theory of turbulent plumes based on parametrising turbulent entrainment, applicable to stratified and unstratified environments. They claim that the inflow at the edge of a convective plume is related to some characteristic velocity of the plume itself. The main assumptions are: that the plume is fully turbulent; that the rate of entrainment is proportional to the vertical velocity at that height, this is implemented by introducing an entrainment coefficient (known as the entrainment hypothesis); that the profiles of mean vertical velocity and temperature in horizontal sections are of similar forms at all heights; and that the Boussinesq approximation applies, namely that the largest local density variations in the field of motion are small in comparison with the density of the ambient at the source level. They also make predictions for the height of the neutral buoyancy level (NBL). By modelling horizontally averaged volume Q, momentum M, and buoyancy F fluxes, defined by

$$Q = 2\pi \int_0^\infty wr \, \mathrm{d}r, \quad M = 2\pi \int_0^\infty w^2 r \, \mathrm{d}r, \quad F = 2\pi \int_0^\infty g' w r \, \mathrm{d}r, \tag{1.36}$$

for vertical velocity w, radial coordinate r, and reduced gravity g', Morton et al. (1956) developed the following dimensional differential equations describing the steady-state behaviour of a plume

$$\frac{\mathrm{d}Q}{\mathrm{d}z} = 2\alpha M^{1/2}, \tag{1.37a}$$

$$\frac{\mathrm{d}M}{\mathrm{d}z} = \frac{FQ}{M}, \tag{1.37b}$$

$$\frac{\mathrm{d}F}{\mathrm{d}z} = -N^2 Q, \tag{1.37c}$$

where z is height, N is the Brunt-Väisälä frequency, and α is a constant coefficient parametrising entrainment of fluid into the plume. The initial conditions

are given by

$$Q = Q_0\,\mathrm{m}^3\,\mathrm{s}^{-1}, \quad M = M_0\,\mathrm{m}^4\,\mathrm{s}^{-2}, \quad F = F_0\,\mathrm{m}^4\,\mathrm{s}^{-3}. \tag{1.38}$$

The Brunt-Väisälä frequency, N, represents the stratification of the ambient. In the case where the density of the ambient fluid is constant with height ($N = 0$) the right hand side of (1.37c) vanishes and the system can be solved analytically by substituting solutions of the form $Q = pz^a$ and $M = qz^b$, where p and q are constants, to find

$$Q = \frac{6\alpha}{5}\left(\frac{9}{10}\alpha F_0 z^5\right)^{1/3}\,\mathrm{m}^3\,\mathrm{s}^{-1}, \tag{1.39a}$$

$$M = \left(\frac{9}{10}\alpha F_0 z^2\right)^{2/3}\,\mathrm{m}^4\,\mathrm{s}^{-2}, \tag{1.39b}$$

$$F = F_0\,\mathrm{m}^4\,\mathrm{s}^{-3}. \tag{1.39c}$$

In the stratified case ($N > 0$) the equations can be solved numerically, using a fourth-order Runge-Kutta method, terminating where the momentum of the plume is zero. The location of zero buoyancy is the NBL and the location of zero momentum is the maximum rise height of the plume. Both the unstratified and stratified solutions are included in figure 1.4. The description of the plume fluxes and the rise height (in the stratified case) can be compared to laboratory, numerical, and real-world plumes for verification of other numerical models or for making predictions of plumes in the physical world.

An alternative model of plume rise, developed at a similar time as that of Morton et al. (1956), is that of Priestley & Ball (1955). Instead of a model based on volume, momentum, and buoyancy flux, they described plume evolution using volume, momentum, and kinetic energy flux of the plume. They also introduced an entrainment relation for turbulent plume flow. Fox (1970) compared both models in an attempt to reconcile the two theories, showing that the entrainment parameter α is dependent on the Reynolds stress and the shape of the velocity and buoyancy profiles.

The models described by both Priestley & Ball (1955) and Morton et al. (1956) consider a turbulent plume that originates at an idealised point source, forming a so-called 'pure' plume. This is an assumption used to simplify the problem. It is not possible for a real-world plume to have zero radius, there must be some finite area at which buoyancy is introduced. Making a

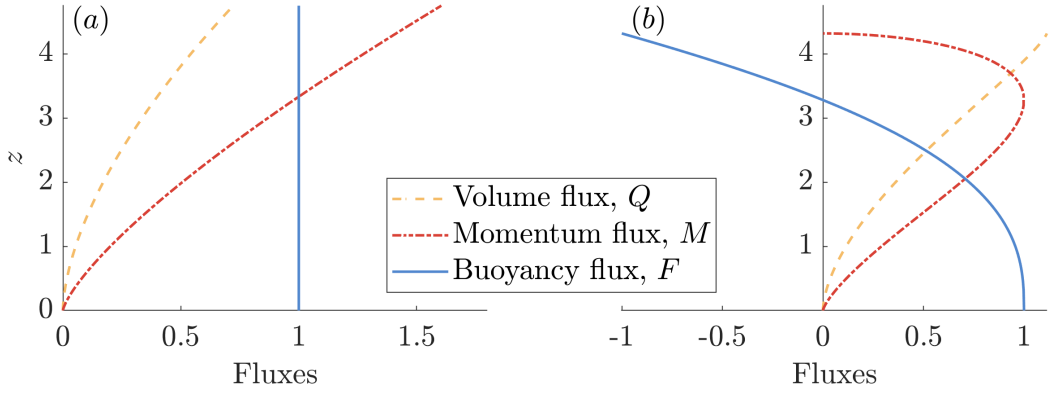

Figure 1.4: Solutions of the model described by Morton et al. (1956). In panel (a) is the analytical solution to the unstratified case, described in (1.39), for $Q_0 = 0\,\mathrm{m^3\,s^{-1}}$, $M_0 = 0\,\mathrm{m^4\,s^{-2}}$, $F_0 = 1\,\mathrm{m^4\,s^{-3}}$ and $\alpha = 0.1$. In panel (b) is the numerical solution to the stratified case, described in (1.37)–(1.38) and (1.38), for $Q_0 = 0\,\mathrm{m^3\,s^{-1}}$, $M_0 = 0\,\mathrm{m^4\,s^{-2}}$, $F_0 = 1\,\mathrm{m^4\,s^{-3}}$, $N = 1\,\mathrm{s^{-1}}$, and $\alpha = 0.1$, and solved using a fourth-order Runge-Kutta method.

point source assumption, however, simplifies the physics to facilitate a unique solution of a plume without considering the effect of source conditions, which can have a large impact on the flow. As a result, the point source assumption is made for all the plumes considered in this thesis. Morton (1959) showed that the behaviour of a plume from a finite-sized source can be related to a virtual point source of buoyancy and momentum, introducing a method that enables plumes generated from a finite-sized source to be compared to plumes from a point source.

Morton & Middleton (1973) described a lazy plume, one with a deficit of momentum flux at the source compared to a 'pure' plume with the same volume flux and buoyancy flux. They also proposed the existence of a virtual origin above the theoretical origin, and described and observed an initial narrowing of the plume, caused by the excess buoyancy accelerating the flow. They base this location on the definition of a source parameter that relates the initial fluxes. Hunt & Kaye (2005) extended the work of Morton & Middleton (1973) to include sources with non-zero radius, describe the region in which the plume transitions from the source conditions to a turbulent 'pure' plume, and compare their results to the work of Morton et al. (1956). These studies brought into plume terminology the terms pure, lazy, and forced to describe plumes. The terms refer to the initial state of the plume source. A lazy plume is said to have an initial buoyancy flux that dominates over the initial mo-

mentum flux, resulting in an acceleration and narrowing of the plume as the two equilibrate. A forced plume is the opposite, with the initial momentum flux dominating the buoyancy flux, resulting in a deceleration and widening of the plume. The works of Morton & Middleton (1973) and Hunt & Kaye (2005) both suggested that the Morton et al. (1956) model takes over once the initial behaviour has been 'resolved' by the governing equations. The pure plume, then, is the one that both the forced and lazy plumes transition towards, after the initial source condition has been resolved. As the plumes considered in this thesis emanate from a point source, they are all, by definition, pure plumes.

There have been numerous works on the entrainment hypothesis proposed by Morton et al. (1956), starting with Fox (1970) who developed a plume model for forced plumes with entrainment strongly related to the mean axial velocity of the flow. Hunt & Kaye (2005) suggested that while the constant-entrainment model is not always accurate, some reduced-entrainment flows can be modelled using constant α, given source conditions and buoyancy flux gain (buoyancy flux can increase as the plume rises in certain atmospheric flows) is taken into account. It is also suggested by Carazzo et al. (2008) that the constant-entrainment model does not make accurate predictions of the rise height of submarine hydrothermal vents and terrestrial volcanic eruptions because the effect of the turbulent mixing on the plume rise is not properly captured. They proposed a new model using variable entrainment, dependent on the buoyancy of the plume, that was shown to predict flux values of plumes on Earth, and rise heights of Martian and Venusian plumes, more accurately than the Morton et al. (1956) model. Van Reeuwijk & Craske (2015) integrated the volume, momentum, buoyancy, and kinetic energy equations, using both the Morton et al. (1956) and Priestley & Ball (1955) models, to over-constrain the equations and hence find a restriction on the entrainment coefficient. They decomposed the entrainment coefficient into contributions due to the production of turbulence kinetic energy, buoyancy, and profile coefficients and found that larger entrainment in a plume over a jet is due to the buoyancy effects associated with the mean flow, rather than the effects of buoyancy on turbulence. They conclude that a variable-entrainment model may be more appropriate than a constant model for predictions of real world plumes. The entrainment parameter is used widely in much of plume research, however the entrainment of fluid is modelled directly in the simulations performed in this thesis. As the entrainment parameter is empirically defined, simulations can be used to confirm its value.

1.1.3 Instability in plume dynamics

Bridging the gap between the laminar and turbulent flow is a transition zone that links the two regimes. As the laminar plume rises, scaling analysis of (1.5) shows that the local laminar Reynolds number scales like $Re_L \sim z^{1/2}$ with height z and hence increases as the plume rises until an instability causes a transition to turbulence. To date, a complete description of the spatial structure arising from the transition to fully developed turbulence of a classical plume remains an open problem, however a number of studies have investigated instabilities in plumes.

Dombrowski et al. (2005) conducted laboratory experiments and performed a similarity scaling of a saline jet (or a forced plume) in a stratification. They empirically derived a scaling law for the location of a specific type of instability, known as a coiling instability, finding a linear relationship between the velocity of the jet and the square of the height to instability. They also found that the rise height (penetration depth using the orientation of their experiments) is non-monotonic with inlet velocity due to the instability that occurs earlier in faster flows.

In a similar vein, Lombardi et al. (2011) used laboratory experiments and DNS to focus on the sinuous versus varicose instability specific to a two-dimensional plume, with high Prandtl number, originating from a finite areal source. They focused on analysing the effect of a stratification in suppressing the short-term initial instability of a plume, developing a scaling law for the rise height of a plume based on the source area, the volume flux, the stratification, and the viscosity. They also showed that, in a stratification, the maximum height attained by a plume is dependent on the final steady state, rather than on the instability.

Instead of a investigating the instability of a plume in a stratification, López Moscat & Marqués Truyol (2013) focused on the various types of instability exhibited by a plume in an unstratified, enclosed cylinder emanating from an areal source for increasing Rayleigh number. They investigated the emergence of symmetries in the initial instability of plumes, providing a classification of different symmetries from the perspective of a dynamical system. They reported behaviour ranging from a laminar plume, to 'puffing' phenomena and symmetry-breaking tilted rings emitted directly from the heated

source, to the source emitting several plume-like eruptions. A linear global stability analysis performed by Lesshafft (2015) suggested that at least one of the behaviours demonstrated by López Moscat & Marqués Truyol (2013) was due to the presence of the top and bottom walls enclosing the plume, illustrating that a solid enclosure can have a profound impact on the plume flow and transition to instability.

Extending the linear instability analysis of Lesshafft (2015) to unenclosed plumes, Chakravarthy et al. (2018) found that the dominant force producing an instability in laminar lazy plumes is buoyancy, rather than shear, with the converse true for jets. However, they also cautioned that the characteristics of the instability are sensitive to the profile of the flow at the inlet and hence may not be extendable to generic plume flows, such as a pure plume generated at a point source of heat.

Another form of instability often studied in plume dynamics is that generated by time-varying source conditions, referred to as an unsteady plume. Scase & Hewitt (2012) investigated a number of previous unsteady turbulent plume models and claimed that they were ill-posed, but could be regularised in some cases by the addition of a velocity diffusion term. Scase & Hewitt (2012) found that this new term had little effect for applications in which the plume source is steady, however. In the laminar regime Hewitt & Duck (2011) found that an unsteady source leads to downstream growth of a short-wave linear instability which triggers the breakdown of the laminar boundary layer structure. This breakdown in the unsteady regime is similar to that in plumes with steady source conditions, such as those considered in this thesis, but varies in that the instability and transition to turbulence is caused by wave propagation from the varying source conditions, a process that does not occur in plumes with steady sources.

1.1.4 Plumes in a stratification

One of the first works of turbulent plume rise, with a point source and in a stratification, was performed by Morton et al. (1956), using the model (1.37)–(1.38) for $N > 0$. The model can be solved by numerically integrating (1.37) subject to the source conditions (1.38) and terminating when the momentum flux becomes zero. The solution for volume Q, momentum M, and buoyancy

F flux, for $F_0 = 1\,\mathrm{m}^4\,\mathrm{s}^{-3}$ and $N = 1\,\mathrm{s}^{-1}$, is plotted in figure 1.4. The buoyancy flux decreases with height, and the neutral buoyancy level (NBL) of the plume is located at a height of $3.28\,(F_0N^{-3})^{1/4}\,\mathrm{m}$ where the buoyancy flux is zero. The momentum flux first increases from zero and begins to decrease after the plume passes its NBL. The rise height is located at a height of $4.32\,(F_0N^{-3})^{1/4}\,\mathrm{m}$ where the momentum flux becomes zero. The model described by Morton et al. (1956) is often used in the study of plumes, from comparisons with higher order models (Devenish et al., 2010) to modelling particle dispersal from the NBL (Sparks et al., 1991).

There have been a number of studies of turbulent plumes in a stratification. For example, Kotsovinos (2000) performed experiments on a plume rising in an unstratified layer and subsequently penetrating into a stratified layer to investigate the growth of the neutrally buoyant intrusion layer at the NBL. Devenish et al. (2010) used large-eddy simulations to investigate the behaviour of plumes in both unstratified and stratified environments. They showed good agreement with the simpler model of Morton et al. (1956) for the unstratified case, but in the stratified case suggested that the effects of the finite source are still impacting the flow even up to the height where stratification becomes important. Rooney & Devenish (2014) performed a scaling analysis and suggested that plume rise and spread in a linear stratification is controlled by the buoyancy frequency and the source buoyancy flux. Mirajkar & Balasubramanian (2017) varied stratification strengths showing that increasing the strength of the stratification leads to a decrease in maximum rise height. All the studies listed here are examples of studies that have investigated the behaviour of turbulent plumes in a stratification, however, none of them consider the behaviour of plumes in a stratification across a spectrum of laminar to turbulent flow.

There has been little work to date on the rise height of laminar plumes in a stratification. Performing experiments on turbulent jets, Dombrowski et al. (2005) found that the rise height varies non-monotonically with inlet velocity due to the instability that occurs earlier in faster flows. Lombardi et al. (2011) used laboratory experiments and DNS to analyse the initial instability of a plume and developed a scaling law for the rise height based on the source area, volume flux, stratification, and viscosity, showing that the rise height is largely unaffected by the initial instability and determined largely by the steady state flow. Xue et al. (2019) performed laboratory experiments of fountains, similar

to jets but with a negative buoyancy, by pouring a liquid into a container filled with a denser fluid. They characterised the flow based on the Reynolds number, focusing on lower Reynolds numbers, and find that rise height (or penetration depth to use their orientation) varies with Reynolds number, with a maximum rise height at $Re \approx 200$. The work of Xue et al. (2019) considered the rise height of fountains, however, a gap in the literature has been identified here for the rise height of plumes, rather than fountains or jets, across a spectrum of Reynolds numbers.

1.1.5 Starting plumes

So far, all of the preceding discussion has focused on steady state plumes. A starting plume is the time-dependent precursor to the steady plume, consisting of the production of an advancing 'head' or 'cap' at the transient front of the plume flow which can be laminar or turbulent, and leaves the steady plume flow behind it as it progresses. Experiments of starting plumes illustrate the development of a pronounced head above a thin, approximately steady stem (e.g. Moses et al., 1993). Turner (1962) and Bhamidipati & Woods (2017) both use laboratory experiments to determine that for a turbulent plume the head rises at 0.6 times the mean stem speed. Bhamidipati & Woods (2017) propose a theoretical model that suggests that 61% of the total buoyancy released from the source accumulates in the plume head. These two studies both assume that the plume beneath the head is turbulent, leading us to question how the head behaves in higher viscosity plumes.

Moses et al. (1993) consider a laminar starting plume and find that the laminar head rises at a constant velocity, from a finite areal source. They suggest that the increasing Reynolds number of the growing head causes the plume to become unstable. Using scaling arguments it can be shown that the width of the stem grows as time $t^{1/2}$ (Batchelor, 1954) and Moses et al. (1993) suggest that the width of the plume head grows at the same rate. They also find that the head ascent velocity is $\dot{h_p} = 0.23\,(F_0/\nu)^{1/2}\,\mathrm{m\,s^{-1}}$ for buoyancy flux F and viscosity ν, which is a result that can be compared to numerical simulations of plumes. In the large Prandtl number regime, Kaminski & Jaupart (2003) find that the rise speed of the head is dependent on the Prandtl number for $Pr > 7$, suggesting that the rise speed of the plume front is proportional to the centreline value of velocity (1.34) predicted by Worster (1986). For simulations

investigating plume rise over a range of Prandtl numbers, the work of Kaminski & Jaupart (2003) can used to predict the rise speed of the plume front.

More recently, Vatteville et al. (2009) and Davaille et al. (2011) have performed detailed laboratory and numerical analysis of starting laminar plumes in viscous fluids at various initial buoyancy fluxes, to show that the flow in the laboratory can be accurately obtained using numerical predictions. Both studies suggest that temperature-dependent viscosity has a significant impact on plume flow in high-Prandtl number plumes, noting discrepancies from the uniform-viscosity models of Worster (1986) and Kaminski & Jaupart (2003).

1.1.6 Particle transport

There are many examples of particle transport by plumes in nature in the literature, from a volcanic eruption to aerosols in a room. In particular the field of natural ventilation, in which particle transport in laminar plumes are significant, has been of interest in recent years due to the Covid-19 pandemic, with a focus on air quality in offices, classrooms, and hospital wards (Tang et al., 2006). A gap in the literature has been identified regarding particle transport in both laminar and hybrid laminar-turbulent plumes.

Many studies have focused on particle fallout from turbulent plumes, with some producing predictions for particle build up. Some of these are listed and discussed below, as the results can be used in the study of laminar and hybrid laminar-turbulent plumes. For example, Ernst et al. (1996) developed a theoretical model for sedimentation from the outer edge of a particle-laden turbulent plume in an unstratified, quiescent environment, and more recently, Pegler & Ferguson (2021) developed a model for the dispersal of particles from hydrothermal plumes. These studies illustrate the work done on particle transport in turbulent plumes and comparisons between them and particle transport in laminar and hybrid laminar-turbulent plumes can be made to verify new models.

1.2 Modelling plumes using high-order numerical methods

The invention and widespread availability of high performance computing (HPC) for scientific research has enabled researchers to solve complicated partial differential equations describing the behaviour of plumes numerically. The benefit of this method can be (relatively) quick, reproducible simulations with which many different numerical experiments can be performed in a short space of time, resulting in comprehensive parametric studies. This technique is not infallible, however, because it can require certain assumptions and simplifications. For example, lower Reynolds numbers than present in physical phenomena may be necessary. Furthermore, it has its own set of quantities that must be satisfied, such as mesh sensitivity, stability criteria, and convergence criteria. High-order numerical methods are the main approach used for modelling plumes in this thesis.

There are a number of different simulation methods to choose from when performing numerical simulations. A short, incomprehensive list includes techniques such as Reynolds-averaged Navier-Stokes (RANS) modelling, large-eddy simulation (LES), smoothed-particle hydrodynamics (SPH), and direct numerical simulations (DNS). For the majority of options, the governing equations require modification to reduce the complexity of the solution, often parametrising the small scale motions of the flow using a turbulence model.

One of the most intensive forms of numerical fluids research, DNS, solves the governing equations without any turbulence modelling and hence requires a mesh fine enough to resolve every detail of a flow. This is both the main advantage and disadvantage of DNS, in that the equations modelled are 'correct', yet the requirement on the mesh resolution results in a very numerically expensive simulation. A further advantage is that turbulence models do not have to be tested and verified, compared to techniques such as RANS and LES.

The detail in the flow fields that result from using DNS enable it to be used in studying fundamental behaviour within the plume. DNS has been employed in the field of plume dynamics to study the formation of vortices in the near-source region and their dependence on source temperature of axisymmetric plumes (Jiang & Luo, 2000), the accuracy of subgrid-scale

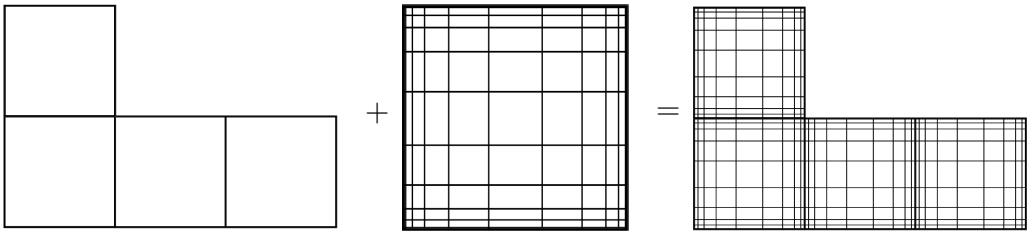

Figure 1.5: Illustration of the meshes of finite element methods (FEM) and spectral methods combining to produce the mesh used for spectral element methods (SEM).

models (Pham et al., 2007) for large eddy simulation (LES), the near source behaviour of heated, areal sources (Plourde et al., 2008), the effect of rotation on plume evolution and structure (Fabregat Tomàs et al., 2016), the detailed flow properties of jets, forced plumes, and pure plumes validating the Priestley & Ball (1955) entrainment model (Van Reeuwijk et al., 2016), and the effect of wind-advection (Jordan et al., 2022). These studies all use DNS to investigate a specific part of turbulent plumes.

After making the decision to use DNS for the numerical simulations in this thesis, a further choice of the type of discretisation scheme is required since, without making simplifying assumptions such as axisymmetry or boundary layer assumptions, an analytical solution is unavailable for the fully 3D governing equations (1.1)–(1.4). The governing equations need to be discretised in order to model the flow on a computational mesh. Some options for discretisation methods include finite difference, finite volume, finite element (FEM), spectral, and spectral element methods (SEM). A SEM is a combination of a FEM and a spectral method (Boyd, 2001), examples of a simple mesh used for each method are presented in figure 1.5. The SEM was first introduced by Patera (1984) and is the choice of discretisation for the numerical simulations in this thesis.

1.2.1 Finite element methods (FEM)

In order to describe the spectral element method (SEM), the concepts of finite element methods (FEM) and spectral methods are first introduced. Some of the earliest work on FEM can be found in Courant (1943), for a historical review see Oden (1991). It should be noted that the presentation of finite

elements in this section is constructive and avoids a number of subtleties that are discussed in textbooks such as Oden (1991).

While the equations in this thesis are three-dimensional with a number of dependent variables (e.g. velocity, temperature, pressure), the topic is introduced using a simple one dimensional problem with one dependent variable $u(x,t)$ that is continuous across the domain of interest. Let x and t be spatial and time coordinates and let the differential equation and boundary condition to be solved take the form

$$\frac{\partial}{\partial x}u(x,t) - f(x) = 0, \qquad u(x,t_0) = u_{t_0}(x), \tag{1.40}$$

for some function $f(x)$, initial condition $u_{t_0}(x)$ and spatial domain $x \in [0, L]$ with boundary conditions

$$u(0,t) = u_0(t), \qquad u(L,t) = u_L(t), \tag{1.41}$$

for boundary functions $u_0(t)$ and $u_L(t)$, respectively. Solving this general differential equation using a FEM involves first deriving the so-called weak formulation of the governing equations by multiplying through by an arbitrary smooth function $v(x)$ that spans $[0, L]$ and integrating over the domain to result in

$$\int_0^L v(x)u'(x,t)\ \mathrm{d}x - \int_0^L v(x)f(x)\ \mathrm{d}x = 0, \tag{1.42}$$

where primes represent differentiation with respect to x and $v(x)$ is called the test function. Using integration by parts, this equation can be rewritten as

$$\Big[vu\Big]_0^L - \int_0^L v'(x)u(x,t)\ \mathrm{d}x = \int_0^L v(x)f(x)\ \mathrm{d}x. \tag{1.43}$$

In order to solve the equations, they now need to be discretised onto a computational 'element' mesh. The variable u is expanded in a series that approximates the solution to the differential equation (1.40) in terms of a finite number of (pre-determined) basis functions

$$u(x,t) \approx \sum_{i=1}^{N} w_i(x)u_i(t), \tag{1.44}$$

for the number of elements N, element index i, basis functions $w_i(x)$, and approximations to $u(x,t)$ on each element $u_i(t)$. Choosing appropriate basis functions depends on the type of problem being solved. Similar expressions for v and f are

$$v(x,t) \approx \sum_{i=1}^{N} w_i(x) v_i, \quad f(x,t) \approx \sum_{i=1}^{N} w_i(x) f_i. \tag{1.45}$$

By noting that only the basis functions w_i are dependent on x, the derivative with respect to x (denoted by dash notation) of one of these summations (using u as an example) is simply

$$\left(\sum_{i=1}^{N} w_i(x) u_i \right)' = \sum_{i=1}^{N} w_i'(x) u_i. \tag{1.46}$$

By introducing the matrix notation

$$[M]\{u\} \equiv \sum_{i=1}^{N} w_i(x) u_i, \tag{1.47}$$

$$[M']\{u\} \equiv \sum_{i=1}^{N} w_i'(x) u_i, \tag{1.48}$$

and then substituting the discretised variables (1.44) and (1.45) into the weak formulation (1.43) results in the matrix equation

$$\Big[\{v\}^T[M]^T[M]\{u\}\Big]_0^L - \int_0^L \{v\}^T[M']^T[M]\{u\}\ \mathrm{d}x = \int_0^L \{v\}^T[M]^T[M]\{f\}\ \mathrm{d}x. \tag{1.49}$$

As u_i and v_i are independent of x, the $[M]$ terms can be separated from the $\{u\}$ and $\{v\}$ terms which can be moved outside the integrals. As a result the test functions $\{v\}^T$ cancels (hence justifying why its choice was arbitrary) and the matrix equation becomes

$$\left(\Big[[M]^T[M]\Big]_0^L - \int_0^L [M']^T[M]\ \mathrm{d}x \right) \{u\} = \int_0^L [M]^T[M]\{f\}\ \mathrm{d}x. \tag{1.50}$$

Solving the differential equation (1.40) has hence been reduced to solving the matrix equation (1.50) using a numerical scheme of choice. The above description is for a linear problem. To extend the analysis to a more complicated problem with non-linear equations, such as the Navier-Stokes equations (1.1)–

(1.4), a similar process is employed. Instead of just solving an equivalent matrix equation (1.50) however, an iterative scheme is required, such as Newton's method (Galántai, 2000), which generates a sequence of linear problems whose solutions then converge to the correct solution of the non-linear problem (Wriggers, 2008).

1.2.2 Spectral methods

In the previous subsection, it was shown that a FEM makes use of a computational mesh on which the solution to the differential equation (1.40) is approximated. Typically, these approximations are of low order and as a result a very large mesh can be required to capture the relevant flow physics. A spectral method is a so-called global method, whereby the computation at any given point in the domain depends on information from the entire domain, rather than just from neighbouring points (like in a FEM). It therefore allows the use of a coarser grid by using higher order approximations to the differential equation being solved (Boyd, 2001).

Spectral methods approximate the solution to a differential equation for a variable u by using the series expansion

$$u(x,t) \approx u_N(x) \equiv \sum_{i=1}^{N+1} u_i(t)\phi_i(x), \tag{1.51}$$

where $\phi_i(x)$ are a set of N orthonormal basis functions. While this expansion is exact in the limit of $N \to \infty$, the physical limits of computational resources require truncating to some finite N. The choice of these basis functions can be a non-trivial problem and can depend on the equations being solved. An example of a set of basis functions that can be chosen are the Lagrange polynomials, given by

$$\ell_i^{(N)} \equiv \prod_{k=1,k\neq i}^{N+1} \frac{x - x_k}{x_i - x_k}, \tag{1.52}$$

such that the interpolating polynomial (1.51) becomes

$$u_N(x) = \sum_{i=1}^{N+1} u_i\, \ell_i^{(N)}(x). \tag{1.53}$$

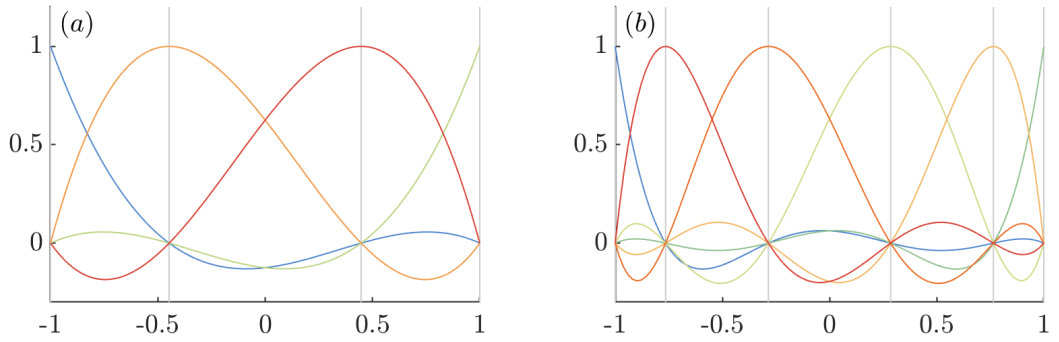

Figure 1.6: The Lagrange polynomials (1.52) for $N = 3$ (panel a) and $N = 5$ (panel b). Grey vertical lines illustrate the locations of the collocation points, given by maxima of the Lagrange polynomials. The figure illustrates that at each collocation point, one of the Lagrange polynomials has a value of one, while all the others are equal to zero.

The Lagrange polynomials (1.51) are one of the most commonly used sets of basis functions in spectral methods, and are in fact used by the code for the simulations in this thesis. The locations of the points of the computational grid (often referred to as collocation points) are hence given by the maxima of these polynomials. The Lagrange polynomials for $N = 3$ and for $N = 5$ are plotted in figure 1.6, illustrating that at each collocation point one polynomial has a value of one and all the others are equal to zero. The locations of these collocation points (i.e. the computational grid points) are indicated with vertical grey lines.

The spectral method algorithm then solves for the unknown basis coefficients u_i using a fast Fourier transform and makes use of what is known as 'spectral convergence', whereby the error decreases exponentially as N is increased, which results in high accuracy. One of the key disadvantages of spectral methods compared to FEM is the nature of the geometry required. A spectral method essentially requires a cuboidal geometry (in three dimensions) with mesh points specified by the basis functions. For modelling plumes, it is desirable to cluster mesh points in certain regions of the domain so as to capture the plume flow without needing to prescribe a high density of mesh points in a region with stagnant flow.

1.2.3 Spectral element methods (SEM)

Spectral element methods (SEM), first proposed by Patera (1984) are so called because they take inspiration from both FEM and spectral methods. They involve using the FEM to solve a differential equation like in section 1.2.1 but instead of using low-order basis functions w_i in (1.44) they use the high order basis functions, such as Lagrange polynomials (1.52) from the spectral method, like in (1.51). Essentially, this results in a small spectral method mesh within each finite element, therefore combining the high accuracy of spectral methods with the versatility of FEM. A simple, graphical illustration of example meshes for each method is given in figure 1.5.

One of the key benefits of using a SEM is that they exhibit very little numerical dispersion and dissipation. This is important for high Reynolds number flows, such as a turbulent plume. SEM also exhibit spectral convergence, whereby the error decreases exponentially with increasing polynomial order, and due to their high order basis functions, results in high accuracy with fewer degrees of freedom compared to a FEM (Deville et al., 2002).

1.2.4 Description of the code

The solver used to solve the discretised governing equations is the open source code Nek5000 (Fischer et al., 2007). It has been used previously by multiple authors to model jets and plumes (Peplinski et al., 2014; Fabregat Tomàs et al., 2016; Ezhova et al., 2017), and has been demonstrated to have excellent scalability on large numbers of cores (Offermans et al., 2016). The equations solved by Nek5000 are the Navier-Stokes and conservation of energy equations, written conventionally in the dimensionless form as

$$\frac{D\boldsymbol{u}}{Dt} = -\boldsymbol{\nabla} p + \frac{1}{Re^*}\nabla^2 \boldsymbol{u} + \boldsymbol{F}, \tag{1.54a}$$

$$\boldsymbol{\nabla} \cdot \boldsymbol{u} = 0, \tag{1.54b}$$

$$\frac{DT}{Dt} = \frac{1}{Pe^*}\nabla^2 T + Q_s, \tag{1.54c}$$

where $\boldsymbol{F}$ is a forcing term, Q_s is a source term, and $Re^* = UL/\nu$ and $Pe^* = UL/\kappa$ are a Reynolds number and Péclet number, respectively, for characteristic length L and velocity U scales.

Nek5000 makes use of a SEM decomposition of the Navier-Stokes equations, as discussed in section 1.2.3, to discretise in space. In time, the code is discretised using a semi-implicit method making use of a k-th order (in this thesis $k = 3$) backwards differencing and extrapolation schemes (referred to as the BDFk/EXTk scheme) (Boström, 2015). For a general time dependent problem

$$\frac{\partial \boldsymbol{U}}{\partial t} = \mathcal{L}[\boldsymbol{U}], \qquad \boldsymbol{U}(t_0, \boldsymbol{x}) = \boldsymbol{U}_0, \tag{1.55}$$

where $\mathcal{L}$ represents spatial operators. Then the backwards differencing scheme of order k (BDFk) approximates the partial time derivative as

$$\frac{1}{\Delta t} \sum_{i=0}^{k} \beta_i \boldsymbol{U}^{n+1-i} \approx \mathcal{L}[\boldsymbol{U}^{n+1}], \tag{1.56}$$

where $\boldsymbol{U}^n$ represents the solution at time step n, β_i are backwards differencing coefficients for $i = 1, \ldots, k$, and Δt is the time-step size. The advection terms in Navier-Stokes equations (1.54) are treated explicitly by using a high-order extrapolation on the non-linear terms. The k-th order extrapolation (EXTk) of a general non-linear term $\mathcal{L}(\boldsymbol{U}^{n+1})$ is

$$\mathcal{L}(\boldsymbol{U}^{n+1}) \approx \sum_{i=1}^{k} \alpha_i \mathcal{L}(\boldsymbol{U}^{n+1-i}), \tag{1.57}$$

where α_i are a set of extrapolation coefficients for $i = 1, \ldots, k$. Combining the two schemes (1.56) and (1.57) results in

$$\frac{1}{\Delta t} \sum_{i=0}^{k} \beta_i \boldsymbol{U}^{n+1-i} \approx \sum_{i=1}^{k} \alpha_i \mathcal{L}(\boldsymbol{U}^{n+1-i}). \tag{1.58}$$

The BDF3/EXT3 scheme (used for the simulations in this thesis) is order $\mathcal{O}(\Delta t^3)$ accurate (Fischer et al., 2016). When making use of an explicit time-stepping method, stability is maintained by restricting the ratio between the spatial-step and the time-step. The Courant-Friedrichs-Lewy (CFL) constraint ensures the stability of the time-stepping scheme by requiring that the Courant number

$$C = \frac{|\boldsymbol{u}|\Delta t}{\Delta x} < 0.5, \tag{1.59}$$

where $|\boldsymbol{u}|$ is the root mean square of the velocity and Δx is the largest spatial-

step in the domain.

1.3 Research questions and thesis summary

The problem of a plume emanating from a point source of heat in a quiescent, unstratified environment transitioning from its inception to laminar flow and through a transition to turbulent flow is investigated using various approaches of study, such as direct numerical simulations (DNS) and scaling analysis. Both these approaches of study are used to model a fully 3D laminar and turbulent plume in an unstratified environment with $Pr = 1$ and confirm descriptions of flow profiles in laminar and turbulent regimes in chapter 2. Firstly, a description of the height to instability for a plume generated by a point source of heat is investigated, addressing research question 1.

Research Question 1

What is the height to instability for a plume generated by a point source of heat?

A plume initialised from a point source will undergo a transition from laminar to turbulent flow. The location of this height to instability is currently an open question. The most related work in the literature is that discussed in section 1.1.3. Dombrowski et al. (2005) and Lombardi et al. (2011) both investigated the instability of plumes in a stratification and both studies focused on the initial time dependent instability of a plume emanating from a finite areal source. López Moscat & Marqués Truyol (2013) investigated the emergence of symmetries using a dynamical systems perspective.

The answer to this research question is distinguished from previous work as it considers the full spatial structure of a plume initialised at a point source, to a laminar regime, through an instability region with a quasi-steady height, and finally to a fully turbulent regime to determine the location of a universal height to instability for a plume in an unstratified environment. Direct numerical simulations and similarity theory are employed to answer this question in chapters 2 and 3.

Secondly, the location of the virtual origin for the turbulent regime of a plume emanating from a point source in an unstratified environment is investigated, addressing research question 2.

Research Question 2

Can a unified theory of a plume be developed, encompassing both laminar and turbulent sections and the transition between?

A unified theory of a plume would involve a laminar similarity solution (1.30)–(1.33) (Zeldovich, 1937; Yih, 1951), a turbulent similarity solution (1.35) (Zeldovich, 1937; Schmidt, 1941), and a quantitative description of how the former transitions into the latter. This can be achieved using the height to instability discussed in research question 1 and a virtual origin for the turbulent regime, describing the region over which the plume undergoes instability and transitions to turbulence.

There have been many studies predicting the virtual origins of plumes. Morton & Middleton (1973) and Hunt & Kaye (2001) both did so for lazy turbulent plumes, whereby the momentum deficit at the source needs resolving to a virtual origin. No previous work has been found, however, that investigates the location of the virtual origin of a turbulent plume resulting from a laminar plume undergoing a transition to turbulence.

A short study showing that the laminar portion of a plume emanating from a point source can be approximated using the laminar similarity solution (1.30)–(1.33) is conducted in chapter 2, addressing research question 3.

Research Question 3

How does a point source of heat evolve into a laminar plume?

This research question addresses the fundamental question of initialising a laminar plume. In (1.4), a source condition on the input of heat at a point was introduced. No work in the literature was found that investigates how a conductive source of a pure plume transitions into a (convective) plume. In answering research question 3 it will be shown that this condition can be replaced with relevant variables from the lam-

inar similarity solution (1.30)–(1.33) (Zeldovich, 1937; Yih, 1951) with negligible loss of information.

Finally in chapter 2, an investigation into the time-dependent plume regime comparing head and stem widths is conducted, addressing research question 4.

Research Question 4

How does the time-dependent front of a plume generated by a point source of heat evolve in time?

Before reaching a steady state, a plume generated by a point source of heat will evolve in time exhibiting a head-like structure in front of the laminar regime. There have been a number of studies that have focused on the time-dependent evolution of a plume. Moses et al. (1993), for example, suggested that the width of the laminar head at the front of the plume grows at the same rate as the stem, namely as $t^{1/2}$. In the high Prandtl number limit, Kaminski & Jaupart (2003) suggest that the initial rise speed is proportional to the bulk flow velocity (1.34) defined by Worster (1986).

In section 2.4.1, the hypothesis proposed by Moses et al. (1993) that the head expands as $t^{1/2}$ will be tested using the results of the DNS, and a new prediction will be proposed for head growth as a function of time. In section 3.3.3, a new theory of plume head ascent velocity is derived using a constraint on the total buoyancy flux in the plume.

The work from chapter 2 is then extended in two ways. Firstly, in chapter 3, to consider plumes in an unstratified environment, initialised at a point source, with varying viscosity and temperature diffusivity ratio (varying Prandtl numbers) to investigate the effect of Prandtl number on plume structure and the location of instability using DNS of a plume with $Pr \in [0.1, 2.0]$, addressing research question 5.

Research Question 5

How does the height to instability and the overall plume structure depend on the ratio of viscosity to thermal diffusivity?

The full spatial structure of a plume initialised at a point source, to a laminar regime, and through a steady instability to a turbulent regime will be shown to be dependent just on the ratio of viscosity to thermal diffusivity, namely the Prandtl number. DNS and scaling analysis will be used in chapter 3 to describe the dependence of this full structure on the Prandtl number.

Also in chapter 3, plumes in unstratified environments at low and high limits of Prandtl number are investigated, introducing a theory for the low $Pr \to 0$ limit, addressing research question 6.

Research Question 6

What is the behaviour of plumes in both the low and high limits of the ratio of viscosity to thermal diffusivity?

Worster (1986) investigated the limit of Prandtl number $Pr \to \infty$, however there has been little work on that of an inviscid plume, that of $Pr \to 0$. In section 3.3.1 the similarity equations for an inviscid plume are solved and compared to the full similarity equations (1.30)–(1.33) and high Prandtl number limit.

Secondly, the work in chapter 2 is extended in chapter 4 to consider plumes initialised at a point source in a stratification, where an investigation of the change in rise height and neutral buoyancy level with Reynolds number is undertaken, addressing research question 7.

Research Question 7

How do the maximum rise height and the neutral buoyancy of a plume in a stratification depend on viscosity?

Morton et al. (1956) produced the first description of the maximum rise height and the neutral buoyancy level (NBL) of a plume in a stratification for a fully turbulent plume, there has been little work, however, on the rise height and NBL of low-Re (laminar) and mid-Re number (transitional) plumes.

Xue et al. (2019) found a link between the rise height of negatively buoyant fountains and the Reynolds number using laboratory experiments. Dombrowski et al. (2005) found that rise height of a plume varies non-monotonically with inlet velocity and Lombardi et al. (2011) developed a scaling law for the rise height of two-dimensional plumes. On the other hand, there have been many studies of turbulent plumes in a stratification (Morton et al., 1956; Plourde et al., 2008; Devenish et al., 2010; Rooney & Devenish, 2014; Fabregat Tomàs et al., 2016), yet there has been little work on the steady maximum rise height and NBL of plumes over a range of Reynolds numbers spanning laminar to turbulent plumes.

In chapter 4, DNS of plume over a wide range of Reynolds numbers are investigated and the maximum rise height and NBL for each is described. A simple model of plume rise is developed using boundary layer theory to predict the steady maximum rise height and NBL for laminar plumes.

The relationship between height to instability and rise height for plumes in a stratification with varying viscosity at a fixed Prandtl number is also investigated in chapter 4, addressing research question 8.

Research Question 8

What is the relationship between the maximum rise height and height to instability for a plume in a stratification?

There has been little work on the steady transition to instability of a plume in a stratification and the relationship between maximum rise height of plumes and the height to instability. In chapter 4, DNS of plumes emanating from a point source into a linearly stratified environment, over a wide range of Reynolds numbers are investigated. This

study describes the relationship between the steady height to instability for plumes in unstratified environments, discussed in research question 1, and the maximum rise height of a plume.

Choosing an appropriate numerical Reynolds number for the numerical study of plumes in a stratification for large applications, such as volcanic eruptions, is also discussed in chapter 4, addressing research question 9.

Research Question 9

What numerical Reynolds number is appropriate for simulating the rise height of highly turbulent plumes?

In numerical investigations into turbulent plumes, many studies pick a large Reynolds number, often near the value of 7000 (Pham et al., 2007; Plourde et al., 2008; Fabregat Tomàs et al., 2016) to represent an often much larger Reynolds number. For example, in the case of a volcanic eruption the Reynolds number can be $> 10^6$ (Pyle, 1995). Few studies, however, discuss in much detail why this particular number was chosen with most studies suggesting it is high enough to produce the relevant flow physics. In chapter 4, this research question is investigated in an attempt to assert the lowest Reynolds number that will represent a high Reynolds number turbulent plume.

The theory of plume rise from a plume an unstratified environment developed in chapters 2 and 3 is applied to a model of aerosol transport in the indoor environment in chapter 5 to determine the time taken for particles to be dispersed within the height of a room, addressing research question 10.

Research Question 10

What are the implications of a hybrid laminar-turbulent plume transition for aerosol transport?

Previous studies of particle transport in plumes have often focused

on particle fallout and spread through the neutrally buoyant gravity current stage at a NBL of a turbulent plume (Sparks et al., 1991; Johnson et al., 2015; Sutherland & Hong, 2016). Few studies, however, have investigated the transport of particles in laminar and hybrid laminar-turbulent plumes. In chapter 5, the laminar (1.30)–(1.33) and turbulent (1.35) similarity solutions, combined with the height to instability and turbulent virtual origin, of a plume are used to make predictions of a combined hybrid laminar-turbulent theory of aerosol transport in the indoor environment.

Finally, conclusions from the preceding four chapters are drawn in chapter 6, summarising all presented work and detailing areas that require further research.

Chapter 2

A unified laminar-turbulent theory of plumes in an unstratified environment

Contents

In this chapter, I present a theoretical analysis addressing the fundamental flow of a pure plume generated by a localised buoyancy source, its subsequent transition to turbulence, and final structure comprising both laminar and turbulent regimes. As detailed in section 1.3, plumes have been

well studied at the end-member cases of laminar and turbulent flow. Both laminar and turbulent plumes have been described with similarity solutions, given by (1.30)–(1.33) (Zeldovich, 1937; Yih, 1951) and (1.35) (Zeldovich, 1937; Schmidt, 1941), respectively. As reviewed in section 1.1.3, instabilities in plumes have also been studied (Dombrowski et al., 2005; Lombardi et al., 2011; López Moscat & Marqués Truyol, 2013), but with little focus on the steady transition to instability linking the laminar and turbulent regimes. A key open research question involves locating this height to instability (research question 1), with another involving the description of the full structure of a plume emanating from a point source (research question 2).

The equations that govern the behaviour of a plume are presented and scaling arguments are used to perform a non-dimensionalisation that reveals the dependence of the flow on only one dimensionless variable, the Prandtl number. Using direct numerical simulations (DNS) combined with scaling analysis, the universal properties of a pure plume with $Pr = 1$ are established. The classical transition to instability of a plume generated by a point source of heat is investigated by systematically documenting the full evolution of a plume from inception at a point source of heat, through the development of the laminar plume, to the initiation of instability and the transience during instability, and finally to the statistically steady state comprising both laminar and turbulent regimes.

Initially, a theoretical model of a plume in an unstratified environment is introduced in section 2.1. A scaling analysis is then performed in section 2.2 to reveal the intrinsic scales and non-dimensionalise the governing equations. The details involved in modelling a plume using DNS are discussed in section 2.3, with a description of the evolution of a point source of heat into a laminar plume, research question 3, in section 2.3.3. The laminar boundary layer and similarity theory (Zeldovich, 1937; Yih, 1951) are presented and solved in section 2.4, and comparisons to the DNS are made to investigate the height to instability, addressing research question 1, and the time-dependent plume front, research question 4. In section 2.5 the instability and turbulent similarity theory (Zeldovich, 1937; Schmidt, 1941) are compared to the DNS, and a unified theory of a laminar-transitional-turbulent plume is developed, addressing research question 2. Finally, a summary of the final structure in dimensional form is included in section 2.6 and concluding remarks and further work are presented in section 2.7.

2.1 Modelling a plume emanating from a point source in an unstratified environment

The environment in which a plume resides is referred to as unstratified if its density is uniform. A plume in an unstratified environment admits a different similarity solution for the laminar (1.5) and turbulent (1.35) regimes, which can be analysed using scaling arguments (Zeldovich, 1937). In this section, the governing equations of a plume emanating from a point source in an unstratified environment are presented and analysed to derive important parameters, determine intrinsic scales, and to non-dimensionalise the governing equations.

In the case of a plume in an unstratified environment emanating from a point source at $\boldsymbol{x} = (0, 0, 0)$, as discussed in section 1.1 and illustrated schematically in figure 2.1, the flow is modelled using the Navier-Stokes equations and energy conservation equation (1.1)–(1.4) subject to the Boussinesq approximation

$$\frac{D\boldsymbol{u}}{Dt} = -\frac{\boldsymbol{\nabla} p}{\rho_0} + \nu \nabla^2 \boldsymbol{u} + g\beta T \hat{\boldsymbol{z}}, \tag{2.1a}$$

$$\boldsymbol{\nabla} \cdot \boldsymbol{u} = 0, \tag{2.1b}$$

$$\frac{DT}{Dt} = \kappa \nabla^2 T, \tag{2.1c}$$

where $\boldsymbol{x} = (x, y, z)$ is the position vector, t is time, $\boldsymbol{\nabla}$ is the gradient operator, $\boldsymbol{u}(\boldsymbol{x}, t) = (u, v, w)$ is the fluid velocity, p is the fluid pressure, ρ_0 is a reference density, ν is the kinematic viscosity, $T(\boldsymbol{x}, t)$ is the temperature difference from the ambient, κ is the thermal diffusivity, β is the coefficient of thermal expansion, and g is acceleration due to gravity.

The solution to the equations is considered in the semi-infinite region $z \geq 0$ subject to no-slip and insulation conditions at $z = 0$, given by

$$\boldsymbol{u}(x, y, 0, t) = \boldsymbol{0}, \qquad \frac{\partial T}{\partial n}(x, y, 0, t) = 0, \tag{2.2}$$

respectively. In the far-field of the domain (encompassing both the limits of $x, y \to \infty$ for $z \geq 0$ and $z \to \infty$), it is assumed that the fluid is stagnant and that the temperature is given by the ambient value, as specified by

$$\lim_{R \to \infty} \boldsymbol{u} = \boldsymbol{0}, \qquad \lim_{R \to \infty} T = 0, \tag{2.3}$$

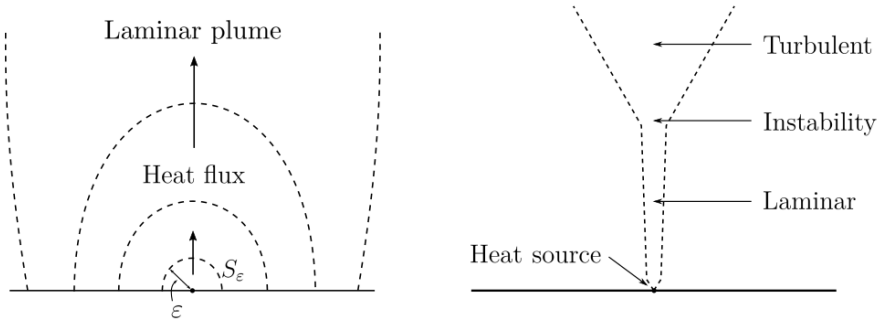

Figure 2.1: Representation of source conditions and overview of the plume flow. (Left) Zoomed in view of the point source illustrating the diffusive source region with an illustration of the hemisphere S_ε of radius ε in (2.4) and the transition to a laminar plume as advection becomes a dominant transport mechanism. (Right) Overview of a steady plume in an unstratified environment with transition from a diffusive heat source to laminar flow, to laminar-turbulent instability, and finally to a turbulent plume.

where $R = \sqrt{x^2 + y^2 + z^2}$ is the spherical radial coordinate. To prescribe the source of buoyancy, the point-source condition of constant thermal flux,

$$\lim_{\varepsilon \to 0} \int_{S_\varepsilon} r \left(-\kappa \frac{\partial T}{\partial n} \right) \, \mathrm{d}S = F_0, \tag{2.4}$$

is imposed, where $r = \sqrt{x^2 + y^2}$ is the cylindrical radial coordinate, S_ε is the hemisphere of radius $R = \varepsilon$ in the region $z \geq 0$ (illustrated in figure 2.1), and F_0 is the prescribed buoyancy source flux.

2.1.1 Plume fluxes

It should be noted that (2.4) differs from the more typical source condition applied in studies of laminar or turbulent plumes, given in (1.9) (Morton et al., 1956; Brand & Lahey, 1967; Worster, 1986). In this subsection, the equation for the width-averaged buoyancy flux F at a given height z is derived from the temperature conservation equation (2.1c), and is shown to consist of both advective and convective terms. In section 2.3.3 it will be shown that the assumption of an advective buoyancy flux is justified and that the convective term can be neglected at a height sufficiently far above the point source.

The equations governing the behaviour of a plume emanating from a point source were introduced in (2.1)–(2.4). For convenience in specify-

ing source conditions, and as plumes exhibit axisymmetric behaviour when averaged temporally, cylindrical coordinates are used to specify the source fluxes. Vertical velocity and temperature are written as $w = w(r, \varphi, z, t)$ and $T = T(r, \varphi, z, t)$, respectively. Making use of the product rule of differentiation and using incompressibility (2.1b), the temperature conservation equation (2.1c) is rewritten as

$$\frac{\partial T}{\partial t} + \boldsymbol{\nabla} \cdot \left(T\boldsymbol{u} - \kappa \boldsymbol{\nabla} T \right) = 0, \tag{2.5}$$

resulting in the definition of the heat flux $\boldsymbol{q}(r, \varphi, z, t) = \rho_0 c_p \left(T\boldsymbol{u} - \kappa \boldsymbol{\nabla} T \right)$, where c_p is the specific heat capacity of the fluid. Partitioning the heat flux into radial, azimuthal, and vertical parts, and assuming that the flow is steady, it holds that

$$\boldsymbol{\nabla} \cdot \boldsymbol{q} = \boldsymbol{\nabla} \cdot \left(q_r \hat{\boldsymbol{r}} + q_\varphi \hat{\boldsymbol{\varphi}} + q_z \hat{\boldsymbol{z}} \right) = \frac{1}{r} \frac{\partial}{\partial r} \left(r q_r \right) + \frac{1}{r} \frac{\partial q_\varphi}{\partial \varphi} + \frac{\partial q_z}{\partial z} = 0. \tag{2.6}$$

Multiplying through by r and integrating with respect to radius and azimuthal direction results in the heat flux through a horizontal plane (with normal in the z-direction)

$$\int_0^{2\pi} \int_0^{\infty} \frac{\partial}{\partial r} \left(r q_r \right) + \frac{\partial q_\varphi}{\partial \varphi} + r \frac{\partial q_z}{\partial z} \, \mathrm{d}r \, \mathrm{d}\varphi = 0. \tag{2.7}$$

Evaluating the radial integral over the first term and the azimuthal integral over the second term and rearranging results in

$$2\pi \left[r q_r \right]_0^{\infty} + \int_0^{\infty} \left[q_\varphi \right]_0^{2\pi} \, \mathrm{d}r + \frac{\partial}{\partial z} \int_0^{2\pi} \int_0^{\infty} r q_z \, \mathrm{d}r \, \mathrm{d}\varphi = 0. \tag{2.8}$$

The zero far field conditions (2.3), and the periodicity of q_φ, reveal that the radial and azimuthal terms are zero. Substituting in the z component of $\boldsymbol{q}$ results in

$$\frac{\partial}{\partial z} \left(\rho_0 c_p \int_0^{2\pi} \int_0^{\infty} r \left(T w - \kappa \frac{\partial T}{\partial z} \right) \, \mathrm{d}r \, \mathrm{d}\varphi \right) = 0. \tag{2.9}$$

It is more convenient when studying plumes to use the buoyancy flux instead of the heat flux. To make this conversion the term inside the derivative

in (2.9) is multiplied by the group $g\beta/\rho_0 c_p$ (Gill, 1982), resulting in an equation for the width-averaged buoyancy flux

$$F(z,t) = \int_0^{2\pi}\int_0^{\infty} g\beta r\left(Tw - \kappa\frac{\partial T}{\partial z}\right)\,\mathrm{d}r\,\mathrm{d}\varphi \equiv F_A(z,t) + F_C(z,t), \tag{2.10}$$

which, due to (2.9), is constant with height in an unstratified environment. Included are both the advective and conductive contributions to the buoyancy flux, denoted $F_A(z,t)$ and $F_C(z,t)$, respectively. Studies of both laminar and turbulent plumes to date have generally assumed that $F \equiv F_A$ uniformly, with an advectively specified input condition $F(0,t) \equiv F_A$. The purely conductive condition $F(0,t) = F_C$ assumes nothing about the form of the generated plume (whether turbulent or laminar), of the amount of turbulence already present, nor of the details of an inflow geometry. The boundary condition at the point source of a pure plume is hence given by

$$F(0,t) = F_C(0,t) \equiv \lim_{\varepsilon\to 0}\int_{S_\varepsilon} r\left(-\kappa\frac{\partial T}{\partial n}\right)\,\mathrm{d}S = F_0, \tag{2.11}$$

where F_0 is a prescribed buoyancy flux representing the rate of thermal input, S_ε is the hemisphere of radius $R = \varepsilon$ in the region $z \geq 0$, and n is the normal to the surface of the hemisphere S_ϵ.

By calculating the values of $F_A(z,t)$ and $F_C(z,t)$ in (2.10) for a simulation near the source, it is demonstrated in section 2.3.3 that in the region above the source, outside of the diffusive region near the point source, that F_C can be neglected as fluid transport due to advection dominates diffusion, see figure 2.7. The buoyancy flux used in both the laminar and turbulent plume regions is therefore approximated by the advective buoyancy flux with negligible loss of accuracy

$$F(z,t) = F_A(z,t) \equiv \int_0^{2\pi}\int_0^{\infty} g\beta r T w\,\mathrm{d}r\,\mathrm{d}\varphi. \tag{2.12}$$

This integral is used in conjunction with similarity theory (introduced in section 1.1.1) in later sections to initialise a laminar plume directly, without having to model the diffusive source. It is also used in both laminar and turbulent regimes to make comparisons between simulations and theory (Yih, 1951; Morton et al., 1956).

While not appearing explicitly in the model, it is useful to consider the volume Q and momentum M fluxes, as they are common in many studies of plumes. For example Morton et al. (1956) base their plume model on volume, momentum, and buoyancy flux. They are given by

$$Q(z,t) = \int_0^{2\pi}\int_0^{\infty} rw \ \mathrm{d}r \ \mathrm{d}\varphi, \qquad M(z,t) = \int_0^{2\pi}\int_0^{\infty} rw^2 \ \mathrm{d}r \ \mathrm{d}\varphi, \tag{2.13}$$

and are used later in the analysis for comparison between theory and simulations in both the laminar and turbulent regimes.

2.2 Intrinsic scales and nondimensionalisation

The system (2.1)–(2.4) is dependent on a total of five parameters: ρ_0, ν, $(g\beta)$, κ and F_0. By performing a scaling analysis to determine the intrinsic scales and subsequently using them to non-dimensionalise, the five-way dependence can be reduced to a dependence on just a single parameter.

Firstly, the intrinsic scales for length $\boldsymbol{x} \sim L$, time $t \sim \tau$, and temperature $T \sim \mathcal{T}$ are defined. By comparing the the advective and forcing terms in (2.1a), the advective and diffusive terms in (2.1c), and the terms in (2.10), the following scaling relationships are uncovered

$$L \sim g\beta\mathcal{T}\tau^2 \qquad L^2 \sim \kappa\tau, \qquad F_0 \sim g\beta\frac{\mathcal{T}L^3}{\tau}. \tag{2.14}$$

By rearranging these scaling relationships, the following scales for length, time, and temperature are derived

$$L = \left(\frac{\kappa^3}{F_0}\right)^{1/2}, \qquad \tau = \frac{\kappa^2}{F_0}, \qquad \mathcal{T} = \frac{1}{\beta g}\left(\frac{F_0^3}{\kappa^5}\right)^{1/2}, \tag{2.15}$$

respectively. The model in (2.1) is subsequently non-dimensionalised by defining the dimensionless variables, denoted by hats,

$$\boldsymbol{x} = L\hat{\boldsymbol{x}}, \quad t = \tau\hat{t}, \quad \boldsymbol{u} = \frac{L}{\tau}\hat{\boldsymbol{u}}, \quad p = \rho_0\left(\frac{L}{\tau}\right)^2\hat{p}, \quad T = \mathcal{T}\hat{T}, \tag{2.16}$$

and substituting. On dropping hats, (2.1) becomes

$$\frac{D\boldsymbol{u}}{Dt} = -\boldsymbol{\nabla} p + Pr\nabla^2\boldsymbol{u} + T\hat{\boldsymbol{z}}, \tag{2.17a}$$

$$\boldsymbol{\nabla}\cdot\boldsymbol{u} = 0, \tag{2.17b}$$

$$\frac{DT}{Dt} = \nabla^2 T, \tag{2.17c}$$

where the single controlling dimensionless parameter, defined by $Pr = \nu/\kappa$, is the Prandtl number. The no-slip and far-field conditions, (2.2) and (2.3), remain unchanged in form, namely,

$$\boldsymbol{u}(x, y, 0, t) = \boldsymbol{0}, \qquad \frac{\partial T}{\partial n}(x, y, 0, t) = 0, \tag{2.18}$$

and

$$\lim_{R\to\infty} \boldsymbol{u} = 0, \qquad \lim_{R\to\infty} T = 0, \tag{2.19}$$

respectively. The source condition (2.4), after substitution of (2.16), becomes

$$\lim_{\varepsilon\to 0} \int_{S_\varepsilon} r\left(-\frac{\partial T}{\partial n}\right)\, \mathrm{d}S = 1. \tag{2.20}$$

The fluxes in section 2.1.1 are also non-dimensionalised using the scales in (2.15). The full description of both the advective and diffusive buoyancy flux in (2.10) becomes

$$F(z,t) = \int_0^{2\pi}\int_0^{\infty} r\left(Tw - \frac{\partial T}{\partial z}\right)\, \mathrm{d}r\, \mathrm{d}\varphi \equiv F_A(z,t) + F_C(z,t), \tag{2.21}$$

and the dimensionless forms of the advective source fluxes in (2.12) and (2.13) become

$$F_A(z,t) = \int_0^{2\pi}\int_0^{\infty} rTw\, \mathrm{d}r\, \mathrm{d}\varphi, \tag{2.22}$$

$$Q(z,t) = \int_0^{2\pi}\int_0^{\infty} rw\, \mathrm{d}r\, \mathrm{d}\varphi, \tag{2.23}$$

$$M(z,t) = \int_0^{2\pi}\int_0^{\infty} rw^2\, \mathrm{d}r\, \mathrm{d}\varphi. \tag{2.24}$$

The dimensionless system (2.17)–(2.20) describes the initialisation, development, and full structure of a plume generated at a sustained point source of heat in a given unstratified fluid at a given Prandtl number Pr. As the system is shown to be dependent only on this one dimensionless number, pure plumes in unstratified environments can therefore be classified entirely in terms of the Prandtl number alone. As the Prandtl number depends purely on the material properties of kinematic viscosity ν and thermal diffusivity κ of the fluid under consideration, the form of the solution to (2.17)–(2.20) is universal for a given material subject to a scaling by (2.15). For example, all plumes generated in a quiescent unstratified body of water will be equivalent up to a multiplication by the relevant scales in (2.15).

Initially, in order to simplify the problem and not study a range of Prandtl numbers, just a single Prandtl number is studied in this chapter. I pick the case for $Pr = 1$, as it simplifies the equations and is of the order of magnitude for most gases. In chapter 3 the work is extended and the structure and asymptotic elements of pure plumes generated over a range of Prandtl numbers is investigated.

2.2.1 Laminar regime

There have been multiple previous studies of the laminar plume regime, as discussed in the introduction in section 1.1.1. The governing equations (2.17)–(2.20) can be simplified by using boundary layer theory and by noting the existence of a similarity solution (Zeldovich, 1937; Yih, 1951). A review of the derivation of the similarity solution for the dimensional case was performed in section 1.1.1, for the dimensionless case the process is very similar, resulting in the same laminar similarity system (1.30)–(1.33)

$$-f\left(\frac{f'}{\eta}\right)' = Pr\left(\eta\left(\frac{f'}{\eta}\right)'\right)' + \eta h, \tag{2.25a}$$

$$h' = -\frac{1}{\eta}fh, \tag{2.25b}$$

with boundary conditions

$$\lim_{\eta\to 0}\left(-\frac{1}{\eta}f'(\eta) + f''(\eta)\right) = 0, \qquad \lim_{\eta\to 0}\left(f(\eta) - \frac{1}{2}\eta f'(\eta)\right) = 0, \tag{2.26}$$

as $\eta \to 0$ and far field conditions

$$f' = 0, \qquad h = 0, \qquad \text{as } \eta \to \infty, \tag{2.27}$$

with the buoyancy flux condition

$$2\pi \int_0^\infty h f' \, \mathrm{d}\eta = 1. \tag{2.28}$$

To convert from similarity variables f and h back into dimensionless vertical velocity w, temperature T, and radial velocity u, the dimensional stream function and temperature (1.26) can be substituted into the definition of the stream function (1.23) and nondimensionalised using the relationships in (2.16) to result in

$$w = \frac{1}{\eta} f'(\eta), \qquad T = z^{-1} h(\eta) \qquad u = z^{-1/2} \left(\frac{1}{2} f'(\eta) - \frac{1}{\eta} f(\eta) \right), \tag{2.29}$$

which can then be used, after solving the laminar similarity equations (2.25)–(2.28) to make comparisons to the solutions to the DNS of (2.17)–(2.20).

The dimensionless laminar similarity equations (2.25)–(2.28) are solved using a shooting method. A shooting method involves reducing a boundary value problem to an initial value problem, then trying different 'initial conditions', using an iteration procedure, until the original boundary conditions are satisfied. The shooting parameters $s_f = f'(0)$ and $s_h = h(0)$ are iterated through two bisection methods, using (2.27) and (2.28) as success conditions. To solve this system numerically, the system is reframed as a set of four ODEs by defining $\mathcal{F}_0 := f$, $\mathcal{F}_1 := f'$, $\mathcal{F}_2 = f''$, and $\mathcal{H}_0 := h$ and substituting into (2.25b) and an expanded version of (2.25a), resulting in the system

$$\frac{\mathrm{d}\mathcal{F}_0}{\mathrm{d}\eta} = \mathcal{F}_1, \tag{2.30a}$$

$$\frac{\mathrm{d}\mathcal{F}_1}{\mathrm{d}\eta} = \mathcal{F}_2, \tag{2.30b}$$

$$\frac{\mathrm{d}\mathcal{F}_2}{\mathrm{d}\eta} = Pr \left(\frac{1}{\eta^2} \mathcal{F}_0 \mathcal{F}_1 - \frac{1}{\eta} \mathcal{F}_0 \mathcal{F}_2 - \eta \mathcal{H}_0 \right) - \frac{1}{\eta^2} \mathcal{F}_1 + \frac{1}{\eta} \mathcal{F}_2, \tag{2.30c}$$

$$\frac{\mathrm{d}\mathcal{H}_0}{\mathrm{d}\eta} = -\frac{1}{\eta} \mathcal{F}_0 \mathcal{H}_0, \tag{2.30d}$$

with two of the shooting initial conditions derived by rewriting $s_f = f'(\eta_0)$ and $s_h = h(\eta_0)$ in $\mathcal{F}$ and $\mathcal{H}$ form, and two by substituting s_f and s_h into (2.26) for some η_0 close to zero

$$\mathcal{F}_0(\eta_0) = \frac{\eta_0 s_f}{2}, \qquad \mathcal{F}_1(\eta_0) = s_f, \qquad \mathcal{F}_2(\eta_0) = \frac{s_f}{\eta_0}, \qquad \mathcal{H}_0(\eta_0) = s_h. \quad (2.31)$$

The far field (2.27) and buoyancy flux (2.28) conditions are used as success conditions for the shooting methods, requiring that they be satisfied to a tolerance of

$$|\mathcal{F}_1(\eta_{max})| < 10^{-5}, \qquad |\mathcal{H}_0(\eta_{max})| < 10^{-5}, \quad (2.32)$$

and

$$\left| 2\pi \int_0^\infty \mathcal{H}_0 \mathcal{F}_1 \, \mathrm{d}\eta - 1 \right| < 10^{-5}, \quad (2.33)$$

respectively. The shooting values s and t are iterated through a bisection search using the integration of (2.30)–(2.31) which is computed using the integrator `ode15s` (Shampine & Reichelt, 1997) in MATLAB subject to the far field conditions (2.32) and the buoyancy flux condition (2.33).

The solutions of w, zT, and $z^{1/2}u$, derived from the solutions to the laminar similarity equations using (2.29), are plotted in figure 2.2. These solutions inform the profiles of velocity and temperature at a given height, z. This solution can be compared to higher-level numerical simulations for verification, and is used to initialise the plume at a given height above the point source rather than resolving the diffusive heat source condition (discussed later in section 2.3.3).

2.3 Direct numerical simulation of a full laminar-turbulent plume

The system (2.17)–(2.20) is now solved for $Pr = 1$ using direct numerical simulations (DNS) using the open source, spectral element method (SEM) code Nek5000 (Fischer et al., 2008). This code has been demonstrated to have an excellent scalability to a large number of computational nodes and

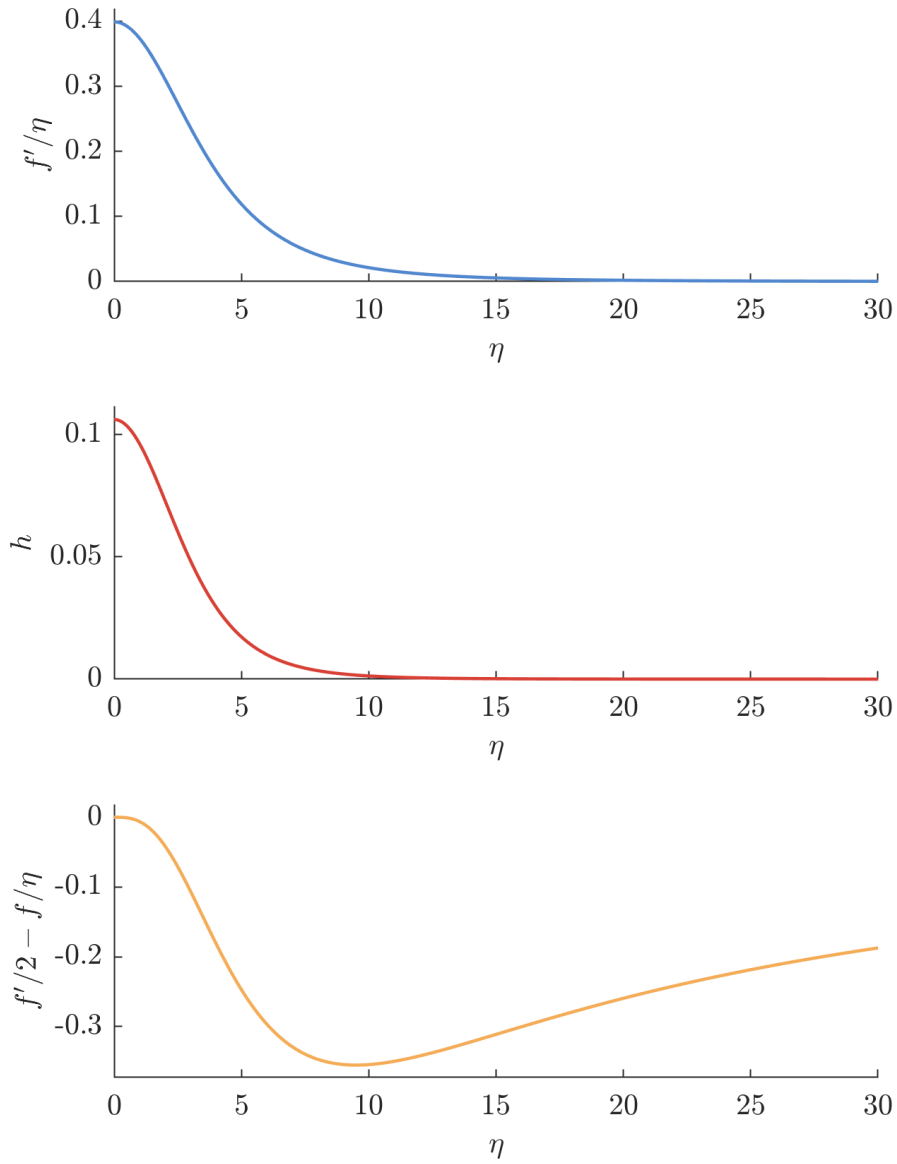

Figure 2.2: Solutions of the model described in (2.30) and (2.31). (Top) Solution for the vertical velocity f'/η $(= w)$. (Middle) Solution for the similarity form of the temperature h $(= zT)$. (Bottom) Solution for the similarity form of the radial velocity $\frac{1}{2}f' - f/\eta$ $(= z^{-1/2}u)$. The equations are solved using two iterative bisection methods to ensure that s and t are chosen such that the far field condition (2.32) and buoyancy flux condition (2.33) are satisfied.

has been validated in a wide range of turbulent flows (Peplinski et al., 2014; Fabregat Tomàs et al., 2016; Offermans et al., 2016; Ezhova et al., 2017). The SEM allows for high-order solutions in complex geometries by making use of the advantages of both finite element methods and spectral methods. An overview of the SEM and a description of the solver Nek5000 is included in section 1.2.

This section details the modelling of a plume in Nek5000. A description of the domain and boundary conditions is included in section 2.3.1 and a mesh sensitivity study is included in section 2.3.2. A short investigation into verifying that the solution to the similarity equations (2.25)–(2.28) can be used to initialise a laminar plume is undertaken in section 2.3.3, followed by the relevant source conditions with which to initialise a laminar plume in section 2.3.4. Finally, a description of the plume evolution and structure is presented in section 2.3.5, describing the results of the DNS. An illustration of the process required to run a direct numerical simulation of a plume in Nek5000 is presented in appendix A.

2.3.1 Simulation set-up

The computational domain is specified as a cylinder with the source located in the centre of the lower circular base. Given the nondimensionalisation based on intrinsic scales, it might be expected that the domain size should be of order unity. Initial tests indicated, however, that the height over which the instability and transition to turbulence occurred was much larger. Therefore, the radius of the domain is chosen to be $r_e = 1.6 \times 10^5$ and the height is chosen to be $z_e = 8 \times 10^5$. As per the SEM, the domain is spatially discretised into a mesh of N_{el} elements. The elements of the mesh are clustered towards the centre of the domain and towards the source using a geometric progression. The elements are then fanned outwards from the centre and subsequently repositioned to reduce aspect ratios of the elements. A schematic illustrating the mesh is included in figure 2.3. By virtue of the SEM, the elements are further sub-divided using Legendre polynomials up to the pth order.

At the top and sides of the simulation domain, the Neumann bound-

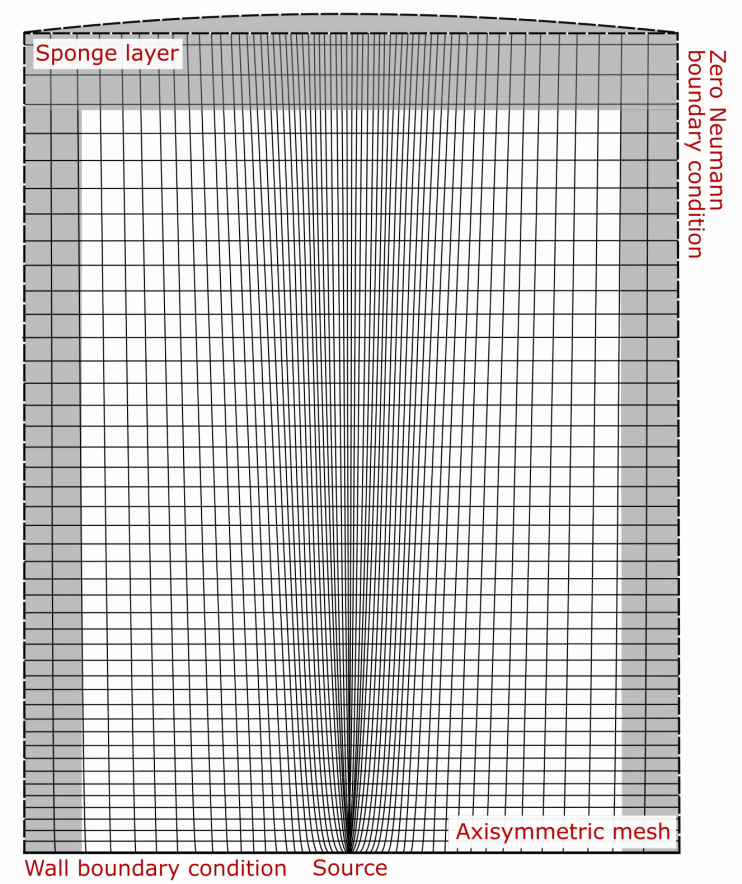

Figure 2.3: An illustration of an example element mesh (without spectral, higher order basis functions included), clustered near the source and in the centre. The wall boundary conditions at the base are given by (2.18), the zero Neumann boundary conditions at the sides are given by (2.34), and the greyed out area represents the sponge region, given by (2.35) and illustrated in more detail in figure 2.4.

ary conditions

$$\frac{\partial \boldsymbol{u}}{\partial n} = 0, \qquad \frac{\partial T}{\partial n} = 0, \tag{2.34}$$

are applied, representing an insulating, smooth boundary. Numerical instabilities at these outflow boundary conditions, caused by turbulent eddies moving through the boundary, are suppressed by implementing a numerical 'sponge' in which the viscosity in the far-field regions is artificially increased nearer the domain edge to dampen any turbulent eddies that may pass through the domain boundaries and cause numerical instabilities. Following Jiang & Luo (2000) and Pant & Bhattacharya (2016), a sponge layer is implemented by prescribing a spatially variable $Re_*(r, z)$ in the equations used in the Nek5000

solver (1.54) according to

$$Re_*(r,z) = \overline{Re}_* \left[1 + \gamma_s \left(2 + \operatorname{erfc}\left(\frac{\beta_z(z-z_e)}{z_e - z_{\min}}\right) + \operatorname{erfc}\left(\frac{\beta_r(r-r_e)}{r_e - r_{\min}}\right)\right)\right]^{-1}, \tag{2.35}$$

where $\overline{Re}_*$ is the specified Reynolds number in the majority of the simulation domain, $\operatorname{erfc}(x) = 2/\sqrt{\pi}\int_x^\infty \exp(-t^2)\,\mathrm{d}t$ is the error function, β_z and β_r represent the characteristic thickness of the sponge layers, and z_e, $z_{\min}$, and r_e, $r_{\min}$ are the maximum and minimum values of the z and r coordinates within the simulation domain, respectively. In all simulations in this thesis, $z_{\min} = r_{\min} = 0$. The above specifies that the Reynolds number of the fluid decreases (and hence the damping increases) in a narrow band along the exterior of the domain from the bulk value by a factor of γ_s to the wall of the domain. The value of $Re_*(r,z)$ for fixed $z = 4\times10^5$, halfway up the domain, is plotted in figure 2.4. A sponge thickness of $\beta_z = \beta_r = 20$ and a viscosity factor of $\gamma_s = 10$ were found to be sufficient to suppress instabilities, with the region $z_s < z < 7.5\times10^5$ and $r < 1.4\times10^4$ deemed to be unaffected by the presence of the sponge layer. The location of the sponge layer is illustrated with grey shading in figure 2.3. All plots in this chapter are hence cut off at these levels by default.

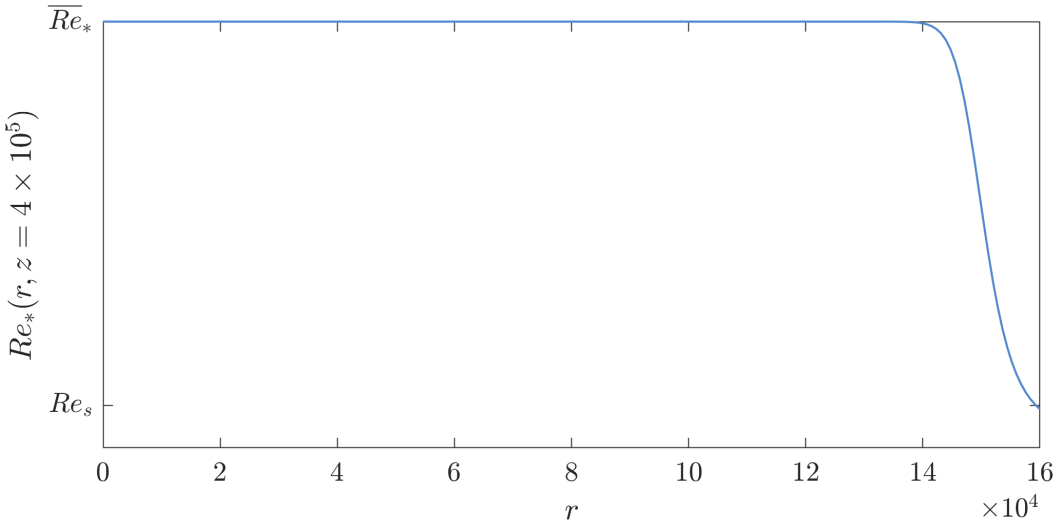

Figure 2.4: A plot of the spatially variable Reynolds number (2.35) in the r-direction (at fixed $z = 4\times10^5$) used to produce the sponge layer. The value of Re_* varies from the bulk value $\overline{Re}_*$ to the value of the Reynolds number in the furthest extent of the sponge region Re_s as shown.

2.3.2 Mesh sensitivity

To attempt to establish the degree of convergence of the DNS to the size of the computational grid, a mesh sensitivity study was performed on the plume flow. A series of simulations of (2.17)–(2.20) for the case $Pr = 1$ were conducted to test the sensitivity of the final height of instability z_* to the resolution of the computational mesh. In order to test the contribution of numerical errors to the seeding of noise in the simulation domain, we allow for a numerical forcing applied to the Navier-Stokes equations (2.17)–(2.20) such that (2.17a) becomes

$$\frac{D\boldsymbol{u}}{Dt} = -\boldsymbol{\nabla} p + Pr\nabla^2\boldsymbol{u} + \boldsymbol{f}, \tag{2.36}$$

where the forcing term

$$\boldsymbol{f} = A \begin{pmatrix} \sin(k_x x + \omega t)\sin(k_y y + \omega t)\sin(k_z z + \omega t) \\ \sin(k_x x + \omega t)\sin(k_y y + \omega t)\sin(k_z z + \omega t) \\ T \end{pmatrix}, \tag{2.37}$$

where A is the amplitude of disturbance, k_x, k_y, k_z, and ω are wave numbers in x, y, z, and time t, respectively.

ID	$N_p\,(\times 10^6)$	p	$N_{el}\,(\times 10^4)$	$z_*\,(\times 10^5)$	A	$k_x = k_y = k_z$	ω
A0	6.75	5	5.4	4.0	0.0	1.0	0.5
A1	6.75	5	5.4	3.9	1.0	1.0	0.5
B0	10.3	5	8.4	5.1	0.0	1.0	0.5
B1	10.3	5	8.4	5.2	1.0	1.0	0.5
C0	18.5	7	5.4	5.2	0.0	1.0	0.5

Table 2.1: Meshes used in the mesh sensitivity study of the DNS solving (2.17)–(2.20) for $Pr = 1$, where the parameter $N_p = p^3 N_{el}$ represents the number of degrees of freedom (the number of elements multiplied by the order of the polynomials cubed), and z_* is the height to instability reported in each simulation. For all simulations, the radius of the domain is $r_e = 1.6 \times 10^5$ and the height is $z_e = 8 \times 10^5$. For the application of the disturbance in (2.37), A is the amplitude of the disturbance, and k_x, k_y, k_z, and ω are wave numbers in x, y, z, and time t, respectively. The value of the vertical velocity calculated from the laminar similarity solution (2.25)–(2.28) is $w_0 = 0.40$.

A list of simulations performed is included in table 2.1, each set up as detailed in section 2.3.1. The 'size' of the mesh N_p, representing the number

of degrees of freedom, is defined by $N_p = p^3 N_{el}$, where N_{el} is the number of elements in the mesh and p is the order of the polynomials across each element. For every simulation detailed in table 2.1 the radius of the domain is $r_e = 1.6 \times 10^5$ and the height of the domain is $z_e = 8 \times 10^5$. In applying the disturbance (2.37) for both simulations A1 and B1, the amplitude $A = 1.0$ the wave numbers $k_x = k_y = k_z = 1.0$, and $\omega = 0.5$. In simulations A0, B0, and C0 the amplitude of the disturbance $A = 0$.

For the simulation of each mesh in table 2.1, the height at which the centreline vertical velocity of the plume drops below $w_0/2$ (where $w_0 = 0.40$ is the value of vertical velocity calculated in the laminar similarity solution of (2.25)–(2.28) for $Pr = 1$ in section 2.2.1) is used as a proxy for height to instability. In figure 2.5, a showcase from simulation A0 is presented, comparing centreline vertical velocity with a contour plot of vertical velocity. The vertical dashed line in plot (b) indicates $w_0/2$, while the horizontal dashed lines indicate the height at which the centreline vertical velocity drops below $w_0/2$. As there is a significant drop off of the centreline vertical velocity as the plume transitions from laminar to turbulent flow, using the $w_0/2$ condition results in an accurate prediction of the height to instability, illustrated by the horizontal dashed line in the contour plot. The value of height to instability is then plotted against time in figure 2.6 for each simulation in table 2.1. By averaging the height to instability for each simulation after the curve has been determined to have stopped increasing, the quasi-steady height to instability z_* is extracted and plotted in solid black over each curve, hence determining the value of z_* in table 2.1.

The values of z_* between simulations A0 and A1, and B0 and B1 respectively, differ by $< 2.5\%$ in each case, hence revealing that the value of z_* does not vary significantly with an application of disturbance to the plume flow. Figure 2.6 shows that the increase in rise height from simulations A to B (increasing mesh resolution) is not due to numerical noise produced by the discretization of the mesh. By introducing a small, but significant, quantity of noise to the forcing term (2.37) in the governing equations (2.17)–(2.20), and therefore seeding the plume with small disturbances, the minimal change in z_* shows that the height to instability is not significantly sensitive to a lack of noise. In other words, the laminar plume regime will not continue to rise indefinitely with increasing resolution as any symmetry realised in the mesh is broken by the implementation of noise.

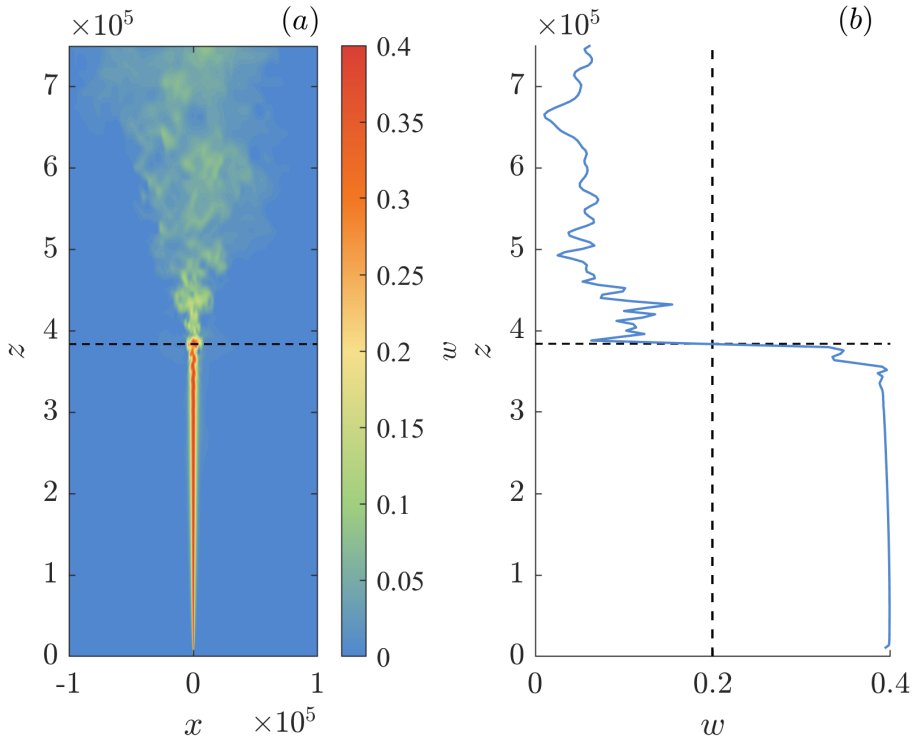

Figure 2.5: Comparison of a contour plot through a vertical slice (a) with the centreline vertical velocity (b), both at time $t = 2 \times 10^7$ for the DNS of (2.25)–(2.28) for simulation A0 (see table 2.1). The vertical dashed line in plot (b) is located at $w_0/2$ (where $w_0 = 0.40$ is the value of vertical velocity calculated in the laminar similarity solution of (2.25)–(2.28)) and the horizontal dashed line spanning both plots indicates the height at which the centreline vertical velocity drops below $w_0/2$. These plots indicate that the $w_0/2$ condition accurately predicts the height to instability.

Figure 2.6 also illustrates that mesh A, of size $N = 6.75 \times 10^6$, predicts a 25% change in the value of height to instability z_* from mesh A to B, whereas there is minimal change in z_* between meshes B and C, confirming numerical convergence of the solution and meaning that mesh B, of size $N = 10.3 \times 10^6$, is sufficient for using DNS to predict z_* for a plume in the current domain configuration with radius $r_e = 1.6 \times 10^5$ and height $z_e = 8 \times 10^5$.

The results used for further analysis in this chapter, particularly of the turbulent region, are those on mesh A. In figure 2.6 the curve for mesh B has a value of $z_* = 5.2 \times 10^5$, meaning that between the height to instability and the sponge layer beginning at a height of $z = 7.5 \times 10^5$, there is not enough height to sufficiently analyse the turbulent plume region. The current results on mesh A are qualitatively accurate, and as can be seen in figure 2.6, only vary by about 25% from the value for mesh B, hence resulting in results for

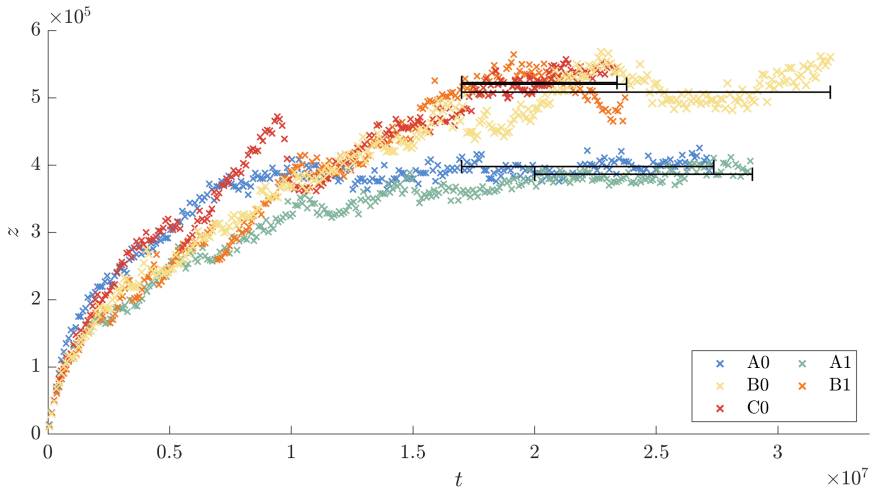

Figure 2.6: Mesh sensitivity study using height at which the centreline vertical velocity of the plume drops below $w_0/2$ (where $w_0 = 0.40$ is the value of vertical velocity calculated in the laminar similarity solution of (2.25)–(2.28)) for the DNS of (2.17)–(2.20) for each mesh in table 2.1. See figure 2.5 for an illustration of this condition. The legend refers to simulations detailed in table 2.1 and solid black lines represent the time window over which each simulation has been averaged and the average value.

the turbulent region in the rest of the chapter subject to a margin of error.

2.3.3 Plume formation from a point source of heat

In order to investigate the height to instability of a laminar plume and the subsequent turbulent region, the transitional scale on which the initial point source of heat becomes a laminar flow needs to be resolved, i.e. research question 3. In answering this question, it can be shown that the flow can be initialised directly in the laminar plume regime at some height $z = z_s \geq z_H$, where $z_H > 0$ is the height above which there is negligible loss of information when initialising the flow in the laminar plume regime.

For a dimensionless plume in an unstratified environment the buoyancy flux is equal to one at the point source (2.20), yet the velocity is equal to zero. In other words, temperature is transmitted by conduction only, and not convection. After this initial diffusive regime, just above the point source (represented by the elongation of hemispheres in figure 2.1), convection begins to occur. Because both advection and diffusion are present here, the definition

of the dimensionless buoyancy flux (2.21) must include both

$$F(z,t) = \int_0^{2\pi}\int_0^{\infty} r\left(Tw - \frac{\partial T}{\partial z}\right)\,\mathrm{d}r\,\mathrm{d}\varphi \equiv F_A(z,t) + F_C(z,t). \tag{2.38}$$

As discussed earlier, previous theoretical studies of both laminar and turbulent plumes have typically imposed that the buoyancy flux is purely advective uniformly for the full height of the plume, namely that $F \equiv F_A$. In a near source region, diffusion dominates the flow, velocity is negligible and hence F_A is also negligible, leaving the buoyancy flux condition at the point source at $z = 0$ as $F(0,t) = F_C = 1$. In the region further away from the source, as the velocity of the plume increases, advection dominates the flow and F_C becomes negligible, leaving $F(z,t) = F_A$ for $z > z_H$ for some (as yet undefined) characteristic height z_H.

The switch from conductive to convective regimes is evidenced in the results of DNS of (2.17)–(2.19) with the buoyancy flux condition

$$\frac{\partial T}{\partial z} = \lim_{r_s \to 0} \frac{1}{\pi r_s^2}, \tag{2.39}$$

where r_s is the radius of the hemisphere S_ϵ satisfying the point source condition (2.20). The radius of the simulation domain is chosen to be $r_e = 300$ and the height is chosen as $z_e = 350$. As a point source cannot be resolved by a discrete simulation mesh, the radius of the hemisphere S_ϵ for the DNS of (2.17)–(2.20) is chosen to be the small and non-zero $r_s = 1.6$ in order to demonstrate the evolution from conductive to convective regimes. The domain is spatially discretised into a mesh with $N_{el} = 7560$ elements with a polynomial order of 7, the elements are clustered towards the centre of the domain in order to sufficiently resolve the source. Boundary conditions at the edges of the domain are the same as in section 2.3.1 and the simulation was run until the flow reached a steady state.

Results of this simulation are presented in figure 2.7, where panels (b) and (c) are half-domain contour plots of vertical velocity and log temperature to illustrate the flow. Figure 2.7(a) combines plots of the advective F_A, conductive F_C, and full F buoyancy fluxes in (2.38). The full buoyancy flux $F(z,t)$ remains approximately equal to one for the full height of the domain (within 2%). Initially, the dominant contribution to F is the conductive buoyancy flux

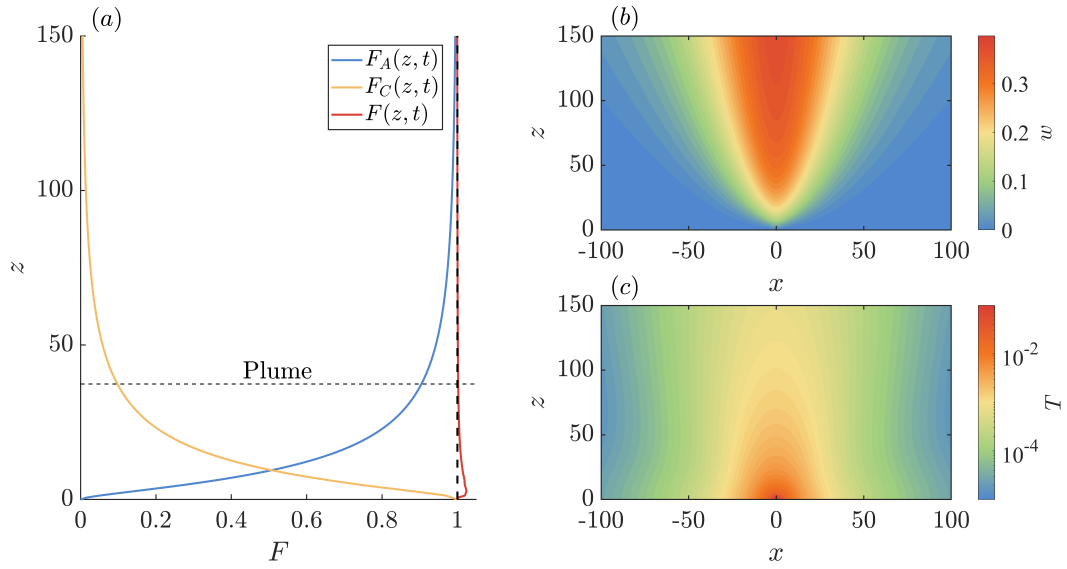

Figure 2.7: DNS of (2.17)–(2.20) to illustrate the initial development of the steady flow of a plume from the purely conductive source condition (2.20). In (a) the advective F_A, convective F_C, and full F buoyancy fluxes are calculated from the DNS solution, using (2.38), and compared. In (b) and (c) contour plots of vertical velocity and log temperature are plotted to illustrate the flow. The total buoyancy flux $F(z,t)$ remains approximately equal to the specified buoyancy flux (within 2%) at the source, non-dimensionalised to unity. Initially, the dominant contribution is the conductive buoyancy flux, but within just 40 dimensionless height units, F_C has dropped to $\sim 10\%$ of the full buoyancy flux and the flow can be said to approximate a plume defined by dominantly advective transport, as described by the laminar similarity theory (section 2.4).

F_C, but within only about 100 dimensionless height units, the contribution of the advective buoyancy flux F_A has become completely dominant. The small discrepancy in $F(z,t)$ near the source is expected to be due to a step in the definition of the source, which is defined for $r < r_s = 1.6$ using a top-hat condition. After only approximately 25 dimensionless height units, the full buoyancy flux $F(z,t)$ is within 0.5% of $F_0 = 1$. Despite this small discrepancy near the source, the argument can still be made that the advective buoyancy flux F_A takes over after only about 100 dimensionless height units and hence a plume can be imposed with only an advective heat source, using the laminar similarity solution (2.25)–(2.28), with negligible loss of information at a dimensionless height of $z_s > z_H \approx 100$.

The work in this section constitutes a description of the evolution of a point source of heat into a laminar plume. This hence results in an answer to research question 3, namely that flow generated by a point source of heat

can be approximated by the solution to the laminar similarity equation (2.25)–(2.28) after only approximately 100 dimensionless spatial units for $r_s = 1.6$ and $Pr = 1$. This result will be used to initialise the simulations in the laminar regime for the rest of chapters 2 to 4.

2.3.4 Source conditions at the displaced origin

The condition given in (2.20) defines the buoyancy flux through a hemisphere as $\epsilon \to 0$, representing a point source condition. As a numerical simulation involves calculating the solution to the governing equations on a discrete grid, a point source cannot be represented in a numerical simulation. Indeed, even in the previous section it was approximated as a small hemisphere. One way of solving this is to make use of the solution to the laminar similarity equations (2.25)–(2.28). The details of the numerical solver are provided in section 2.2.1. The similarity solution, illustrated in figure 2.8, informs the profile of the solution at a given height above the point source, thereby facilitating the specification of the boundary conditions at a new, displaced origin at $z = z_s$ in the boundary layer regime. The height of the displaced origin z_s must be chosen to be sufficiently smaller than the height to instability to allow the transient head region at the front of the plume to develop. These new conditions will also play the role of replacing the diffusive flux condition (2.20) with the convective flux condition $F_A(0,t) = 1$ from (2.21). This assumption was justified in section 2.3.3.

Many previous studies suggest that Gaussian profiles are good approximations of vertical velocity and temperature in turbulent plumes (Nakagome & Hirata, 1977; George Jr et al., 1977; Papanicolaou & List, 1988; Shabbir & George, 1994; Devenish et al., 2010; Plourde et al., 2008; Van Reeuwijk et al., 2016). It is important to note that all of these studies were of turbulent plumes. Nonetheless, it might be expected that a Gaussian profile would be a sufficient approximation to the vertical velocity and temperature profiles in laminar plumes. This assumption looks fairly good on inspection of the solution to the similarity equations (2.25)–(2.28) in figure 2.8 (solid curves). However, when compared against fitted Gaussians

$$w_G(\eta) = 0.39e^{-0.049\eta^2}, \qquad T_G(\eta) = 0.10e^{-0.081\eta^2}, \tag{2.40}$$

found using MATLAB's Fit function, in figure 2.8 (dashed lines), there is a significant difference between the curves for $2 \lesssim \eta \lesssim 15$, where $\eta = rz^{-1/2}$ is the similarity parameter, after non-dimensionalisation using the scales (2.15), first defined in (1.22).

By contrast, using a fitted spline to represent the solution to the laminar similarity equations (2.25)–(2.28), plotted in figure 2.8 as crosses, gives a much better agreement with the similarity solution (2.25)–(2.28) than the Gaussian (2.40). The splines are a set of k third-order piecewise continuous polynomials mapping values from an interval to the set of real numbers, namely $S_{(w)}, S_{(z^{1/2}u)}, S_{(zT)} : [0, \eta_{\max}] \to \mathbb{R}$, they are defined by

$$S_{(w)}(\eta) = \begin{cases} P_1(\eta) = a_1\eta^3 + b_1\eta^2 + c_1\eta + d_1, & 0 \le \eta < \eta_2, \\ P_i(\eta) = a_i\eta^3 + b_i\eta^2 + c_i\eta + d_i, & \eta_i \le \eta < \eta_{i+1} \text{ for } i = 2, ..., k-1, \\ P_k(\eta) = a_k\eta^3 + b_k\eta^2 + c_k\eta + d_k, & \eta_k \le \eta < \eta_{\max}, \end{cases} \tag{2.41}$$

and similarly for $S_{(z^{1/2}u)}$ and $S_{(zT)}$. The coefficients a_i, b_i, c_i, d_i are determined using MATLAB's splinefit function to fit k polynomials to the similarity solution (2.25)–(2.28) for w, u, and T. Writing $\eta = rz_s^{-1/2}$ and using the dimensionless form of the similarity variables (2.29) allows w, u, and T to be written in terms of the splines at the displaced origin

$$w_s(r) = S_{(w)}(rz_s^{-1/2}), \tag{2.42a}$$
$$u_s(r) = z_s^{-1/2} S_{(z^{1/2}u)}(rz_s^{-1/2}), \tag{2.42b}$$
$$T_s(r) = z_s^{-1} S_{(zT)}(rz_s^{-1/2}). \tag{2.42c}$$

The fit (2.42) is then used in all future simulations to define the profile of the vertical velocity, horizontal velocity, and temperature at the plume source. As a result, all modelled plumes are initialised directly in the laminar regime, without need for a transition to the laminar similarity solution.

Time displacement

By applying the displaced source condition, it is assumed that the region $0 < z < z_s$ is given virtually by the laminar similarity solution (2.25)–(2.28) (with z_s chosen small compared to the height of instability). As a result, the domain

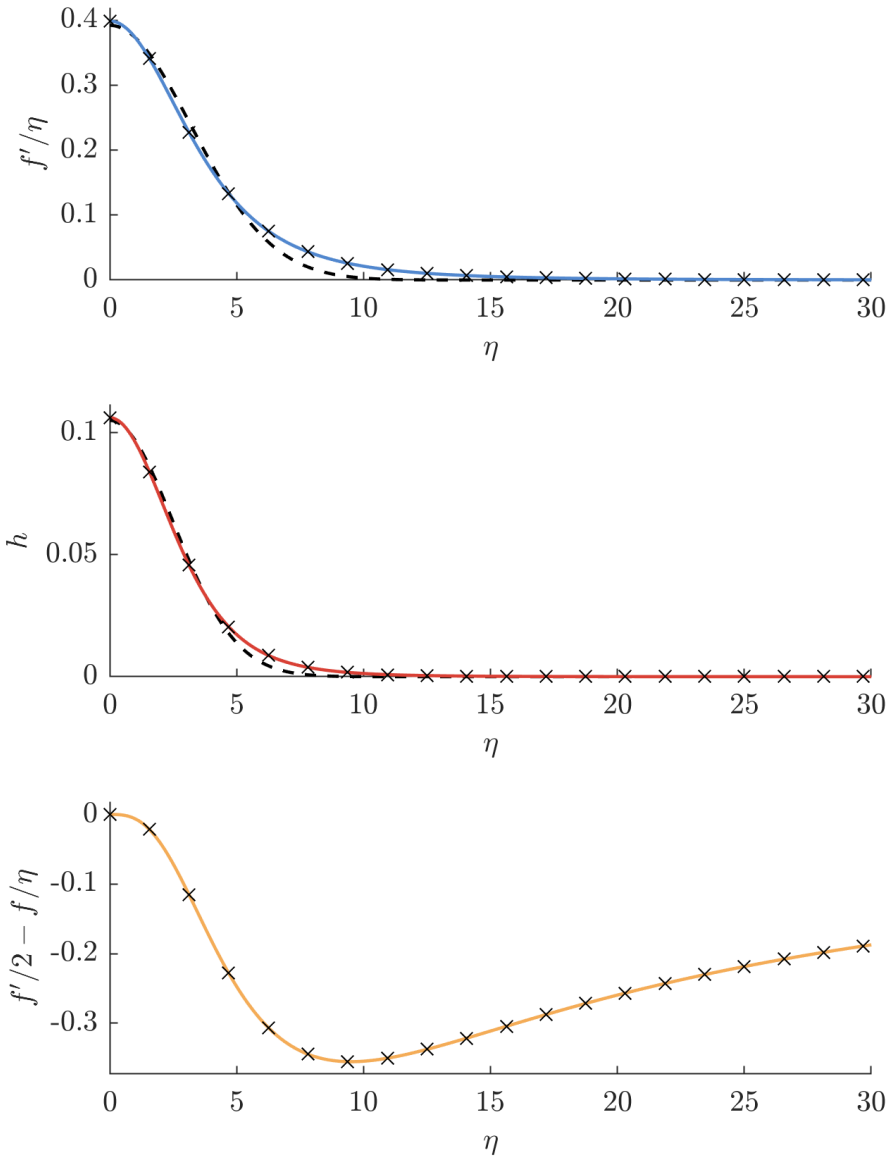

Figure 2.8: Solutions of the similarity equations (2.25)–(2.28), compared with a fitted Gaussian (2.40) (dashed) and a fitted spline (2.41) (crosses) to illustrate that the similarity solution differs from a Gaussian significantly in the tail region of the plume. From top to bottom, the curves are of the similarity form of the vertical velocity, temperature, and horizontal velocity. The fitted spline fits the similarity solution so well that the difference between the numerical solution to the similarity solution and the spline is not visible on these plots. In the bottom plot, a Gaussian is not fitted to the data as the curve is fundamentally the wrong shape.

already contains a small quantity of total buoyancy at the time at which the simulation is initiated t_s. To derive the total buoyancy, firstly the advective buoyancy flux F (2.22) is integrated with respect to time. As the buoyancy flux is equal to one at the source, the integration yields that the integral is linear with t

$$\int_0^t \int_0^{2\pi} \int_0^{\infty} rTw \, \mathrm{d}r \, \mathrm{d}\varphi \, \mathrm{d}t = t. \tag{2.43}$$

Changing the order of integration and making a substitution of variables using that $w = \partial z/\partial t$ results in

$$\int_0^{2\pi} \int_0^{\infty} \int_0^{z(t)} rT \, \mathrm{d}z \, \mathrm{d}r \, \mathrm{d}\varphi = t. \tag{2.44}$$

By defining the total buoyancy $B(t)$ in the domain up to a height of $z(t)$ to be the left hand side of (2.44) at time t, it holds that

$$B(t) \equiv \int_0^{z(t)} \int_0^{2\pi} \int_0^{\infty} Tr \, \mathrm{d}r \, \mathrm{d}\varphi \, \mathrm{d}z = t. \tag{2.45}$$

In order for the total buoyancy to be zero at $t = 0$, as required if the simulation is initiated at the displaced origin $z = z_s$ at some time $t = t_s$, the time origin is shifted to account for the existing buoyancy $B(t_s)$ already in the domain at the initiation of the simulation. Substituting the similarity variables (2.29) into (2.45) and conducting the z integral results in the displaced time t_s at the displaced origin z_s

$$t_s = z_s \left(2\pi \int_0^{\infty} h(\eta)\eta \, \mathrm{d}\eta \right) = z_s E(Pr), \tag{2.46}$$

where $E(Pr)$ is defined to be the term in the parentheses. Solving the similarity equations (2.25)–(2.28) and evaluating the function $E(Pr)$ for $Pr = 1$ results in $E(1) \approx 5.01$.

The height of the displaced origin for simulations in this chapter is chosen to be $z_s = 10^4$. The corresponding time shift is $t_s \approx 5 \times 10^4$, calculated using (2.46). The data in all plots (excluding figure 2.7) are given by the

simulations for times $t > t_s$ and heights $z > z_s$. The period $0 < t < t_s$ and region $0 < z < z_s$ are represented virtually by the laminar prediction, denoted by dashed lines in figures 2.9 and 2.10 and left implicit in subsequent figures.

2.3.5 Illustration of plume evolution and structure

As a preliminary illustration of the evolution of a plume, the numerical solution to the system (2.17)–(2.20) is considered for the case $Pr = 1$. Figure 2.9 illustrates the initial transient evolution of a plume in an unstratified environment from a laminar source, through laminar flow to turbulent flow. Initially, the plume exhibits a slender laminar stem that grows with time, this will be shown to be consistent with the laminar similarity solution to (2.25)–(2.28) in section 2.4. At the top, the plume has a growing spherical head, evident in figure 2.9(a). This head then undergoes an instability at a dimensionless height of $z \approx 1.2 \times 10^5$ in figure 2.9(b) and the laminar region extends further in height in figure 2.9(c,d), approaching a steady position of instability above which the plume becomes fully turbulent (evidenced in figure 2.10).

Figure 2.10 illustrates the initial transience and the final statistically steady-state behaviour of the plume. In the top panel, the figure shows a sequence of contour plots of the vertical velocity w in the rz cross-section over a progression of increasing times, like in figure 2.9. Figure 2.10(a,b) illustrate the same behaviour as in figure 2.9. After the initial instability, the speed of the head decreases and a transition region connecting laminar to turbulent flow develops. The plume above this transition region is turbulent, yet the laminar region extends through the initial instability at z_t (fig. 2.9(c,d)) and settles at a height of $z_* \approx 3.9 \times 10^5$ (fig. 2.10(d)), thus addressing research question 1. The height to instability z_* is determined as described in section 2.3.2, by finding the height at which the vertical velocity along the vertical centreline drops below $w_0/2$, where $w_0 = 0.40$ is the centreline vertical velocity predicted by the solution to the laminar similarity equations (2.25)–(2.28) for $Pr = 1$. After this height to instability, the lower part of the plume can be said to be in a statistically steady state.

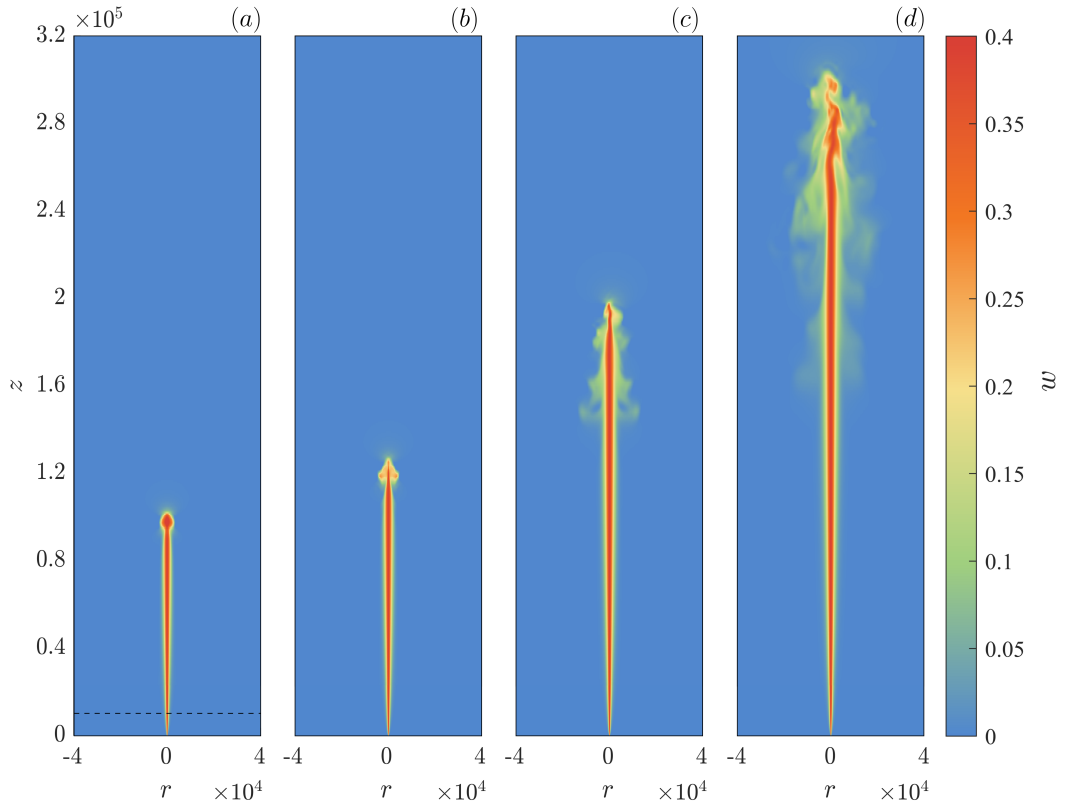

Figure 2.9: Evolution of a plume generated by a point source of heat, as predicted by the DNS of (2.17)–(2.20) for $Pr = 1$ in the early time stages to illustrate the initial instability (simulation A in table 2.1). In panel (a), at dimensionless time $t = 5.0 \times 10^5$, the plume is fully laminar, exhibiting a slender main section connected to an ovular head. In plot (b), at $t = 7.5 \times 10^5$, instability has taken place locally at the plume head, causing the ovular head to transition into a more complex, yet still axisymmetric, form. In plot (c), at $t = 1.6 \times 10^6$, the instability has moved higher and is exhibiting signs of asymmetry. Plot (d), at $t = 3.4 \times 10^6$, shows the continued development of the unstable head and remnants of the instability accumulating to the sides of the plume stem. In all plots the solution to the similarity equations (2.25)–(2.28) has been added for the region $z < z_s = 10^4$, represented by the dashed line in panel (a).

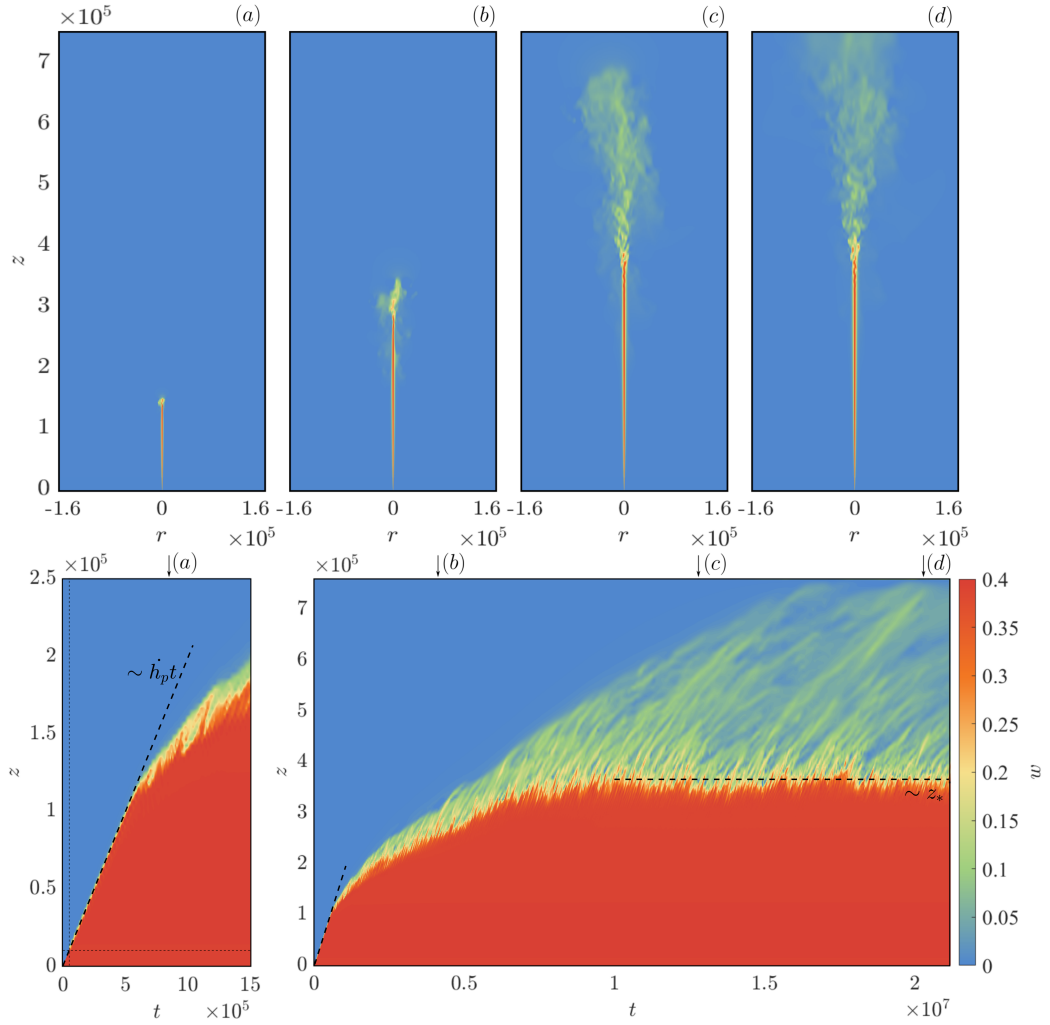

Figure 2.10: Evolution of a plume, as predicted by the DNS of (2.17)–(2.20) for $Pr = 1$ (simulation A in table 2.1). The plots (a-d) show the vertical velocity field w in the rz cross-section, the similarity solution (2.25)–(2.28) for the vertical region $z < z_s = 10^4$ has been added to each plot. In panel (a), at dimensionless time $t = 8.1 \times 10^5$, the first signs of instability have started to occur. In plot (b), at $t = 4.1 \times 10^6$, the instability has translated higher and the laminar region has increased in height. In plot (c), at $t = 1.28 \times 10^7$, the location of the instability has settled at a height of $z \approx 3.9 \times 10^5$ and the turbulent region has begun to develop. In plot (d), at $t = 2.08 \times 10^7$, the plume has reached a quasi-steady state. In the lower half of the figure the vertical velocity along the vertical centreline is plotted against time, the solution to (2.17)–(2.20) prior to the spatial and temporal virtual origins have been added using the similarity solution (2.25)–(2.28) for $z < z_s = 10^4$ and $t < t_s \approx 5{\times}10^4$, respectively, indicated by the dashed lines in the left-hand plot. The arrows above indicate the time of each plot (a-d). The left-hand plot is a zoomed in region to better illustrate early time behaviour, the laminar plume rises linearly in this region, represented by the dashed line with a gradient of $\dot{h}_p \approx 0.2$. The position where this line departs from the contour indicates the head instability, at a height of $z_t \approx 1.2{\times}10^5$. The steady instability is indicated with a horizontal dashed line located at a height of $z = z_* \approx 3.9 \times 10^5$, which is determined by finding the height at which the centreline vertical velocity drops below $w_0/2$, where $w_0 = 0.40$ is the centreline vertical velocity predicted by the solution to the laminar similarity equations (2.25)–(2.28) for $Pr = 1$.

Interestingly, in undertaking a short study to attempt to shortcut to the steady flow (like in figure 2.10(d)), it was discovered that the time-dependent height to instability $z_*(t)$ rises in response to an accumulation of fluid in the head-like structure ahead of it. The simulation performed involved initialising the domain with the full laminar similarity solution (2.25)–(2.28) at time $t = 0$, figure 2.11(a) shows a contour just a short time after initialisation. What resulted was the majority of the laminar plume structure exhibiting instability down to a height much lower than the predicted steady $z_* = 3.9 \times 10^5$, evident in figure 2.11(c). The time-dependent height to instability then continues to rise as previously, as can be seen in the progression of figure 2.11(d,e,f) and the build up of a new time-dependent head. This indicates that the time dependent evolution has a dependence on the flow ahead of it. In other words, the location of the long-term height to instability z^* is strongly dependent on the accumulation of buoyant, mixed fluid directly above it, which is dependent on the long-term nonlinear evolution. Hence, a linear stability analysis would not produce accurate predictions of the height to instability z^*. The need to accumulate buoyant, mixed fluid in order for the plume to progress explains the protracted growth of the height to instability $z_*(t)$ shown in figure 2.10 as it grows towards its final value.

The results presented here demonstrate both a temporal and spatial regime transition from a laminar to turbulent plume. In the laminar region, boundary layer and similarity theory (Zeldovich, 1937; Yih, 1951), presented in (2.25)–(2.28), can be used to simplify the equations, make scaling arguments, and verify the numerics. This simplified theory also facilitates the specification of boundary conditions immediately in the laminar region rather than resolving the point source, as discussed in section 2.3.3. In the turbulent region, similarity theory (Zeldovich, 1937; Schmidt, 1941) can be used to make scaling arguments to make flow predictions and validate the numerics.

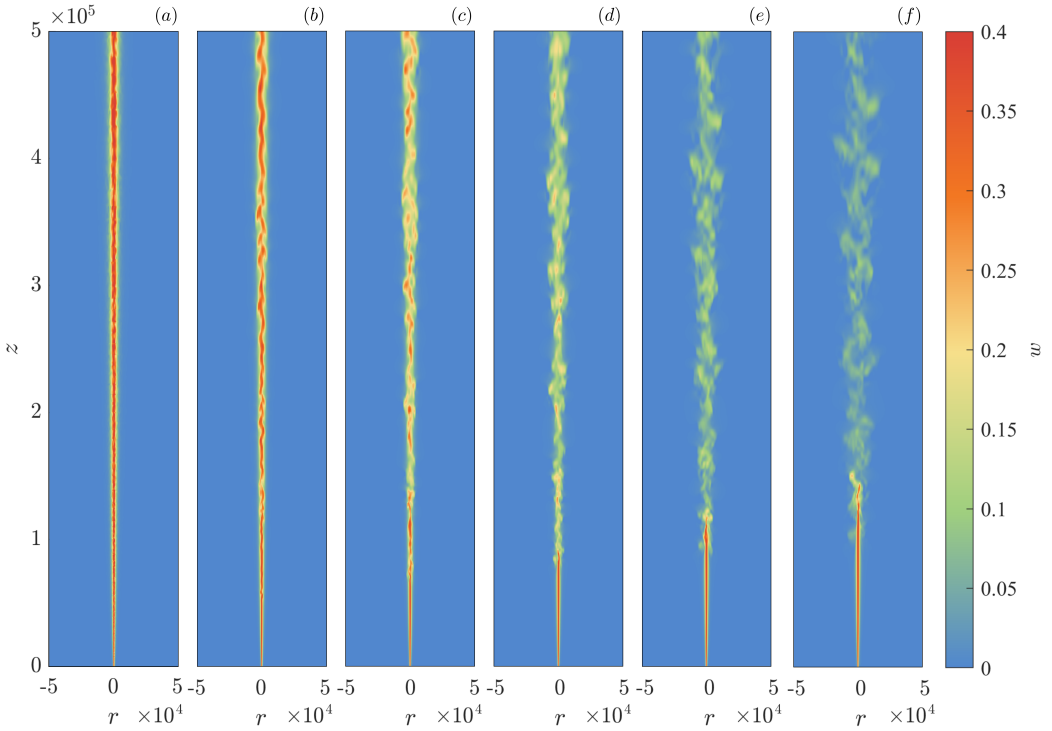

Figure 2.11: Evolution of a plume, as predicted by the DNS of (2.17)–(2.20) for $Pr = 1$, initialised with the laminar similarity solution (2.25)–(2.28) through the full height of the domain at times (a) $t = 2.0 \times 10^2$, (b) $t = 2.0 \times 10^5$, (b) $t = 3.0 \times 10^5$, (d) $t = 4.0 \times 10^5$, (e) $t = 6.0 \times 10^5$, and (f) $t = 8.7 \times 10^5$. Initial instabilities are present through the majority of the height of the plume in panel (a), growing larger in panels (b) and (c). By panel (d) it can be seen that the steady laminar region is maintained to a height of $z \approx 10^5$, after which, in panels (e) and (f), the laminar region appears to push through the instability, building a turbulent head like in the conventional study.

2.4 Laminar regime

As illustrated by the DNS of (2.17)–(2.20) in section 2.3.5, a plume emanating from a point source in an unstratified environment exhibits first a fully laminar starting plume, that subsequently develops a turbulent head, followed by a steady laminar plume up to an instability to the turbulent regime. In this section, laminar similarity theory is used to validate the DNS and make predictions about the flow.

The solution to the similarity equations (2.25)–(2.28) in the (r, z) coordinate system (1.26) is compared to the DNS in figure 2.12. As a check on the accuracy of the DNS, and to examine the conditions for the emergence of a region in which the boundary-layer approximation applies both during the

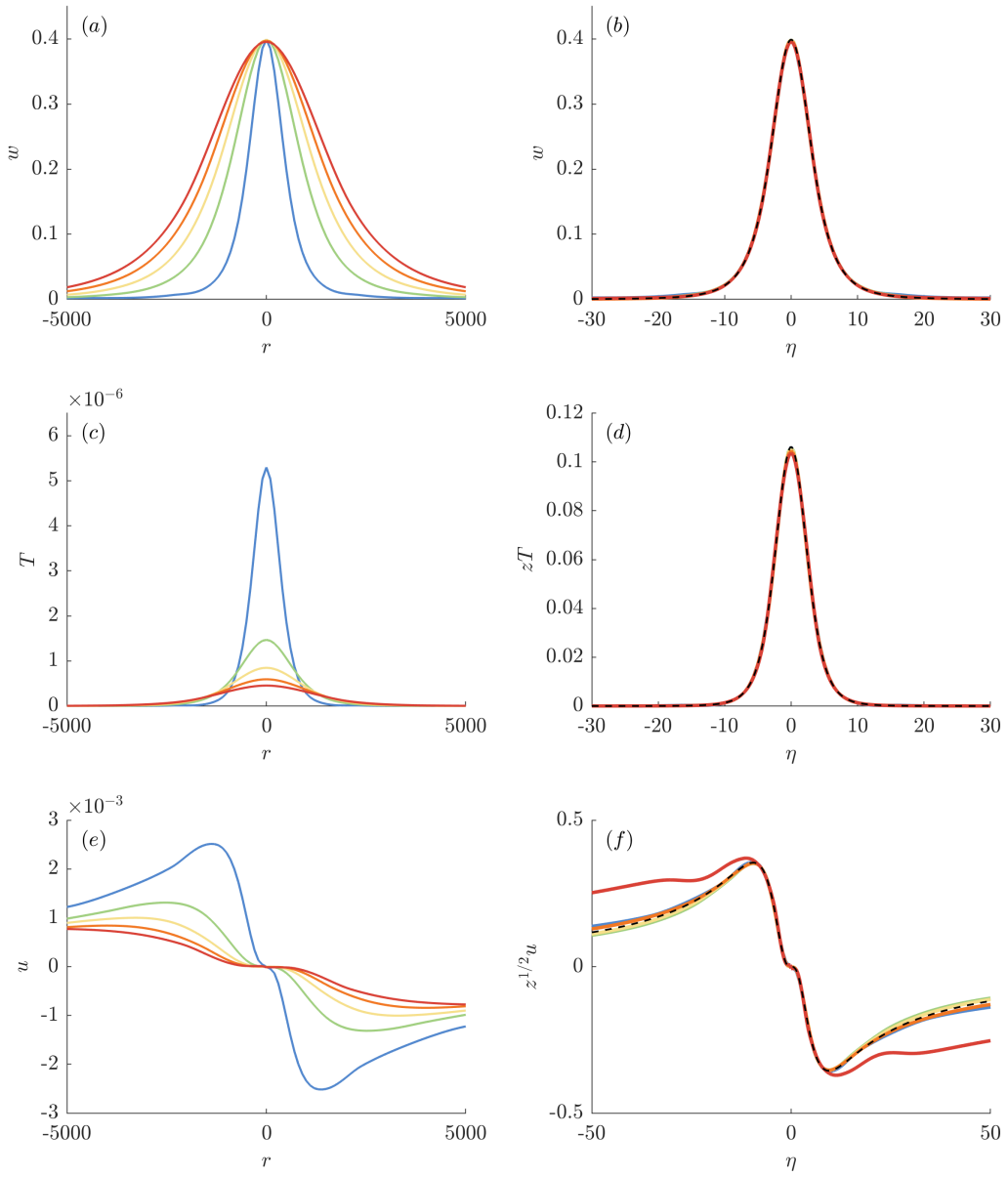

Figure 2.12: Temporally and azimuthally averaged vertical velocity (a), temperature (c), and horizontal velocity (e) from the DNS of (2.17)–(2.20) for $Pr = 1$ at five dimensionless heights from $z = 2 \times 10^4$ (blue) to 2.3×10^5 (red). The centreline vertical velocity is equal at all heights in the laminar regime, according to the scaling in (2.29). The vertical velocity (b), height-multiplied temperature (d), and square root of height multiplied by horizontal velocity (f) are scaled with respect to the similarity variable η and compared to f'/η, h, and $f/2 - f/\eta$, respectively (black, dashed), from the solution to the system (2.25)–(2.28). A collapse of the DNS onto the similarity solution for all heights for vertical velocity and temperature in the laminar regime is evident. In plot (f), it is interesting to see the horizontal velocity starting to differ from the laminar similarity solution as the plume begins to transition to turbulence.

initial ascent and final state below the height of instability z_*, a selection of cross-sections at various heights of the vertical velocity w and temperature T fields are plotted in figure 2.12. The left-hand plots show profiles of the raw values and the right-hand plots show the values mapped into the similarity variables. Figure 2.12(b) shows the collapse of w at different heights, beneath the transition height

$$z_* \approx 3.9 \times 10^5, \tag{2.47}$$

onto the similarity solution, and figure 2.12(d) does the same for zT. The independent prediction of the similarity solution determined from the solution to (2.25)–(2.28) is shown as a dashed black curve. The result shows an excellent collapse onto the laminar solution. It is evident from this that the laminar portion of the numerics agree with the similarity solution, and that the centre-line values of w and zT are constant with height in the steady, laminar regime. It is interesting to note, in figure 2.12(f), that the horizontal velocity begins to differ from the laminar similarity solution hence indicating that the plume is beginning to transition to turbulence.

To illustrate the change in centreline values from the laminar to turbulent regime at the height to instability, along with time averaged contours of velocity and logarithm of temperature, figure 2.13 plots the centreline values of vertical velocity

$$w_0 = \lim_{\eta \to \infty} f'(\eta)/\eta = 0.40, \tag{2.48}$$

and similarity temperature

$$h_0 = h(0) = 0.11, \tag{2.49}$$

next to the similarity solution, illustrating the change from laminar regime where w and zT are approximately constant with height up to $z \approx z_* = 3.9 \times 10^5$, to the transitional and turbulent regimes which will be discussed in later sections. The standard deviation for vertical velocity is defined by

$$\sigma_w = \left(\frac{1}{N} \sum_{i=1}^{N} (w_i - \overline{w})^2 \right)^{1/2}, \tag{2.50}$$

and similarly for temperature T, where w_i represents centreline vertical velocity

at a given time-step i out of N total time-steps and $\overline{w}$ represents the mean vertical velocity. The near-zero value of standard deviation in the laminar regime for both vertical velocity and temperature shows how little variability there is in vertical velocity and temperature in the laminar plume.

The source fluxes, described in (2.22)–(2.24), can also be expressed in similarity form. By substituting (2.29) into (2.23) and (2.24), it holds that Q and M are both linear in z, and F is constant, given by

$$Q = \left(2\pi \lim_{\eta\to\infty} f\right) z, \tag{2.51a}$$

$$M = \left(2\pi \int_0^\infty \frac{f'^2}{\eta}\, \mathrm{d}\eta\right) z, \tag{2.51b}$$

$$F = 1. \tag{2.51c}$$

As a further check on the agreement of the DNS with the similarity solution, the volume, momentum and buoyancy fluxes calculated using the DNS results of (2.17)–(2.20) for $Pr = 1$ (2.22)–(2.24) are compared to those calculated from the solution to the similarity equations (2.51), in figure 2.14. The fluxes from the DNS (2.22)–(2.24) are calculated by extracting two vertical planes (XZ and YZ planes, each bisecting the full height of the plume), calculating the fluxes at each height using Simpson's Rule (Atkinson, 1991) to approximate the integrals (2.22)–(2.24) for every time-step for $t > 1.6 \times 10^7$, and then subsequently averaging in time. Standard deviation for buoyancy flux at each height z is calculated using

$$\sigma_F(z) = \left(\frac{1}{N}\sum_{i=0}^{N}\left(F_i(z) - \overline{F}(z)\right)^2\right)^{1/2}, \tag{2.52}$$

where N is the number of time samples from $t \in [1.6, 2.7] \times 10^7$, $F_i(z)$ is the buoyancy flux at each time-step i and $\overline{F}(z)$ is the average buoyancy flux, both at height z. The standard deviations for volume and momentum flux, $\sigma_Q(z)$ and $\sigma_M(z)$, are calculated analogously. The standard deviation for each flux is plotted in figure 2.14 as the respective shaded area, illustrating the near-zero fluctuation in the laminar regime in each flux over time, and the beginning of the transition to turbulence at the top of each plot.

Figure 2.14 shows excellent agreement with the laminar similarity

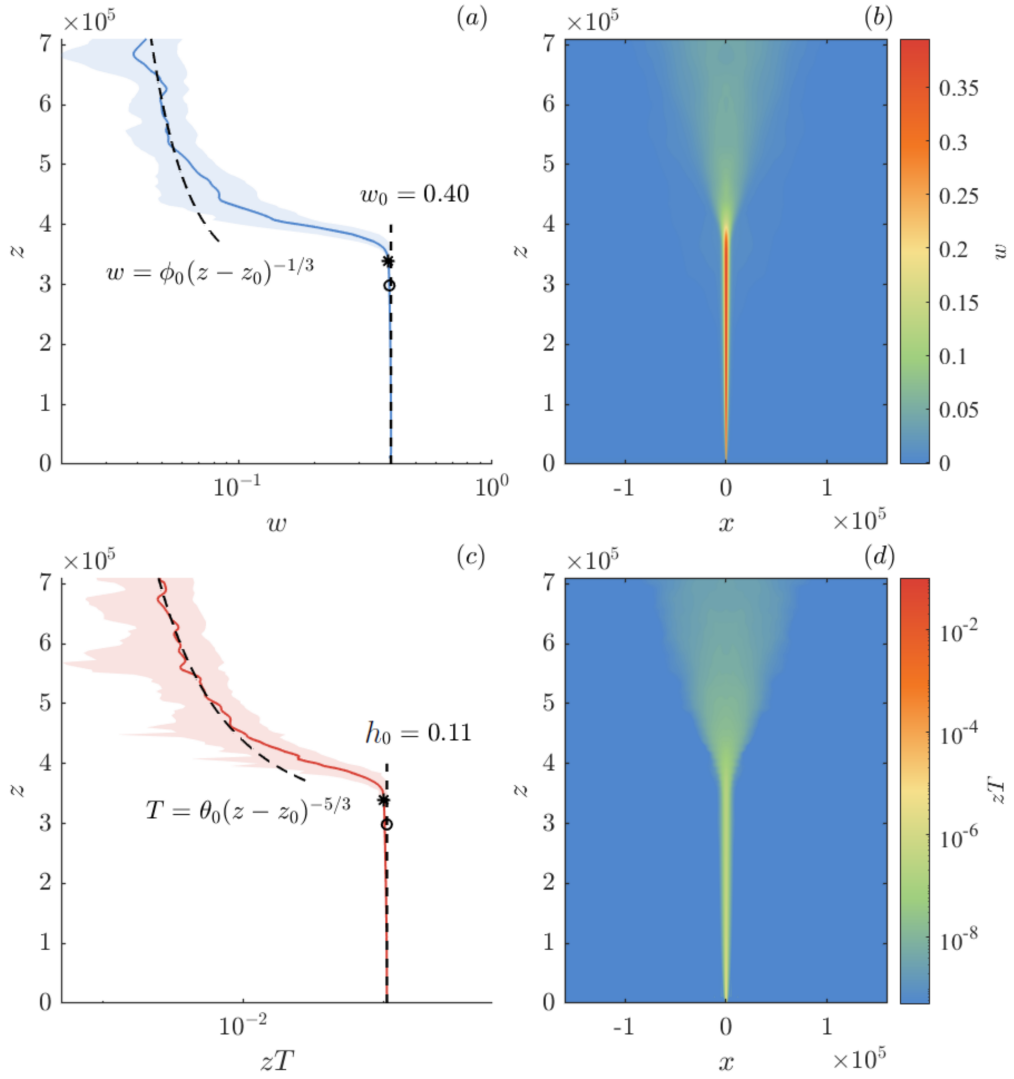

Figure 2.13: In panel (a) centreline vertical velocity is compared with both laminar (2.29) and turbulent (2.57) similarity solutions. Plot (b) shows temporally and azimuthally averaged vertical velocity from the DNS of (2.17)–(2.20). In plot (c) height-multiplied, centreline temperature is compared with both laminar (2.29) and turbulent (2.57) similarity solutions, as in plot (a). Plot (d) shows temporally and azimuthally averaged temperature from the solution to (2.17)–(2.20), as in plot (b). There is a good fit for both the laminar and turbulent similarity solutions with the DNS either side of a transition zone spanning $3.9 \times 10^5 \lesssim z \lesssim 4.8 \times 10^5$. Black asterisks indicate the height of instability $z = z_* \approx 3.9 \times 10^5$, and black circles indicate the height $z = z_0 = 2.9 \times 10^5$, representing the virtual origin for the turbulent regime and the departure from the laminar regime. The shaded region in panels (a) and (c) represent the standard deviation in the vertical velocity and temperature, respectively and illustrate the variability in the turbulent flow and lack-thereof in the laminar flow.

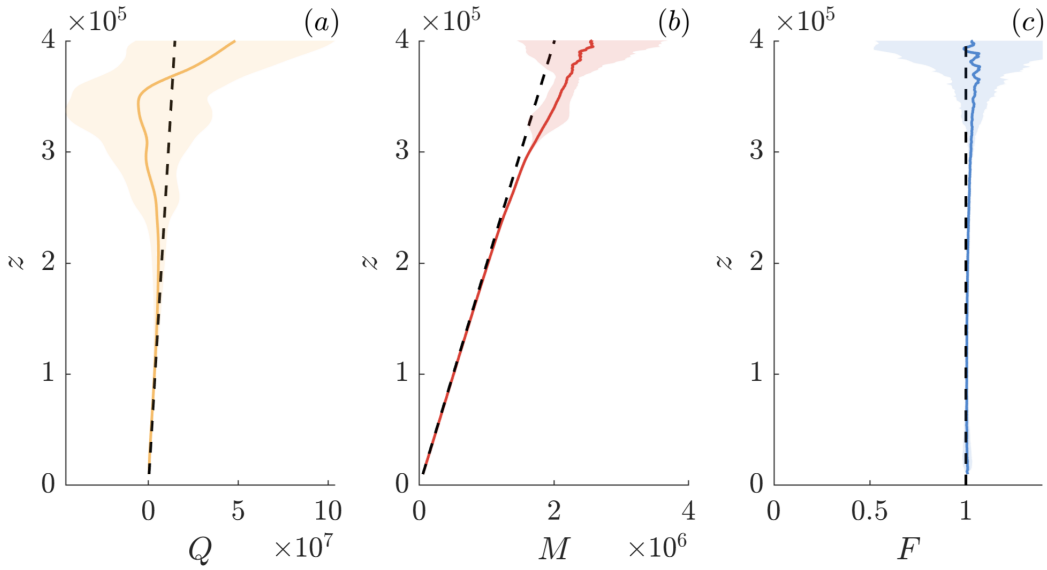

Figure 2.14: Volume Q, momentum M and buoyancy F advective fluxes (2.22)–(2.24) calculated from the DNS of (2.17)–(2.20), compared with equivalent similarity fluxes (2.51) calculated using the solution to the similarity equations (2.25)–(2.28). The DNS solution (solid curves) shows excellent agreement with the predictions of the laminar similarity solution (dashed curves), providing a further check on the DNS. Standard deviations for each flux are calculated using (2.52) and represented as the shaded areas in each plot.

solution. It is also clear where the DNS begins to diverge from the laminar similarity solution as the flow transitions to turbulence at a height of $z \approx 2.5 \times 10^5$, which, interestingly is lower than the height to instability extracted from the values of the vertical velocity at $z_* = 3.9 \times 10^5$.

2.4.1 Growth of the plume head

The initial transience of the plume results in an oval-shaped head region at the front of the developing laminar regime, as illustrated in figure 2.9. In contrast to the stem, the head exhibits a comparable size in each dimension, indicating a local breakdown of the boundary-layer approximation. The size of the head increases with time from its initiation. In figure 2.15, the horizontal radius of the plume head r_H and the plume stem r_s from the results of the DNS of (2.17)–(2.20) for $Pr = 1$, are plotted as a function of time. The radius is defined as the location where the velocity has decreased to 20% of the maximal value in the centre of the head. The plot shows that the head grows in size as $t^{2/3}$, a power-law that is faster than the growth of the radius of the plume stem

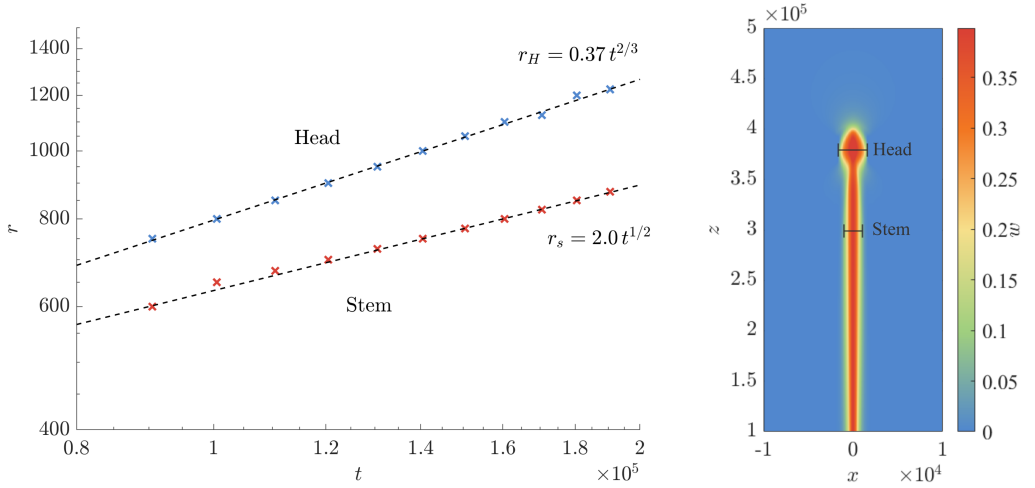

Figure 2.15: Radius of the plume head r_H and stem at the widest point below the head r_s against time, as predicted by the DNS of (2.17)–(2.20) for $Pr = 1$. Dashed curves represent predictions of the form $r_H = 0.37\,t^{2/3}$ for the head, given by (2.53), and $r_s = 2.0\,t^{1/2}$ for the stem.

at its widest point just below the head, which grows in size as $t^{1/2}$ (Batchelor, 1954). Predictions for the radius of the plume head r_H and the radius of the plume stem r_s are plotted as functions of time in figure 2.15 with the radius of the plume head predicted to grow as

$$r_H = \zeta_H t^{2/3}, \tag{2.53}$$

where ζ_H is a constant prefactor. Fitting the value $\zeta_H = 0.37 \pm 0.003$ and plotting in figure 2.15, the prediction (2.53) shows excellent agreement with the DNS. The corresponding stem radius increases as $r_s = \zeta_s\,t^{1/2}$, where $\zeta_s = 2.0 \pm 0.007$, also showing good agreement with the DNS. The error ranges are found using the 95% confidence interval in the least squares fit of r_H and r_s. It is interesting to note that the predictions of Moses et al. (1993) are different to those suggested here, as they assumed the head radius would increase at the same rate as the stem radius and hence fitted a $t^{1/2}$ power law to the expansion of the head radius.

The work in this section describes the evolution of the time-dependent front of a plume, equivalent to addressing research question 4. The radius of the plume head has been shown to expand with time as $t^{2/3}$, differing from the prediction of the expansion of the stem radius of $t^{1/2}$ (Batchelor, 1954; Moses et al., 1993).

2.5 Instability and transition to turbulence

Figures 2.9 and 2.10 illustrate two types of instability, firstly, the head instability whereby the spherical region on top of the laminar plume becomes unstable at a height of $z \approx 1.2 \times 10^5$ and a time of $t \approx 7.0 \times 10^5$. Secondly, the instability where the laminar region goes unstable and transitions to a turbulent plume at a height of $z = z_* \approx 3.9 \times 10^5$, henceforth referred to as the 'steady' instability. As the location of the head instability rises with time $z = z_*(t)$ and eventually settles at the steady height to instability, the flow develops into a turbulent plume for $z > z_*(t)$. As can be seen in figure 2.10(d), the plume begins to widen laterally from an effective point source localised at some z_0. In this regime, the boundary-layer assumption $\partial/\partial r \gg \partial/\partial z$ made in section 2.4 can no longer be applied due to the development of turbulent eddies with an order-unity aspect ratio, in effect radius scales like height $r \sim z$. It is proposed, however, that the leading-order dynamics of the flow no longer depend explicitly on the viscosity nor the thermal diffusivity of the fluid, in accordance with previous models of turbulent plumes (e.g. Zeldovich, 1937; Morton et al., 1956) and vigorous (high Rayleigh number) convection (Bejan, 2013). The viscous stresses and diffusive transport associated with these parameters still play a role in generating and sustaining turbulence, but the size of the coefficients themselves no longer have an impact on the flow.

A scaling analysis of the full equations (2.17)–(2.20), results in the following scaling relationships

$$r \sim z, \qquad \frac{Dw}{Dt} \sim T, \qquad 2\pi \int_0^\infty rTw \, \mathrm{d}r \sim 1. \tag{2.54}$$

The second and third scalings are similar to those in the laminar regime (1.21), the difference being that the scaling between inertia and viscosity has been replaced with the scaling $r \sim z$, that horizontal and vertical lengths scale together. Using these scalings the three scaling relationships

$$r \sim z, \qquad w^2 \sim zT, \qquad r^2 Tw \sim 1, \tag{2.55}$$

are obtained. Resolving these scales illustrates that it is impossible to form a length scale in the problem that does not depend on the independent variable z, indicating the existence of a similarity solution (Zeldovich, 1937). By

rearranging the relationships (2.55) for w and T results in the scalings

$$w \sim z^{-1/3}, \qquad T \sim z^{-5/3}. \tag{2.56}$$

In the following, the fact that the origin of instability and the effective origin of the similarity solution conforming to these scalings are offset from the source origin is taken into account. Hence, it is specified that the turbulent regime initiates from an effective virtual origin at a height z_0, to be determined by comparing the self-similar predictions with the results of the DNS of (2.17)–(2.20). It is interesting to note that z_0 does not coincide with the position of instability z_*, which is consistent with a spatially extended transition zone between z_* and the fully developed turbulent regime evident in figure 2.13. Allowing for the displacement in origin of the turbulent regime, the relevant similarity variables describing the statistically averaged final state of the turbulent regime take the form

$$w = (z - z_0)^{-1/3}\phi(\xi), \qquad T = (z - z_0)^{-5/3}\vartheta(\xi), \tag{2.57}$$

where $\xi = r/(z - z_0)$ is the similarity variable, and $\phi(\xi)$ and $\vartheta(\xi)$ are structure functions. In light of these scalings, the turbulent regime is predicted to maintain a consistent angle of expansion, forming a cone from a virtual origin z_0. The conic shape is evidenced clearly in the temporally and azimuthally averaged contour plots in figure 2.13. The centreline velocity decays with height as $w \sim (z - z_0)^{-1/3}$, instead of remaining constant with height in the laminar regime, and the temperature decreases as $(z - z_0)^{-5/3}$, which is faster than the laminar decay of z^{-1}, attributable to the vigorous mixing of the turbulent plume. Using the scaling relationships in (2.55) a local Reynolds number of the flow is shown to scale like

$$Re_T(z) = \frac{wr}{Pr} \sim (z - z_0)^{2/3}. \tag{2.58}$$

Thus, despite the decrease in the flow rate $w \sim (z - z_0)^{-1/3}$, the larger length scale caused by the relatively faster lateral expansion of the plume, $r \sim z$, allows the local Reynolds number Re_T to continue to increase in the turbulent regime, consistent with maintaining a turbulent regime at ever greater heights.

Prior experimental and numerical studies focusing on turbulent plumes have obtained predictions for the velocity and temperature structure functions

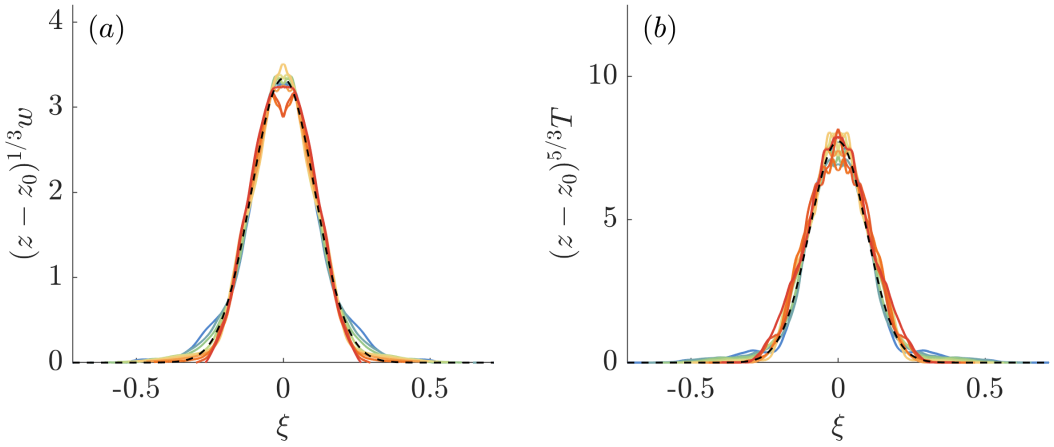

Figure 2.16: Collapse of the temporally and azimuthally averaged (a) vertical velocity and (b) temperature profiles determined from the DNS for $Pr = 1$ in the turbulent region of the plume, sampled from five equally spaced heights across the region $z \in [5.6, 7.1] \times 10^5$, forming the turbulent analogue of figure 2.12. The time window over which the solution is averaged for is $t \in [1.6, 2.1] \times 10^7$. The profiles are plotted in terms of the similarity forms of the vertical velocity and temperature, defined by $(z-z_0)^{1/3}w$ and $(z-z_0)^{5/3}T$, respectively. Consistent collapses of the data to the Gaussians (2.59) are observed for $z_0 = (2.9 \pm 0.23) \times 10^5$, with prefactors $\phi_0 = 3.3 \pm 0.1$ and $\vartheta_0 = 7.7 \pm 1.3$ and spread coefficients of $\alpha_w = 43.2 \pm 7.2$ and $\alpha_T = 54.2 \pm 8.3$ (dashed black curves).

$\phi(\xi)$ and $\vartheta(\xi)$. These papers all conclude that the transverse profiles for the time-averaged statistically steady state of a developed turbulent plume both closely follow Gaussian profiles,

$$\phi(\xi) = \phi_0 e^{-\alpha_w \xi^2}, \qquad \vartheta(\xi) = \vartheta_0 e^{-\alpha_T \xi^2}, \tag{2.59}$$

where ϕ_0 and ϑ_0 are constants representing the centreline vertical velocity and temperature, respectively, and α_w and α_T are constants representing the profile widths. These studies reported values of α_w ranging from 55 to 96, and α_T from 60 to 80 (Rouse et al., 1952; George Jr et al., 1977; Zimin & Frik, 1977; Devenish et al., 2010). Different studies report conflicting conclusions, some predicting that the vertical velocity profile is wider then the temperature profile ($\alpha_w < \alpha_T$), while others conclude that it is narrower ($\alpha_w > \alpha_T$).

In figure 2.16 the collapse of the DNS solutions of (2.17)–(2.20) onto a consistent self-similar solution (as in figure 2.12 for the laminar solution) is plotted. It illustrates the temporally (for $t \in [1.6, 2.1] \times 10^7$) and azimuthally averaged solution to (2.17)–(2.20) at five equally spaced heights across the

region $z \in [5.6, 7.1] \times 10^5$, rescaled in terms of the similarity coordinate ξ. These curves clearly resemble Gaussian profiles, as discussed above. In order to determine the values of ϕ_0, ϑ_0, α_w, α_T, and z_0 from the solution to the DNS of (2.17)–(2.20), a non-linear regression using a genetic algorithm (Mitchell, 1996) is performed. This consists of assuming the form of the solution to be (2.57) and (2.59) and using the least-squares approach to minimise the sum

$$\sum_{i=1}^{n} \left[\frac{1}{w_N} \left(\overline{w}_i - (z_i - z_0)^{-1/3} \phi(\xi) \right)^2 + \frac{1}{T_N} \left(\overline{T}_i - (z_i - z_0)^{-5/3} \vartheta(\xi) \right)^2 \right] \tag{2.60}$$

for $i = 1, \ldots, n$ data points for time (over the range $t \in [1.6, 2.7] \times 10^7$) and azimuthally averaged vertical velocity $\overline{w}_i = \overline{w}(r_i, z_i)$ and temperature $\overline{T}_i = \overline{T}(r_i, z_i)$ for $z_i \in [5.6, 7.1] \times 10^5$ from the DNS, with respect to the parameters ϕ_0, ϑ_0, α_w, α_T, and z_0.

A genetic algorithm is the method used to minimise the sum (2.60), it consists of setting a population size and then iterating through a predetermined number of generations to statistically approach the minimum values for each of the five parameters. Minimising a sum for five parameters is a difficult task as there can be many local minima that attract the minimisation function. A genetic algorithm is a good choice for this problem as it is randomly initialised, meaning that running the genetic algorithm many times is likely to find the true minimum value. In this problem, a population size of 200 is run through 100 generations, 25 different times, until a minimum value of 1.83×10^{-4} is found. Errors are found by finding the standard deviation in each parameter ϕ_0, ϑ_0, α_w, α_T, and z_0 over the number of minimisations conducted.

Performing the minimisation of (2.60) results in fitting Gaussians of the form (2.59) with values of $\phi_0 = 3.3 \pm 0.1$, $\vartheta_0 = 7.7 \pm 1.3$, $\alpha_w = 43.2 \pm 7.2$, $\alpha_T = 54.2 \pm 8.3$, and $z_0 = (2.9 \pm 0.23) \times 10^5$. As discussed, previous studies have found values of the Gaussian profile width constants of α_w ranging from 55 to 96, and α_T from 60 to 80 (Rouse et al., 1952; George Jr et al., 1977; Zimin & Frik, 1977; Devenish et al., 2010). Interestingly, using the genetic algorithm of (2.60) from the DNS of (2.17)–(2.20) slightly underpredicts the values of α_w and α_T compared to those in the literature. This could be because our measurements are taken too close to the initialisation of the turbulent regime, as suggested by Papanicolaou & List (1988). Further simulations in a larger domain, currently underway, will inform whether this is true. The results also

show, however, that for a turbulent plume in an unstratified environment it can be appropriate to assume an approximately point-like source of buoyancy feeding a turbulent regime at a height of z_0.

Comparison of the centreline similarity predictions for velocity and temperature in (2.57) at $\xi = 0$ with the DNS in figure 2.13 show good agreement for the turbulent regime, with standard deviation (2.50) in lighter shading illustrating the variability in the turbulent flow (and lack-thereof in the laminar flow). The change from laminar regime (discussed earlier) to a transition zone covering an approximate region $[3.9,\ 5.0] \times 10^5$ is illustrated, as well as a turbulent region for $z \gtrsim 5.0 \times 10^5$ where $w \sim (z - z_0)^{-1/3}$ and $T \sim (z - z_0)^{-5/3}$.

The fluxes of volume Q, momentum M, and buoyancy F are calculated from the solution to the DNS (2.17)–(2.20) by extracting two vertical planes (XZ and YZ planes, each bisecting the full height of the plume), calculating the fluxes at each height using Simpson's Rule (Atkinson, 1991) to approximate the integrals (2.22)–(2.24) for every time-step, and then subsequently averaging in time. The fluxes from the DNS are plotted in figure 2.17 as solid curves. Standard deviation for volume, momentum, and buoyancy flux is calculated as in (2.52) for the range $t \in [1.6, 2.7] \times 10^7$ and is plotted in figure 2.17 as the respective shaded area, illustrating the high levels of variability in the turbulent regime in each flux over time.

The theoretical volume, momentum, and buoyancy fluxes described in (2.22)–(2.24), can be expressed in turbulent similarity form. By substituting (2.57) into (2.24), F remains constant, and Q and M are of the form

$$Q = c(z - z_0)^{5/3}, \tag{2.61a}$$

$$M = d(z - z_0)^{4/3}, \tag{2.61b}$$

$$F = 1, \tag{2.61c}$$

where c and d are constants. The turbulent similarity volume, momentum and buoyancy fluxes are fitted to the fluxes from the DNS using MATLAB and the coefficients are found to be $c = 0.22$ and $d = 0.45$ (where $z_0 = 2.9 \times 10^5$). They are compared to those from the DNS (2.22)–(2.24), calculated from the solution to the DNS of (2.17)–(2.20), in figure 2.17. The DNS shows excellent agreement with the volume, momentum, and buoyancy in the laminar (2.51) regime and good agreement in the turbulent (2.61) regime where the curves

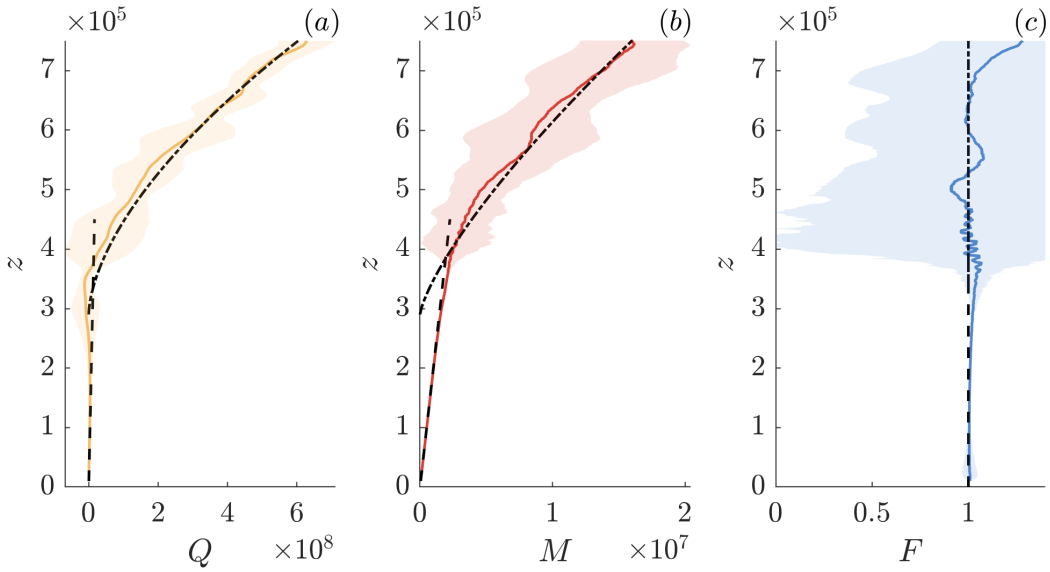

Figure 2.17: Volume Q (a), momentum M (b), and buoyancy F (c) advective fluxes (2.22)–(2.24) calculated from the DNS of (2.17)–(2.20), compared with equivalent similarity fluxes (2.61) calculated using the solution to the laminar similarity equations (2.25)–(2.28). The DNS solution (solid curves) shows good agreement with the predictions of the turbulent similarity solution (dot-dashed curves). The laminar similarity solutions from figure 2.14 is plotted as well for comparison. Standard deviations for each flux are calculated using (2.52) and represented as the shaded areas in each plot.

from the DNS vary slightly from the similarity predictions but are well captured by the standard deviation (shaded areas).

The work in this chapter results in a full unified theory of a laminar to transitional to turbulent plume, equivalent to addressing research question 2. By describing the transition from point source of heat to laminar plume in section 2.3.3, introducing the height to instability z_* in section 2.3.5, and quantifying the turbulent virtual origin z_0 in this section, a steady plume in an unstratified environment can be fully described using the laminar (Zeldovich, 1937; Yih, 1951) and turbulent (Zeldovich, 1937; Schmidt, 1941) similarity solutions, the height to instability z_*, and the turbulent virtual origin z_0.

2.6 Summary of final structure

As a full summary, an overview of the structural components of the hybrid plume in terms of dimensional variables is provided here. From the develop-

ment of a heat source to a laminar plume, discussed in section 2.3.3, to the laminar regime in which the similarity solution (Zeldovich, 1937; Yih, 1951) described the flow, discussed in section 2.4, through the transition zone in the region around $z \approx z^*$, and finally to the turbulent regime, whereby the flow is described by the turbulent similarity solution (Zeldovich, 1937; Schmidt, 1941) in section 2.5. Reinstating dimensions using (2.16), with hats to denote dimensionless variables, the full structure is as follows.

Regime type (and reference in text)	Equations (if any)	Height over which regime occurs
Heat source (2.20):	$$w \approx 0,$$ $$\frac{\partial T}{\partial z} = \lim_{r_s \to 0} \left(\frac{1}{\pi r_s^2} \right).$$	$0 \leq \frac{z}{L} < \hat{z}_H$
Laminar (self-similar) (2.25)–(2.28):	$$w = \left(\frac{F_0}{\kappa} \right)^{1/2} \hat{w} \left(\left(\frac{F_0}{\kappa^3} \right)^{1/4} r z^{-1/2} \right),$$ $$T = \frac{1}{g\beta} \left(\frac{F_0}{\kappa} \right) z^{-1} \hat{h} \left(\left(\frac{F_0}{\kappa^3} \right)^{1/4} r z^{-1/2} \right).$$	$\hat{z_H} \leq \frac{z}{L} < \hat{z}_0$
Transitional		$\hat{z}_0 \leq \frac{z}{L} \lesssim \hat{z}_* + 10^4$

Turbulent (self-similar) (2.57): $\hat{z}_* + 10^4 \lesssim \frac{z}{L}$

$$w = F_0^{1/3} \frac{\phi_0}{(z - z_0)^{1/3}} \exp\left(-\alpha_w \left(\frac{r}{z - z_0}\right)^2\right),$$
$$T = \frac{1}{g\beta} F_0^{2/3} \frac{\vartheta_0}{(z - z_0)^{5/3}} \exp\left(-\alpha_T \left(\frac{r}{z - z_0}\right)^2\right).$$

The length scale $L = (\kappa^3/F_0)^{1/2}$ was defined in the scaling analysis in (2.15). For $Pr = 1$, $\hat{z}_H \approx 100$ is the height above which the laminar similarity solution applies with negligible loss of information, $z_0 = (2.9 \pm 0.23) \times 10^5$ is the dimensionless virtual origin for the turbulent regime, $\hat{z}_* = 3.9 \times 10^5$ is the dimensionless height of instability, $\hat{w}$ and $\hat{h}$ are solutions to the laminar similarity equations (2.25)–(2.28), and the constants for the turbulent regime are given by $\phi_0 = 3.3 \pm 0.1$, $\vartheta_0 = 7.7 \pm 1.3$, $\alpha_w = 43.2 \pm 7.2$, and $\alpha_T = 54.2 \pm 8.3$.

2.7 Conclusions

In this chapter, I have produced the first theoretical description of the full structure of a plume in an unstratified environment undergoing transition from laminar to turbulent self-similar regimes. A description of dimensionless height to instability $\hat{z}_*$ was found for $Pr = 1$, addressing research question 1. Using the length-scale $L = (\kappa^3/F_0)^{1/2}$, defined in the scaling analysis in (2.15), the dimensionless height to instability $\hat{z}_* \approx 5.1 \times 10^5$ (2.47) is re-dimensionalised to find that the dimensional height to instability for a plume rising from a point source of heat in an unstratified environment for $Pr = 1$ is

$$z_* = \hat{z}_* \left(\frac{\kappa^3}{F_0}\right)^{1/2}, \tag{2.62}$$

in a domain with radius $r_e = 1.6\,(\kappa^3/F_0)^{1/2} \times 10^5$ and height $z_e = 8.0\,(\kappa^3/F_0)^{1/2} \times 10^5$. For a given fluid, with thermal diffusivity κ (and equal viscosity ν as $Pr = 1$), the height to instability can be predicted using z_* for any initial buoyancy flux F_0.

The summary in section 2.6 describes the full structure of a plume emanating from a point source in an unstratified environment for $Pr = 1$, addressing research question 2. This was achieved by describing the transition from a point source of heat to a laminar plume in section 2.3.3, illustrating the laminar similarity solution (2.25)–(2.28) (Zeldovich, 1937; Yih, 1951), subsequently introducing the height to instability $\hat{z}_*$ in section 2.3.5, quantifying the turbulent virtual origin $\hat{z}_0 \approx 2.9 \times 10^5$ in section 2.5 along with the turbulent similarity solution (2.57) (Zeldovich, 1937; Schmidt, 1941), and finally re-introducing the dimensional variables from section 2.2. The height to instability $\hat{z}_*$ was shown to differ from the effective virtual origin for the turbulent regime $\hat{z}_0$. This is an interesting result, suggesting that the transition to turbulence exists over a large spatial region and that there is some lazy-like plume behaviour in the transition region with the actual origin turbulent plume higher than the effective virtual origin.

The evolution of a point source of heat into a laminar plume was described in section 2.3.3. This addressed research question 3 by finding that flow from a point source of heat, for $Pr = 1$, can be approximated by the solution to the laminar similarity solution (2.25)–(2.28) after only approximately 100 dimensionless spatial units.

Comparing the head instability to the stem instability in section 2.4.1, it was shown that the radius of the head region evolves with time as $t^{2/3}$. As the radius of the stem evolves at $t^{1/2}$ (Batchelor, 1954), the head must go unstable before the stem, resulting in a turbulent head followed by a laminar stem flow, hence addressing research question 4.

In an attempt to short-cut to a quasi-steady state, a simulation of a plume initialised with the laminar similarity solution (2.25)–(2.28) through the full height of the simulation domain was performed. A drop in height to instability to far less than the predicted steady value was found, therefore implying the time-dependent height to instability is dependent on the accumulation of fluid in the head region that occurs at the front of the growing laminar plume regime.

The work in this chapter forms a basis for all of my subsequent work which will be to generalise the description of the full structure of a plume for independently varying viscosity and thermal diffusivity in chapter 3, to investigate the evolution and structure of plumes in a stratification in chapter 4,

and to apply the prediction of height to instability to aerosol transport in chapter 5.

2.7.1 Limitations and further work

The value of height to instability $\hat{z}_*$ found using DNS of (2.17)–(2.20) in this chapter was found to be insensitive to a changing mesh. The work on the turbulent regime, however, was not possible on this mesh due to the height to instability being too near to the top of the domain. Further work could apply all the methods and practices developed in this chapter to further simulations in a larger domain to result in a robust, full description of a plume in an unstratified environment.

Chapter 3

The effect of Prandtl number on plumes in an unstratified environment

Contents

The non-dimensional system (2.17)–(2.20) discussed in chapter 2, describing the full evolution of a plume emanating from a point source in an unstratified environment, was shown to depend on just one dimensionless number, the Prandtl number. Pure plumes in unstratified environments can therefore be classified entirely in the terms of the Prandtl number alone. That is, the development, evolution and structure of a plume in an unstratified environment for a given ratio of the viscosity ν to thermal diffusivity κ is universal up to a scaling. Across both natural and industrial contexts, Prandtl numbers can vary by orders of magnitude. For example, $Pr \sim 10^{-6}$ for stellar and planetary

dynamics, $Pr \sim 10^{-3}$ for molten metals, $Pr \sim 1$ for air, $Pr \sim 10$ for water, and $Pr \gtrsim 10^{20}$ for the Earth's mantle, with plumes a common occurrence in each application. In this chapter, the structure and asymptotic elements of pure plumes generated at a point source of heat and the dependence of the resulting structure on the viscosity and diffusivity of the fluid is investigated and analysed using a combination of direct numerical simulations (DNS) and scaling analyses.

Initially, a recap of the governing equations and non-dimensionalisation from chapter 2 is given in section 3.1. Following this is a description of the DNS used to model the plumes in section 3.2. A recap of the laminar theory from chapter 2 and an investigation into the asymptotic behaviours of the laminar regime of plumes generated from a point source of heat in an unstratified environment is considered in section 3.3, addressing research question 6. In section 3.4 the height to instability for each Prandtl number is investigated and extracted from the results of the DNS, along with a discussion of the turbulent regime, addressing research question 5. Finally, conclusions are drawn in section 3.5.

3.1 Modelling a plume for a range of Prandtl numbers

As in chapter 2, a plume emanating from a point source of heat at $\boldsymbol{x} = (0, 0, 0)$ is modelled in an unstratified environment. A plume of this form is dependent only on a single parameter, namely the Prandtl number. As a result, any pure plume, after a scaling by the length, time, and temperature scales

$$L = \left(\frac{\kappa^3}{F_0}\right)^{1/2}, \qquad \tau = \frac{\kappa^2}{F_0}, \qquad \mathcal{T} = \frac{1}{\beta g}\left(\frac{F_0^3}{\kappa^5}\right)^{1/2}, \tag{3.1}$$

can be modelled by the governing equations, first given in (1.1)–(1.4). They are non-dimensionalised, as in section 2.2, to result in the dimensionless

$$\frac{D\boldsymbol{u}}{Dt} = -\boldsymbol{\nabla} p + Pr\nabla^2\boldsymbol{u} + T\hat{\boldsymbol{z}}, \tag{3.2a}$$

$$\boldsymbol{\nabla}\cdot\boldsymbol{u} = 0, \tag{3.2b}$$

$$\frac{DT}{Dt} = \nabla^2 T, \tag{3.2c}$$

where $\boldsymbol{x} = (x, y, z)$ is the spatial coordinate vector, t is time, $\boldsymbol{u}(\boldsymbol{x}, t) = (u, v, w)$ is the fluid velocity, p is the fluid pressure, $T(\boldsymbol{x}, t)$ is the temperature, and the single controlling parameter, defined by $Pr = \nu/\kappa$, is the Prandtl number. The no-slip and far-field conditions are as before

$$\boldsymbol{u}(x, y, 0, t) = \boldsymbol{0}, \qquad \frac{\partial T}{\partial n}(x, y, 0, t) = 0, \tag{3.3}$$

and

$$\lim_{R\to\infty} \boldsymbol{u} = 0, \qquad \lim_{R\to\infty} T = 0, \tag{3.4}$$

respectively. The source condition is

$$\lim_{\varepsilon\to 0} \int_{S_\varepsilon} \left(-\frac{\partial T}{\partial n}\right) \, \mathrm{d}S = 1. \tag{3.5}$$

The system (3.2)–(3.5) describes the initialisation and development of a plume in an unstratified environment for any Prandtl number Pr. In this chapter, predictions for the critical heights of instability ranging from $Pr = 0.1$ to 2 are investigated using DNS and scaling arguments.

The dimensionless system (3.2)–(3.5) depends on only one dimensionless number, the Prandtl number Pr. As discussed in chapter 2, pure plumes in unstratified environments can therefore be classified entirely in the terms of the Pr alone. This means that by conducting a study of plumes for a wide range of Pr, a complete description of a plume for any ratio of kinematic viscosity ν and thermal diffusivity κ can be established. This can have implications for heat generated flows in air, water, molten metals, the Earth's mantle, and other applications. A number of plumes described by the governing equations (3.2)–(3.5) are modelled at various Pr by generalising the use of DNS introduced in chapter 2.

3.2 Direct numerical simulation of plumes at various Prandtl numbers

As in chapter 2, the system (3.2)–(3.5) is solved using direct numerical simulations (DNS) using the open source, spectral element method (SEM) code Nek5000 (Fischer et al., 2008). Rather than modelling the diffusive source explicitly, the source conditions are again replaced by third-order piecewise continuous polynomials (splines, see section 2.3.4 for a description) representing the solution to the laminar similarity equations (2.25)–(2.28). Since the solution to the similarity equations is dependent on Prandtl number, the form of each spline, and hence the source specification, is different for each Pr.

In this section the details of modelling a plume at a variety of Prandtl numbers are discussed. Firstly, as in chapter 2, a description of the domain and boundary conditions is included in section 3.2.1, followed by the source conditions in section 3.2.2. Finally, an overview of the plume evolution for the Prandtl numbers studied is presented in section 3.2.3, describing the results of the DNS. An illustration of the process required to run a direct numerical simulation of a plume in Nek5000 is presented in appendix A.

3.2.1 Simulation set-up

The respective computational domains for each simulation are similar to that described in section 2.3.1. They are specified as cylinders with a variety of domain radii and heights, a description of each simulation included in table 3.1. As per the SEM, each domain is spatially discretised into N_{el} elements with polynomial order p, resulting in $N_p = p^3 N_{el}$ computational grid points.

The zero Neumann boundary conditions (2.34) are applied at the edges of the domain and turbulent eddies are suppressed from moving through these edges by applying a numerical sponge layer given by (2.35). The boundary conditions and sponge layer are illustrated in figure 2.3.

Pr	Re_*	Pe_*	$r_e\,(\times 10^4)$	$z_e\,(\times 10^5)$	N_{el}	p	$N_p\ (\times 10^6)$
0.1	1000	100	3.0	3.5	20,400	7	7.0
0.5	200	100	3.0	5.0	20,400	7	7.0
1.0	100	100	16.0	8.0	82,044	5	10.3
2.0	50	100	6.0	8.0	82,044	5	10.3

Table 3.1: Details of parameters used for direct numerical simulations of (3.2)–(3.5) for each Prandtl number given in column one. The simulation Reynolds Re_* and Péclet Pe_* numbers are used to specify the Prandtl number in the equations solved by Nek5000 (1.54). Domain parameters are domain radius r_e and domain height z_e. Mesh parameters are number of elements N_{el}, order of the basis polynomials for the spectral element method p, and number of degrees of freedom $N_p = N_{el} \cdot p^3$.

3.2.2 Source conditions at the displaced origin

As in section 2.3.4, the source is initialised in the laminar regime omitting the point source to laminar transition, justified in section 2.3.3, and using fitted splines gives good agreement with the similarity solution (2.25)–(2.28). The splines are a set of k third-order piecewise continuous polynomials mapping values from an interval to the set of real numbers, namely $S_{(w)}, S_{(z^{1/2}u)}, S_{(zT)} : [0, \eta_{\max}] \to \mathbb{R}$, they are defined by

$$S_{(w)}(\eta) = \begin{cases} P_1(\eta) = a_1\eta^3 + b_1\eta^2 + c_1\eta + d_1, & 0 \le \eta < \eta_2, \\ P_i(\eta) = a_i\eta^3 + b_i\eta^2 + c_i\eta + d_i, & \eta_i \le \eta < \eta_{i+1} \text{ for } i = 2, ..., k-1, \\ P_k(\eta) = a_k\eta^3 + b_k\eta^2 + c_k\eta + d_k, & \eta_k \le \eta < \eta_{\max}, \end{cases} \tag{3.6}$$

and similarly for $S_{(z^{1/2}u)}$ and $S_{(zT)}$. The coefficients a_i, b_i, c_i, d_i are determined using MATLAB's splinefit function to fit k polynomials to the similarity solutions for w, u, and T. Writing $\eta = rz_s^{-1/2}$ and using (2.29) allows w, u, and T to be written in terms of the splines at the displaced origin

$$w_s(r) = S_{(w)}(rz_s^{-1/2}), \tag{3.7a}$$
$$u_s(r) = z_s^{-1/2} S_{(z^{1/2}u)}(rz_s^{-1/2}), \tag{3.7b}$$
$$T_s(r) = z_s^{-1} S_{(zT)}(rz_s^{-1/2}). \tag{3.7c}$$

As in chapter 2, the height of the displaced origin for simulations in this chapter is chosen to be $z_s = 10^4$, which is shown to be larger than the diffusive region .

3.2.3 Illustration of plume behaviour for varying Prandtl number

As an illustrative overview of the evolution of plumes over a variety of Prandtl numbers, the numerical solution to the system (3.2)–(3.5) is considered for the cases $Pr = 0.1$, 0.5, 1.0, and 2.0. As in chapter 2, the transition from heat source to laminar plume, laminar plume to transition, and turbulent plume are all present for each of the plumes, but changing Pr results in changing the height at which these key features occur. Figure 3.1 illustrates the near-final state for each of the Prandtl numbers, an image is selected from each simulation either after the height to instability has stopped rising or the furthest time extent reached. As the Prandtl number increases, so does the length of the laminar regime and hence the height to instability z_*, and the vertical velocity of the plume decreases. For lower Pr, the turbulent regime appears to have a much finer structure and the laminar regime is thinner. For $Pr = 2.0$, the full height of the simulation domain is presented with the height to instability occurring close to the top of the domain. As a result, this simulation may not be reliable as the flow may be impacted by the sponge layer and the edge of the domain. It is included, however, for demonstrative purposes and to illustrate where the work could be improved.

The turbulent regime is theoretically infinite in height for every Pr. However, due to time limitations of the project and the computational cost involved in performing DNS, the simulation for the $Pr = 2$ case could not be run out to the full limits of the domain. The turbulent regime and virtual origin z_0 is therefore not a region of focus in this chapter, however, the approximate behaviour for the height to instability z_* for each of the Prandtl numbers considered is presented and should be updated on publication of these results.

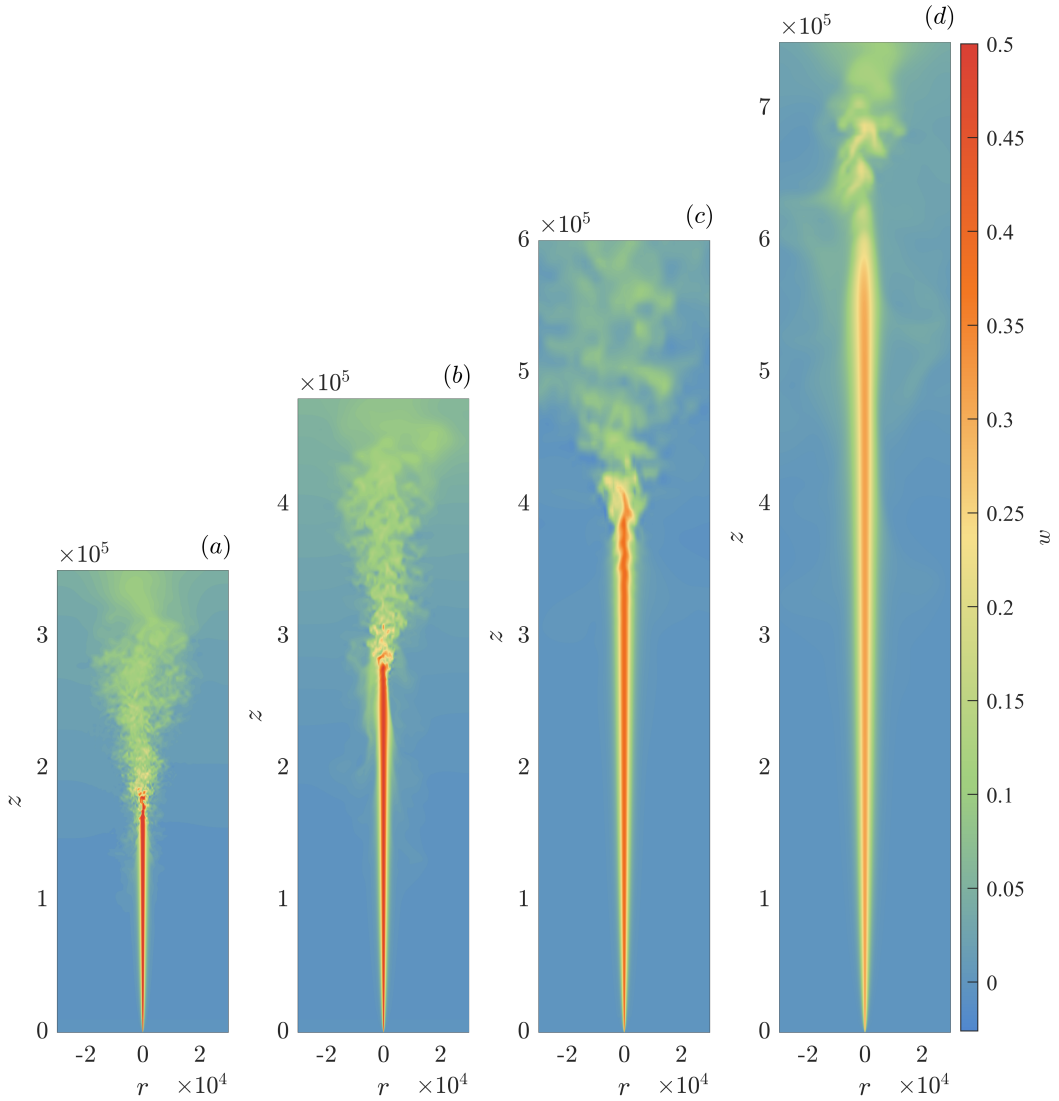

Figure 3.1: Snapshots of a number of different plumes, as predicted by the numerical solution of (3.2)–(3.5) for (a) $Pr = 0.1$, (b) $Pr = 0.5$, (c) $Pr = 1.0$, and (d) $Pr = 2.0$. The time at which each snapshot is taken is either after the height to instability has stopped rising or the furthest time extent reached, namely (a) 1.50×10^7, (b) 1.47×10^7, (c) 2.80×10^7, and (d) 1.63×10^7. The plots show the vertical velocity field w in the (x, z) cross-section for each Prandtl number, the similarity solution (3.9)–(3.12) for the vertical region $z < 10^4$ has been added to each plot to include the solution to the equations from the point source. The height to instability clearly increases as Pr increases. The width of the laminar regime grows wider with Pr and the size of the turbulent eddies decreases. While the height of the domain in each simulation differs, each plot is cut off at a radius of 3×10^4 to keep lengths and the aspect ratio constant between each plot to allow for visual comparisons.

3.3 Laminar regime

As shown in chapter 2 and by the DNS of (3.2)–(3.5) in section 3.2.3, a plume emanating from a point source in an unstratified environment exhibits behaviour that can be described by the laminar similarity equations (1.30)–(1.33). By considering the steady, axisymmetric plume equations, using boundary layer assumptions ($\partial/\partial r \gg \partial/\partial z$) and scaling to find similarity variables to simplify the dimensionless system (3.2)–(3.5), as in sections 1.1.1 and 2.4, results in the same similarity coordinate $\eta = rz^{-1/2}$ and variables $f(\eta)$ and $h(\eta)$, such that the vertical velocity w, temperature T, and radial velocity u are given by

$$w = \frac{1}{\eta} f'(\eta), \qquad T = z^{-1} h(\eta) \qquad u = z^{-1/2}\left(\frac{1}{2} f'(\eta) - \frac{1}{\eta} f(\eta)\right), \tag{3.8}$$

satisfying the equations

$$-f\left(\frac{f'}{\eta}\right)' = Pr\left(\eta\left(\frac{f'}{\eta}\right)'\right)' + \eta h, \tag{3.9a}$$

$$h' = -\frac{1}{\eta} f h, \tag{3.9b}$$

with the boundary conditions

$$\lim_{\eta\to 0}\left(-\frac{1}{\eta} f'(\eta) + f''(\eta)\right) = 0, \qquad \lim_{\eta\to 0}\left(f(\eta) - \frac{1}{2}\eta f'(\eta)\right) = 0, \tag{3.10}$$

and far field conditions

$$f' = 0, \qquad h = 0, \qquad \text{as } \eta \to \infty, \tag{3.11}$$

with the buoyancy flux condition

$$2\pi \int_0^\infty h f' \, \mathrm{d}\eta = 1. \tag{3.12}$$

The system (3.9)–(3.12) is solved, in the same way as in section 2.2.1, by using two bisection methods to find the values of the shooting parameters $s_f = f'(\eta_0)$ and $s_h = h(\eta_0)$, to find a set of solutions illustrating the variation in form of the vertical velocity and temperature profiles of laminar plumes

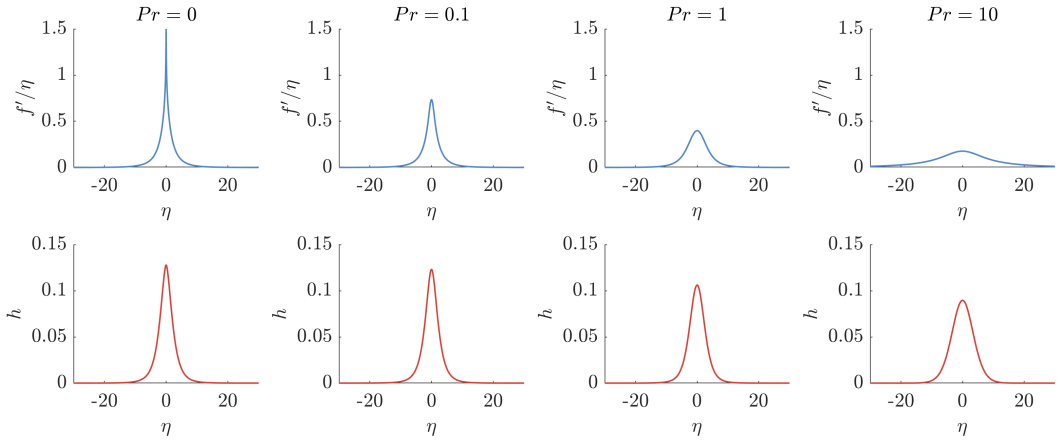

Figure 3.2: Solution to the laminar similarity equations (3.9)–(3.12) for $Pr = 0.1$, 1, 10 and the solution to the inviscid equations (3.13)–(3.14) (equivalent to $Pr = 0$). The top row shows the profile of the similarity vertical velocity, $w = f'/\eta$, while the bottom row shows the profile of the similarity temperature field, $h = zT$. The solutions illustrate a transition between two forms of solution. At small Pr the solution is characterised by profiles in which both the thermal and velocity fields occupy a comparable horizontal scale, with the velocity field exhibiting a sharp singularity at the plume centre for inviscid plumes. At large Pr, the velocity field extends further from the plume centre than the temperature field, with both retaining a smooth profile.

across $Pr = 0.1$, 1, and 10. These solutions are plotted in the three right-hand columns in figure 3.2. As Pr increases the peak vertical velocity and temperature both increase and the width of the profiles widen, with a more drastic effect for the velocity profiles. The centreline values of f and h from the solution to (3.9)–(3.12) for over forty values of the $Pr \in [10^{-3}, 10^{2}]$ are plotted in figure 3.3 to illustrate the trends in the behaviour across Prandtl numbers. In the following two sections, asymptotes are derived by conducting asymptotic analyses for both low and high Pr.

3.3.1 Low-Prandtl number laminar regime

As the Pr becomes small, asymptotic analysis can be used to simplify the laminar similarity system (3.9)–(3.12) and make predictions in the asymptotic limit of $Pr \to 0$. In this limit, the viscous terms in the laminar similarity solution (3.9)–(3.12) can be neglected, leaving the equations describing an

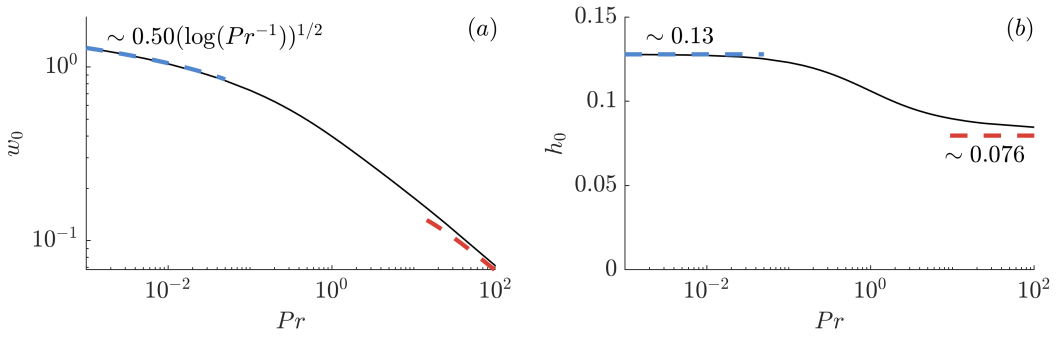

Figure 3.3: The centreline vertical velocity w_0, in panel (a), and similarity temperature $h_0 = zT_0$, in panel (b), for laminar plumes as a function of Pr, as determined from the numerical solution of (3.9)–(3.12) for $Pr \in [10^{-3}, 10^2]$. The asymptotic prediction $h \to 0.13$ as $Pr \to 0$ is shown as a dashed blue line in panel (b). The high-Pr asymptotes (3.21) (Worster, 1986) are plotted as red dashed curves, confirming the limiting trends of our numerical solutions. For both w_0 and h_0, errors resulting from the solution method described in section 2.2.1 are $< 10^{-4}$ which are too small to be visible on the plot for all values of Pr and hence error bars are omitted.

inviscid plume

$$-f\left(\frac{f'}{\eta}\right)' = \eta h, \qquad fh = -\eta h', \tag{3.13}$$

to leading order, with the boundary conditions

$$\lim_{\eta\to 0}(f/\eta) = 0, \qquad \lim_{\eta\to\infty} f'(\eta) = 0, \qquad 2\pi\int_0^\infty hf'\,\mathrm{d}\eta = 1. \tag{3.14}$$

Compared to the full system (3.9)–(3.12), the stress continuity condition at the centre of the plume in (3.10) has been dropped, since velocity (and its spatial gradient) need not be continuous in the idealised limit of inviscid flow. The removal of this boundary condition is consistent with the reduction in order of the momentum conservation equation on neglecting the viscous term.

The system (3.13)–(3.14) is free of parameters, implying that its solution provides a universal asymptotic description of laminar plumes in the limit $Pr \to 0$. It is solved using a shooting method in a similar way to the full system (3.9)–(3.12), by reframing the equations as a set of three ODEs by defining $\mathcal{F}_0 := f$, $\mathcal{F}_1 := f'$, and $\mathcal{H}_0 := h$ and substituting into (3.13), to define

the system

$$\frac{\mathrm{d}\mathcal{F}_0}{\mathrm{d}\eta} = \mathcal{F}_1, \tag{3.15a}$$

$$\frac{\mathrm{d}\mathcal{F}_1}{\mathrm{d}\eta} = \frac{\mathcal{F}_1}{\eta} - \frac{\mathcal{H}_0\eta^2}{\mathcal{F}_0}, \tag{3.15b}$$

$$\frac{\mathrm{d}\mathcal{H}_0}{\mathrm{d}\eta} = -\frac{1}{\eta}\mathcal{F}_0\mathcal{H}_0, \tag{3.15c}$$

with the shooting initial conditions

$$\mathcal{F}_0(\eta_0) = \frac{\eta_0 s}{2}, \qquad \mathcal{F}_1(\eta_0) = s, \qquad \mathcal{H}_0(\eta_0) = t, \tag{3.16}$$

for some η_0 close to zero, where s and t are shooting parameters. The far field and buoyancy flux conditions (3.14) become

$$|\mathcal{F}_1(\eta_{max})| < 10^{-5}, \qquad |\mathcal{H}_0(\eta_{max})| < 10^{-5}, \tag{3.17}$$

and

$$\left| 2\pi \int_0^\infty \mathcal{H}_0\mathcal{F}_1 \, \mathrm{d}\eta - 1 \right| < 10^{-5}, \tag{3.18}$$

respectively. The shooting values s and t are iterated through a bisection search using the integration of (3.15)–(3.16) making use of the integrator `ode15s` (Shampine & Reichelt, 1997) in MATLAB until the far field conditions (3.17) and the buoyancy flux condition (3.18) are satisfied.

The resulting solution for $Pr = 0$ in figure 3.2 (left) exhibits a qualitatively Gaussian similarity temperature field $zT = h(\eta)$, similar to larger Pr, but a vertical velocity $w = f'(\eta)/\eta$ that exhibits a sharp transition to a maximum velocity at the centre of the plume. The sharp increase of the vertical velocity near the plume centre contrasts with the smooth profiles arising for $Pr > 0$, where the requirement that the shear of the flow is continuous (dropped for $Pr = 0$) ensures the curve is smooth. In particular, the centreline values of the velocity and temperature are determined as

$$\lim_{\eta\to 0}(f'/\eta) = \infty, \qquad h(0) = 0.13. \tag{3.19}$$

As illustrated in figure 3.3, a finite Pr indeed regularises the singu-

larity, with an asymptotic trend well represented by

$$w(0) \sim 0.50\,(\log(Pr^{-1}))^{1/2}, \tag{3.20}$$

in the range $Pr \in [10^{-3}, 10^{-2}]$, shown as a dashed blue curve. This expression was obtained by trial and error, taking inspiration from similar expressions in the literature Worster (1986); Kaminski & Jaupart (2003). The solution to (3.13) and (3.14) predicts the centreline value of the similarity temperature $h(0) \approx 0.13$, providing the asymptotic value of the centreline temperature as $Pr \to 0$. As shown in figure 3.3, this value successfully provides the asymptote of the centre-line temperature as $Pr \to 0$.

The work in this section contributes to a description of the behaviour of laminar plumes in the low-Pr limit. This addresses research question 6, having solved the inviscid laminar similarity system (3.13)–(3.14) and introducing a logarithmic trend that well matches the solution to the regular similarity system (3.9)–(3.12) in the low-Pr regime.

3.3.2 High-Prandtl number laminar regime

Asymptotic predictions in the high-Pr limit ($Pr \to \infty$) have been determined previously by Worster (1986). In this limit, the temperature profile is concentrated at the centre of a much broader velocity field. By conducting an asymptotic analysis based on coupling a central viscous region to an outer region dominated by a balance between buoyancy and inertia, Worster (1986) determined the asymptotes for centreline values to be

$$w_0 \sim 0.40\,\varepsilon^2 \log(\varepsilon^{-2}), \qquad h_0 \sim 0.076, \tag{3.21}$$

as $Pr \to \infty$, where ε is a small parameter defined implicitly by $\varepsilon^4 \log(\varepsilon^{-2}) = Pr^{-1}$. The high-$Pr$ asymptote is plotted in red in figure 3.3, showing good agreement with the $Pr \to \infty$ trends of the numerical solution of the similarity equations (3.9)–(3.12).

It is interesting to note that the centreline similarity temperature $zT_0 = h_0$ of a laminar plume is thus universally constrained to lie within the range $0.076 < h(0) < 0.13$.

3.3.3 Initial rise speed

In this subsection, a prediction is developed for the rate at which the top of the plume rises in the unsteady regime. Let $h_p(t)$ denote the leading-order position of top of the plume head. It should be noted that, since the velocity field predicted by the laminar plume theory varies across the width of the plume, the height evolution $h_p(t)$ cannot be directly determined from the velocity profile. To determine a prediction for $h_p(t)$, a global integral constraint on the total buoyancy in the plume system is utilised, in the same way as in section 2.3.4, given by

$$B(t) = \int_0^{h_p(t)} \int_0^{2\pi} \int_0^{\infty} T(r,t)\, r \, \mathrm{d}r \, \mathrm{d}\varphi \, \mathrm{d}z = t. \tag{3.22}$$

Recasting this expression in terms of the similarity variables (3.8) and conducting the z and φ integrals results in

$$B(t) = h_p(t) \left(2\pi \int_0^{\infty} h(\eta)\eta \, \mathrm{d}\eta \right) \equiv h_p(t) E(Pr) = t, \tag{3.23}$$

which predicts that the height of the plume front $h_p(t)$ rises linearly with time t. The Pr-dependent term in parentheses, denoted $E(Pr)$, is the similarity representation of the total buoyancy per unit height of the plume across a horizontal cross-section. The rise rate of the plume during the initial transient can then be predicted from (3.23) by taking the derivative with respect to t and rearranging to find

$$\dot{h}_p = 1/E(Pr). \tag{3.24}$$

The function $E(Pr)$ can be evaluated as a universal function of Pr from the numerical solutions to the similarity equations (3.9)–(3.12), yielding the general relationship for $\dot{h}_p(Pr)$ shown in figure 3.4.

Kaminski & Jaupart (2003) investigate high-Pr laminar plumes and suggest that the initial rise speed is proportional to the bulk flow velocity given in (3.21) (Worster, 1986). Scaling and plotting $0.93Pr^{-1/4}w_0$ in figure 3.4 results in very good agreement with the initial rise speed (3.24) for high-Pr predictions of the solution to the similarity equations (3.9)–(3.12). In the low-Pr regime the initial rise speed of the plume asymptotes to a predicted

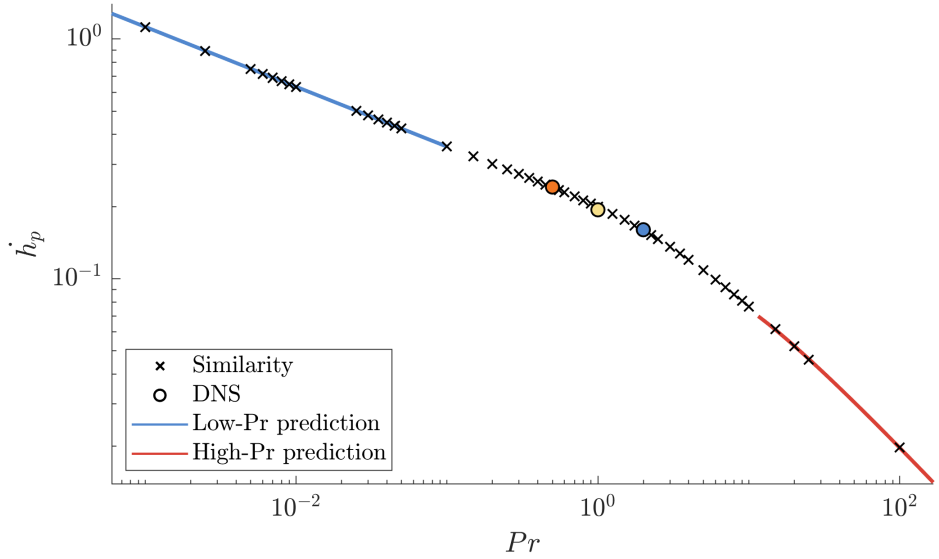

Figure 3.4: The initial rise speed of a laminar plume $\dot{h}_p$ as predicted by the result of (3.24) based on energy conservation. The rise speed approaches an asymptote equal to 0.199 as $Pr \to 0$, attains a global maximum of 0.202 at $Pr \approx 0.4$ (indicated by the filled circle), and decreases proportionally to the bulk flow velocity described in (3.21) as $0.93w_0$.

$\dot{h}_p \approx 0.20 Pr^{-1/4}$ to two significant figures, and agrees with the predictions of initial rise speed (3.24) from the similarity theory for low-Pr in figure 3.4.

The rise speed in the laminar regime is compared to the DNS of (3.2)–(3.5) in figures 3.4 and 3.5. The height of the front of the plume is extracted from the DNS of (3.2)–(3.5) at early times by testing when the velocity of the plume first drops below $w_0(Pr)/2$ (as in section 2.3.2), which is then compared to the prediction of the rise speed from the similarity solution $\dot{h}_p(Pr)$ from (3.24) by plotting $h_p(t) = \dot{h}_p\, t$ in figure 3.5 where $\dot{h}_p(Pr) \approx 0.36$, 0.24, 0.20, and 0.16 to two significant figures, for $Pr = 0.1$, 0.5, 1.0, and 2.0, respectively. There is excellent agreement for $Pr = 0.5$, 1.0, and 2.0, however for $Pr = 0.1$ only the first data point matches the curve predicted by the laminar similarity solution. This discrepancy is because the $Pr = 0.1$ plume undergoes a transition to turbulence at just before $t = 5 \times 10^4$, and the similarity theory is valid only for the laminar regime.

Curves of the form $h_p(t) = \dot{h}_p\, t$ are fitted to the DNS of (3.2)–(3.5) for $t < 3 \times 10^5$ for $Pr = 0.5$ and for $t < 4 \times 10^5$ for $Pr = 1.0$ and 2.0 and values of $\dot{h}_p(Pr)$ are plotted as filled dots in figure 3.4, with error bars that are smaller than the size of each dot. There is excellent agreement with

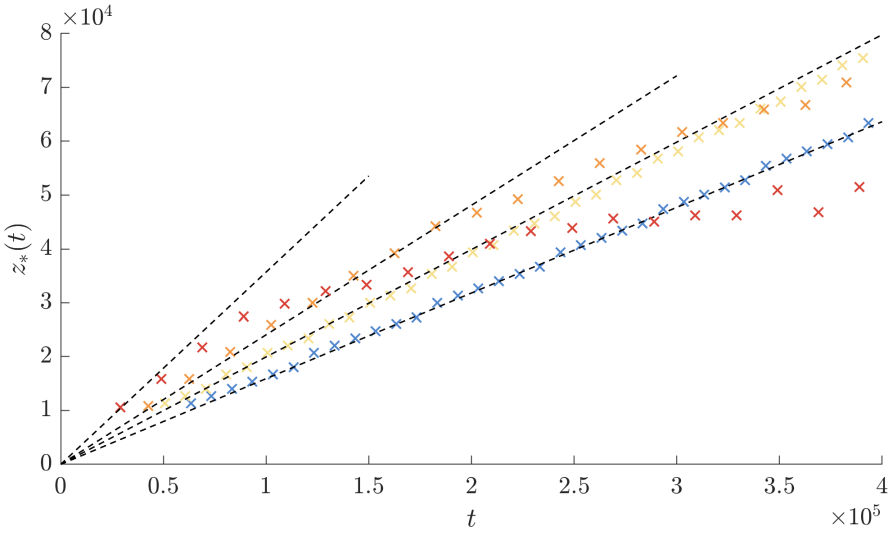

Figure 3.5: The initial rise speed of a laminar plume extracted from the DNS of (3.2)–(3.5) and compared to the predictions from the laminar similarity solution (3.9)–(3.12). The curves $h_p(t) = \dot{h}_p t$ for $Pr = 0.1$, 0.5, 1.0, and 2.0 with $\dot{h}_p(Pr) = 0.36$, 0.24, 0.20, and 0.16, respectively, are plotted as black dashed curves.

the position of the top of the plume during the initial laminar stage, before instability occurs. This prediction also demonstrates good agreement with the work of Moses et al. (1993) for $Pr = 1.0$, who found that the dimensionless head ascent velocity was $\dot{h}_p = 0.23 \pm 0.05$ for $Pr = 1$.

The work in this section has involved developing a new theory for the time-dependent plume head velocity based on a total buoyancy constraint within the plume covering the full spectrum of Prandtl numbers, addressing research question 4. Comparisons have been made to the work of Moses et al. (1993), and Kaminski & Jaupart (2003) in the high-Pr regime, showing excellent agreement with their results.

3.4 Instability and transition to turbulence

The plume becomes turbulent after the transition to instability at $z > z_*$. In this region the turbulent similarity solution (Zeldovich, 1937; Schmidt, 1941), discussed in section 1.1.2, describes the behaviour of the plume, as discussed for the case with $Pr = 1$ in section 2.5. The vertical velocity w and temperature

T in this region are given by

$$w = (z - z_0)^{-1/3}\phi_0 e^{-\alpha_w \xi^2}, \qquad T = (z - z_0)^{-5/3}\vartheta_0 e^{-\alpha_T \xi^2}, \tag{3.25}$$

where the virtual origin for the turbulent regime $z_0(Pr)$ is included in the definition of the similarity variable $\xi = r/(z - z_0)$, $\phi_0(Pr)$, $\vartheta_0(Pr)$ are constants representing the centreline values of vertical velocity and temperature, and $\alpha_w(Pr)$ and $\alpha_T(Pr)$ are constants representing the profile widths.

The work in chapter 2 illustrated that after initial instability, the height of instability $z_*(t)$ rises until it reaches the steady height to instability of z_* (see fig. 2.10). To investigate the dependence of z_* on Prandtl number, DNS of the system (3.2)–(3.5) is performed for $Pr = 0.1$, 0.5, 1.0, and 2.0. Contour plots illustrating the plumes at various Prandtl numbers are included in figure 3.1.

In figure 3.6, the transient height to instability $z_*(t)$ is plotted against time for $Pr = 0.1$, 0.5, 1.0, and 2.0. The value of $z_*(t)$ is found by marking the height at which the vertical velocity first drops beneath half of the vertical velocity at the displaced origin, i.e. $w_0/2$, along the centreline at each time step. By comparing the $w_0/2$ criterion with videos of the plume, I verified that this criterion was appropriate to find z_*. The height to instability $z_*(t)$ is then identified at $t = 1.4 \times 10^7$ and plotted as filled circles in figure 3.6. Error bars are found by tracking the maximum and minimum values of the oscillation in $z_*(t)$ for $t \in [1.3, 1.5] \times 10^7$.

In figure 3.7 the height of instability $z_*(t)$ at $t = 1.4 \times 10^7$ is plotted against Prandtl number for $Pr = 0.1$, 0.5, 1.0, and 2.0. The height to instability rises sub-linearly with Prandtl number over the range of Prandtl numbers studied. A quadratic polynomial, to be used for interpolation, is plotted through the points and plotted as a red, dashed line. The quadratic is determined using the Polyfit function in MATLAB and is found to be

$$z_* \approx (-0.66Pr^2 + 3.09Pr + 2.04) \times 10^5. \tag{3.26}$$

This approximate formula allows for the prediction of $z_*(t)$ at $t = 1.4 \times 10^7$ for any plume with Prandtl number in the range $Pr \in [0.1, 2.0]$ and could also be calculated using the same procedure for any $t < 1.4 \times 10^7$. The work in this chapter goes some way to addressing research question 5, namely describing

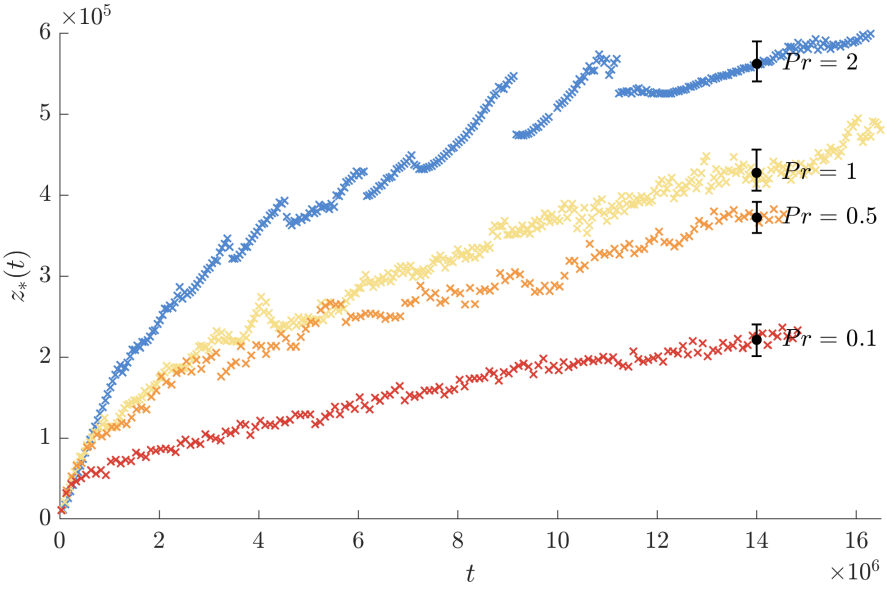

Figure 3.6: Dimensionless height to instability $z_*(t)$ from the DNS of (3.2)–(3.5) for $Pr = 0.1$, 0.5, 1 and 2, illustrating the transient approach to the height to instability. Curves are plotted by finding the lowest height at which the vertical velocity drops beneath half the value at the source $w_0/2$. The value of the height to instability $z_*(t)$ at $t = 1.4 \times 10^7$ is plotted as a black dot for each Pr. Error bars are found by tracking the oscillation in $z_*(t)$ for $t \in [1.3,\ 1.5] \times 10^7$.

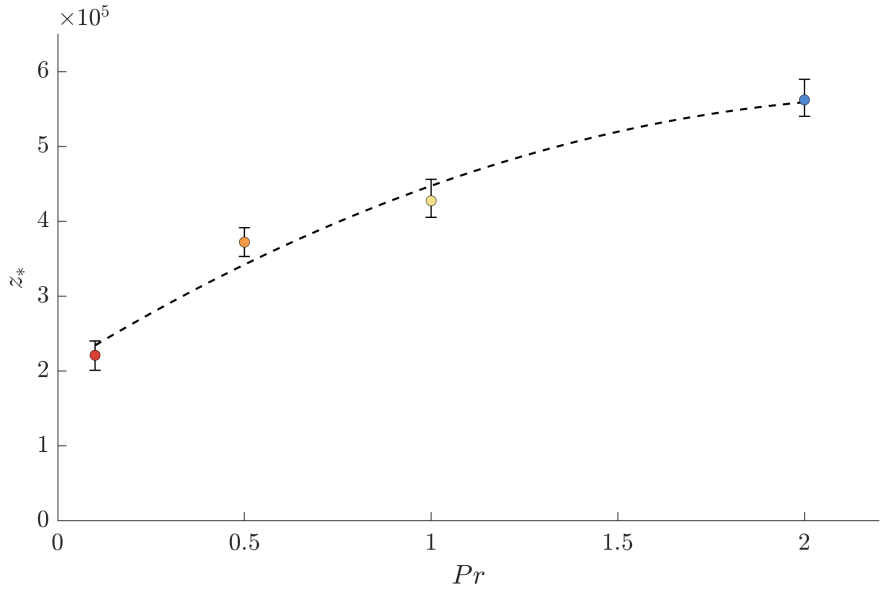

Figure 3.7: Dimensionless height of instability, $z_*(t)$ at $t = 1.4 \times 10^7$, for DNS of (3.2)–(3.5) for $Pr = 0.1, 0.5, 1.0$ and 2.0, illustrating an increasing sub-linear trend. An approximate formula $z_* \approx (-0.66Pr^2 + 3.09Pr + 2.04) \times 10^5$, which could be used for interpolation over this range is indicated by a dashed curve. Error bars are plotted using the maximum and minimum values of $z_*(t)$ over the range $t \in [1.3,\ 1.5] \times 10^7$ as in figure 3.6.

the height to instability z_* for a range of Prantl numbers. While a full theory of a laminar to transitional to turbulent plume is not fully complete for general Prandtl number (as for $Pr = 1$ in section 2.5), a prediction for height to instability $z_*(t)$ in (3.26) for $Pr \in [0.1, 2.0]$ at $t = 1.4 \times 10^7$ was found. Further work could involve running the simulations for a longer time and determining a formula for $z_*(t)$ as the plume reaches an instability at a quasi-steady height as in chapter 2. The DNS could also be performed for a wider range of Prandtl numbers so the prediction of height to instability could be improved using a larger data set. Specific values of $Pr = 0.7$ for air and $Pr = 10$ for water would be especially useful.

3.5 Conclusions

In this chapter, the work from chapter 2 was extended to investigate plumes generated from a point source of heat for a number of different Prandtl numbers. A new theory for initial rise speed of a plume in the laminar regime based on the total buoyancy of the plume, covering the full spectrum of Prandtl numbers, was developed in section 3.3.3, further addressing research question 4. Rise speed was found to become proportional to $Pr^{-1/4}$ as $Pr \to 0$ and decrease according to the results of Kaminski & Jaupart (2003) as $Pr \to \infty$. This new theory was compared to results from the DNS, and excellent agreement for the cases $Pr = 0.5$, 1.0, and 2.0 was found, with the transition to instability occurring too soon to make a comparison for $Pr = 0.1$.

Using the length-scale $L = (\kappa^3/F_0)^{1/2}$ and the time scale $\tau = \kappa^2/F_0$, defined in the scaling analysis in (3.1), and re-introducing hat notation for dimensionless variables, the results from this chapter can be re-dimensionalised. An increasing sub-linear relationship between height to instability and Prandtl number at time $t = 1.4\,(\kappa^2/F_0) \times 10^7$ was found using DNS and is described, to good approximation, by the quadratic polynomial

$$z_* \approx \left(\frac{\kappa^3}{F_0}\right)^{1/2} (-0.66Pr^2 + 3.09Pr + 2.04) \times 10^5, \tag{3.27}$$

for $Pr \in [0.1, 2.0]$. This curve can be used to predict the height to instability for a plume and goes some way towards answering research question 5.

The low- and high-Pr asymptotes were confirmed using DNS of (3.2)–(3.5) in the range $Pr \in [0.1, 2.0]$ and the centreline vertical velocity and temperature in the laminar regime for the full spectrum of Prandtl numbers was described. Section 3.3.1 contributes to a description of the behaviour of laminar plumes in the low-Pr limit, thereby addressing research question 6, by finding a solution to the inviscid laminar similarity system (3.13)–(3.14) and introducing a logarithmic trend (3.20) that matches the solution to the regular similarity system (3.9)–(3.12) in the low-Pr regime, for $Pr \in [10^{-3}, 10^{2}]$.

3.5.1 Limitations and further work

The work in this chapter lays the groundwork for a fundamental theory describing any plume in an unstratified environment emanating from a point source. With some further DNS at $Pr = 0.1$ and 0.5 to check mesh sensitivity and run over a larger time window, and a larger domain for $Pr = 2.0$, the interpolation formula could be extended to capture the quasi-steady height to instability as in chapter 2. Also, with just a few more DNS at different Prandtl numbers, a wider data set would allow for more accurate interpolation, and over a wider range. Another important parameter, the virtual origin of the turbulent regime z_0 (given in section 2.5), would be an ideal candidate for interpolation. This would require more simulations with much larger domains to capture the turbulent region, however, but would result in a complete description of all plumes emanating from a point source in a quiescent, unstratified environment.

Chapter 4

The effect of Reynolds number on plumes in a stratification

Contents

The case of a plume in an unstratified environment was the focus of study in the previous two chapters. Plumes in the physical world commonly occur in a stratified environment, one in which the density of the background varies with height. In this chapter, a plume emanating from a point source and flowing into a linearly stratified environment is investigated. As discussed

in section 1.1.4, many previous studies of plume rise in a stratification have often focused on turbulent plumes (Morton et al., 1956; Plourde et al., 2008; Devenish et al., 2010; Rooney & Devenish, 2014; Fabregat Tomàs et al., 2016), using scaling and numerical simulations to develop theories and predictions of a plume in a stratification. Some studies have investigated the rise of laminar plumes (Lombardi et al., 2011; Xue et al., 2019). However, I could not find any studies that have investigated the rise height of plumes across a wide range of Reynolds numbers, encompassing both laminar and turbulent plumes (pertaining to research questions 7 and 8).

In this chapter, a theoretical analysis of the fundamental flow of a pure plume generated by a localised buoyancy source in a stratification is presented. Using direct numerical simulations (DNS), universal properties of pure plumes fixing Prandtl number $Pr = 1$ are investigated, addressing the Reynolds number dependent maximum rise height and the impact of stratification on the transition to instability of a plume generated by a point source of heat.

Initially, in section 4.1, the governing equations of a plume in a linear stratification are presented, followed by a scaling analysis and a non-dimensionalisation in section 4.2. The details of modelling a plume using DNS are discussed in section 4.3 along with a description of numerical results for a range of Reynolds numbers. This is followed by a discussion of the maximum rise height of a plume in section 4.4, addressing research question 7. Subsequently, a comparison between the height to instability and maximum rise height is undertaken in section 4.5, addressing research question 8. Scaling analysis and simplified models are presented for the laminar regime in section 4.6, addressing research question 7 in more detail. Section 4.7 uses scaling analysis for the turbulent regime to comment on the maximum rise height of turbulent plumes in a stratification, and on an appropriate numerical Reynolds number for modelling extremely large Reynolds number plumes, thereby addressing research questions 7 and 9, respectively. Finally, concluding remarks are made and further work discussed in section 4.8.

4.1 Modelling a plume emanating from a point source in a stratified environment

A background fluid is said to be stratified if the density varies with height. When first initiated, a plume in a stratified environment will rise under a force of buoyancy, as in an unstratified environment, with the stratification exhibiting a negligible impact on the flow. As the plume rises, the buoyancy of the plume fluid decreases until it reaches a neutral buoyancy level (NBL) where the buoyancy is zero. Momentum carries the plume fluid above the NBL and the buoyancy becomes negative. The plume then oscillates about the NBL while moving laterally outwards away from the plume centre and forms a neutrally buoyant gravity current, often referred to as an umbrella region in volcanology.

In chapter 2, a plume in an unstratified environment was shown to depend on only a single dimensionless parameter, the Prandtl number. In this chapter, a plume in a linearly stratified ambient will be shown to depend on two parameters, the Reynolds number and the Péclet number. A plume in a stratified environment, emanating from a point source, is modelled using the incompressible Navier-Stokes equations and temperature conservation equation (1.1) under the Boussinesq approximation, which implies that density variation only plays a significant role in the buoyancy term. The system reads

$$\rho_0 \frac{D\boldsymbol{u}}{Dt} = -\boldsymbol{\nabla} p + \rho_0 \nu \nabla^2 \boldsymbol{u} + \rho g \hat{\boldsymbol{z}}, \tag{4.1a}$$

$$\boldsymbol{\nabla} \cdot \boldsymbol{u} = 0, \tag{4.1b}$$

$$\frac{DT}{Dt} = \kappa \nabla^2 T, \tag{4.1c}$$

where $\boldsymbol{x} = (x, y, z)$ is the spatial coordinate vector, t is time, $\boldsymbol{\nabla}$ is the gradient operator, $\boldsymbol{u}(\boldsymbol{x}, t) = (u, v, w)$ is the fluid velocity, p is fluid pressure, $\rho = \rho(\boldsymbol{x}, t)$ is the fluid density, ρ_0 is a reference density, ν is the kinematic viscosity, $T(\boldsymbol{x}, t)$ is the temperature, κ is the thermal diffusivity, and g is the acceleration due to gravity. The background is assumed to be linearly stratified and the equation of state, relating the density to the temperature, is given by

$$\rho(\boldsymbol{x}, t) = \rho_0(1 - \beta(T(\boldsymbol{x}, t) - T_0)), \tag{4.2}$$

where β is the constant coefficient of thermal expansion and T_0 is a reference value of temperature, related to ρ_0, usually chosen as the value of the environment at the ground level. The temperature is then decomposed into

$$T(\boldsymbol{x}, t) = \vartheta(\boldsymbol{x}, t) + T_0 + \zeta z, \tag{4.3}$$

where ζz represents the linear profile for constant ζ and $\vartheta(\boldsymbol{x}, t)$ is the temperature difference from the background which has linear temperature profile $T_e(\boldsymbol{x}) = T_0 + \zeta z$ and density profile

$$\rho_e = \rho_r(1 - \beta(T_e - T_0)) = \rho_r(1 - \beta\zeta z). \tag{4.4}$$

The value of ϑ for any point outside of the plume is $\vartheta = 0$, corresponding to no perturbation of the temperature field. The Brunt-Väisälä frequency N, given by

$$N^2 = -\frac{g}{\rho_r}\frac{\mathrm{d}\rho_e}{\mathrm{d}z} = g\beta\zeta, \tag{4.5}$$

represents the strength of the stratification of the background.

The equations (4.1) are rewritten in terms of temperature difference ϑ by substituting the equation of state (4.2) and the temperature decomposition (4.3) into the governing equations (4.1), resulting in the Navier-Stokes and temperature difference conservation equations

$$\frac{D\boldsymbol{u}}{Dt} = -\frac{\boldsymbol{\nabla}\tilde{p}}{\rho_0} + \nu\nabla^2\boldsymbol{u} + g\beta\vartheta\hat{\boldsymbol{z}}, \tag{4.6a}$$

$$\boldsymbol{\nabla}\cdot\boldsymbol{u} = 0, \tag{4.6b}$$

$$\frac{D\vartheta}{Dt} = \kappa\nabla^2\vartheta - \zeta w, \tag{4.6c}$$

where the pressure has been redefined to incorporate background terms from the buoyancy term $\tilde{p} = p + \rho_0 g(1 - \beta\zeta z/2)z$. From here on this tilde-notation for the pressure is dropped. As in the unstratified case, the solution to the equations above is considered in the semi-infinite region $z \geq 0$ subject to no-slip and insulation conditions at $z = 0$ (1.2), given by

$$\boldsymbol{u}(x, y, 0, t) = \boldsymbol{0}, \qquad \frac{\partial\vartheta}{\partial n}(x, y, 0, t) = 0, \tag{4.7}$$

respectively. In the far-field of the domain it is assumed that the fluid is

stationary and the temperature difference from the ambient is zero (1.3), as specified by

$$\lim_{R\to\infty} \boldsymbol{u} = \boldsymbol{0}, \qquad \lim_{R\to\infty} \vartheta = 0, \tag{4.8}$$

where $R = \sqrt{x^2 + y^2 + z^2}$ is the spherical radial coordinate. To prescribe the source of buoyancy, a point-source condition of constant thermal flux (1.4),

$$\lim_{\varepsilon\to 0} \int_{S_\varepsilon} \left(-\kappa \frac{\partial \vartheta}{\partial n}\right) \, \mathrm{d}S = F_0, \tag{4.9}$$

is imposed, where S_ε is the hemisphere of radius $R = \varepsilon$ in the region $z \geq 0$, and F_0 is the prescribed buoyancy source flux.

4.1.1 Plume fluxes

As in chapters 2 and 3, it is assumed that the contribution of the convective buoyancy flux to the total buoyancy flux is negligible at a sufficient height above the point source, namely at the displaced origin $z = z_s > 0$. The buoyancy flux of the plume in an unstratified regime is derived in section 2.1.1. For the stratified regime, the process for deriving the buoyancy flux is similar, resulting in the equation for the buoyancy flux of a plume in a stratification

$$F(z,t) = 2\pi \int_0^\infty g\beta r \vartheta w \, \mathrm{d}r. \tag{4.10}$$

Notably, this is no longer constant with height as it was in the unstratified plume, as shown in the solution to the model given by Morton et al. (1956), reviewed earlier in figure 1.4.

As in chapters 2 and 3, it is useful to consider the volume Q and momentum M fluxes. Both Q and M are not explicitly changed by the introduction of stratification, and hence are given by

$$Q(z,t) = 2\pi \int_0^\infty rw \, \mathrm{d}r, \qquad M(z,t) = 2\pi \int_0^\infty rw^2 \, \mathrm{d}r. \tag{4.11}$$

While Q and M do not appear explicitly in the model definition, they can be used for comparison between theory and simulations.

4.2 Intrinsic scales and non-dimensionalisation

The system (4.6)–(4.9) is dependent on a total of six parameters: ρ_0, ν, κ, $(g\beta)$, N, and F_0 (where $\zeta = N^2/g\beta$). Performing a scaling analysis to determine the intrinsic scales and subsequently using them to non-dimensionalise, this six-way dependence can be reduced to a dependence on two parameters. In the previous two chapters, the various scalings between terms were chosen such that the height to instability was fixed by the non-dimensionalisation. In this chapter, the rise height of plumes in a stratification is the main quantity of interest and so the non-dimensionalisation is chosen to fix this value. By comparing the advection and forcing terms in the momentum equation (4.6a), the advection and source terms in the temperature equation (4.6c), and the terms in buoyancy flux condition (4.10), the following scaling relationships between length $\boldsymbol{x} \sim L$, time $t \sim \tau$, and temperature difference $\vartheta \sim \Theta$ are uncovered

$$L \sim g\beta\Theta\tau^2, \qquad \Theta \sim \frac{N^2}{g\beta}L, \qquad F_0 \sim g\beta\frac{\Theta L^3}{\tau}. \tag{4.12}$$

Rearranging results in the intrinsic scalings for length, time, and temperature in terms of the stratification frequency and initial buoyancy flux

$$L \sim \left(\frac{F_0}{N^3}\right)^{1/4}, \qquad \tau \sim \frac{1}{N}, \qquad \Theta \sim \frac{1}{g\beta}\left(F_0 N^5\right)^{1/4}. \tag{4.13}$$

The model in (4.6) is subsequently non-dimensionalised by defining the dimensionless variables, denoted by hats,

$$\boldsymbol{x} = L\hat{\boldsymbol{x}}, \quad t = \tau\hat{t}, \quad \boldsymbol{u} = \frac{L}{\tau}\hat{\boldsymbol{u}}, \quad p = \rho_0\left(\frac{L}{\tau}\right)^2\hat{p}, \quad \vartheta = \Theta\hat{\vartheta}, \tag{4.14}$$

and substituting. On dropping hats, (4.6) becomes

$$\frac{D\boldsymbol{u}}{Dt} = -\boldsymbol{\nabla}p + \frac{1}{Re}\nabla^2\boldsymbol{u} + \vartheta\hat{\boldsymbol{z}}, \tag{4.15a}$$

$$\boldsymbol{\nabla}\cdot\boldsymbol{u} = 0, \tag{4.15b}$$

$$\frac{D\vartheta}{Dt} = \frac{1}{Pe}\nabla^2\vartheta - w, \tag{4.15c}$$

where the Reynolds and the Péclet number are given by

$$Re = \left(\frac{F_0}{N\nu^2}\right)^{1/2}, \qquad Pe = \left(\frac{F_0}{N\kappa^2}\right)^{1/2}. \tag{4.16}$$

Interestingly, in this non-dimensionalisation, the parameter controlling the strength of the stratification ζ is removed from the equations implying that the solution is independent of stratification strength, subject to scaling by (4.13). The no-slip and far-field conditions, (4.7) and (4.8), remain unchanged in form, namely,

$$\boldsymbol{u}(x, y, 0, t) = \mathbf{0}, \qquad \frac{\partial \vartheta}{\partial n}(x, y, 0, t) = 0, \tag{4.17}$$

and

$$\lim_{R\to\infty} \boldsymbol{u} = \mathbf{0}, \qquad \lim_{R\to\infty} \vartheta = 0, \tag{4.18}$$

respectively. The source condition (4.9), after substitution of (4.14), becomes

$$\lim_{\varepsilon\to 0} \int_{S_\varepsilon} r \left(-\frac{\partial \vartheta}{\partial n}\right) \, \mathrm{d}S = 1. \tag{4.19}$$

The dimensionless system (4.15)–(4.19) describes the initialisation and development of a plume in a stratification at given Reynolds and Péclet numbers, depending on the initial buoyancy flux F_0, stratification frequency N, and the material properties of kinematic viscosity ν and thermal diffusivity κ. As the Prandtl number $Pr = Pe/Re$, adding a linear stratification to the problem of a plume emanating from a point source of heat results in the addition of one more dimensionless variable.

The advective buoyancy flux (4.10) is also non-dimensionalised by substituting (4.14) and subsequently dropping hats, resulting in

$$F(z, t) = 2\pi \int_0^\infty r\vartheta w \, \mathrm{d}r. \tag{4.20}$$

Similarly, the volume Q and momentum M fluxes can be non-dimensionalised and hats dropped to find

$$Q(z, t) = 2\pi \int_0^\infty rw \, \mathrm{d}r, \qquad M(z, t) = 2\pi \int_0^\infty rw^2 \, \mathrm{d}r. \tag{4.21}$$

4.2.1 Scaling between unstratified and stratified regimes

It is useful to be able to apply some of the results obtained in chapters 2 and 3, such as the height to instability z_*, to the work in this chapter. To do this, a scaling between the two different non-dimensionalisations is required. This is facilitated by defining the length L^*, time τ^*, and temperature $\mathcal{T}^*$ scales

$$L^* \sim Pe_*^{3/2}, \qquad \tau^* \sim Pe_*^2, \qquad \mathcal{T}^* \sim Pe_*^{-5/2}. \tag{4.22}$$

The dimensionless model describing plume flow in an unstratified environment (2.17) is rescaled by defining the new variables, using bars to denote variables in the unstratified non-dimensionalisation,

$$\overline{\boldsymbol{x}} = L^*\boldsymbol{x}, \quad \overline{\boldsymbol{u}} = \frac{L^*}{\tau^*}\boldsymbol{u}, \quad \bar{p} = \left(\frac{L^*}{\tau^*}\right)^2 p, \quad \overline{T} = \mathcal{T}^* T, \quad \bar{t} = \tau^* t. \tag{4.23}$$

On substituting (4.23) into the governing equation for a plume in an unstratified environment (2.17), the equations become

$$\frac{D\boldsymbol{u}}{Dt} = -\boldsymbol{\nabla} p + \frac{1}{Re}\nabla^2\boldsymbol{u} + T\hat{\boldsymbol{z}}, \tag{4.24a}$$

$$\boldsymbol{\nabla}\cdot\boldsymbol{u} = 0, \tag{4.24b}$$

$$\frac{DT}{Dt} = \frac{1}{Pe}\nabla^2 T, \tag{4.24c}$$

which recover those used for describing plumes in a stratification (4.15), once the equation of state (4.2) and temperature perturbation (4.3) are substituted. In effect, this means that the theory of height to instability $\bar{z}_*$ for unstratified plumes can be compared to the results from the DNS of stratified plumes, if we assume that the stratification does not have a large impact on the value of z_* (which may not be the case, however this scaling enables easy comparison). The height to instability $\bar{z}_*$ is scaled into the non-dimensionalisation for plumes in a stratification, described in section 4.2, by using the length scale in (4.22) to define the scaled height to instability

$$z_* = Pe^{-3/2}\bar{z}_*. \tag{4.25}$$

It is important here to note that all the plumes considered in this chapter are chosen to have $Pr = 1$. Since $Pr = Pe/Re$ it hence holds that the Péclet number is equal to the Reynolds number $Pe = Re$ in this chapter.

In a stratification, a steady plume consists of a number of flow regimes. Initially, there exists a laminar region in which the flow approximates the plume in an unstratified environment, discussed in chapters 2 and 3. Subsequently, the scaling (4.25) indicates an inverse relationship between height to instability and Reynolds number, therefore predicting the existence of a critical Reynolds number at which the height to instability will occur beneath the neutral buoyancy level (NBL). Depending on the Reynolds number, the flow will either transition to instability before the NBL (high-Reynolds number), arriving at the NBL turbulent, or will not transition to instability (low-Reynolds number). In both cases, the buoyancy of the plume becomes negative on overshooting and forms a laterally spreading, neutrally buoyant gravity current around the NBL.

4.3 Direct numerical simulations of plumes in a stratification

The system (4.15)–(4.19) is solved using direct numerical simulations (DNS) using the open source, spectral element (SEM) code, Nek5000 (Fischer et al., 2008), as in chapters 2 and 3. A description of the solver and the SEM was included in section 1.2.

4.3.1 Source conditions

In section 2.3.4, using the advective source condition (4.10) and the laminar similarity solution for a plume in an unstratified environment (1.30)–(1.33) was shown to be a reasonable assumption to initialise the unstratified plume at a displaced origin. This removes the need to resolve a point source in the DNS. Despite the introduction of a stratification, this assumption is again made by assuming that in the region between the point source and the displaced origin $z < z_s$ the effect of the stratification on the development of the plume flow is negligible, i.e. $\vartheta \gg z$ in (4.20).

As in chapters 2 and 3, a set of splines representing the laminar similarity solution (1.30)–(1.33) is used to represent the conditions at the source at the displaced origin $z = z_s$. The splines are a set of k third-order piece-

wise continuous polynomials mapping values from an interval to the set of real numbers such that $S_{(w)}, S_{(z^{1/2}u)}, S_{(zT)} : [0, \eta_{\max}] \to \mathbb{R}$, first defined in section 2.3.4. They define the spline for vertical velocity w, radial velocity u, and temperature T, respectively, by

$$S_{(w)}(\eta) = \begin{cases} P_1(\eta) = a_1\eta^3 + b_1\eta^2 + c_1\eta + d_1, & 0 \le \eta < \eta_2, \\ P_i(\eta) = a_i\eta^3 + b_i\eta^2 + c_i\eta + d_i, & \eta_i \le \eta < \eta_{i+1} \text{ for } i = 2, ..., k-1, \\ P_k(\eta) = a_k\eta^3 + b_k\eta^2 + c_k\eta + d_k, & \eta_k \le \eta < \eta_{\max}, \end{cases} \tag{4.26}$$

ans similarly for $S_{(z^{1/2}u)}$ and $S_{(zT)}$, where $\eta = rz^{-1/2}$. The coefficients a_i, b_i, c_i, d_i are determined using MATLAB's splinefit function to fit k polynomials to the similarity solutions for w, u, and T. The similarity scalings (1.26) are then used to write w, u, and T at the displaced origin in terms of the splines

$$w_s(r) = S_{(w)}(rz_s^{-1/2}), \tag{4.27a}$$
$$u_s(r) = z_s^{-1/2} S_{(z^{1/2}u)}(rz_s^{-1/2}), \tag{4.27b}$$
$$\vartheta_s(r) = z_s^{-1} S_{(zT)}(rz_s^{-1/2}). \tag{4.27c}$$

4.3.2 Simulation set-up

The computational domain is a cylinder with the source located in the centre of the lower base. The radius and height of the domain is variable for each simulation with details given in table 4.1. As discussed in previous sections, the simulation is initialised at a displaced origin so as not to explicitly model the point source. The height of the displaced origin is heuristically given by

$$z_s = \min(0.2,\ Re^{-3/2} \times 10^4). \tag{4.28}$$

This choice of z_s ensures that the displaced origin is not located above, or in fact close to, the height to instability z_* or the neutral buoyancy level (NBL) for any values of Reynolds number Re. If z_s was chosen to be a fixed value of 0.2, then, using the scaling in (4.25), the height of the displaced origin z_s and the height to instability z_* become of a similar size at $Re \approx 15,000$. Therefore a decreasing value of z_s is chosen for $Re \to \infty$ such that there is enough height

for the laminar flow to develop after leaving the displaced origin. At the other end of the Re spectrum, if the value of z_s was chosen to vary as $Re^{-3/2} \times 10^4$, this would result in $z_s \to \infty$ as $Re \to 0$. Later, the NBL will be shown to decrease as $Re \to 0$, requiring a cut-off value of z_s for lower Reynolds numbers, chosen to be 0.2, to ensure that the displaced source height z_s is less than the NBL. This condition ensures that the displaced origin is located at a height of $z_s = 0.2$ for $Re \lesssim 1360$ and is illustrated in figure 4.1.

As in chapter 2, the time displacement is calculated using a formula for total buoyancy in the plume, given by (2.46) as $t_s = E(Pr)z_s$ where $E \approx 5.01$ for $Pr = 1$. As previously, the data in all plots are given by the simulations for times $t > t_s$ and heights $z > z_s$.

Re	r_e	z_e	N_{el}	p	N_p ($\times 10^6$)	N_p/V	NBL	RH
10	2.0	8.0	7560	5	0.95	9400	1.12	1.28
20	-	-	-	-	-	-	1.51	1.93
50	-	-	-	-	-	-	2.28	3.40
100	-	-	-	7	2.59	25,794	3.18	5.19
200	-	-	-	-	-	-	4.66	7.15
400	-	15.0	17,700	-	6.07	32,708	6.41	9.82
500	-	-	-	-	-	-	7.09	11.20
700	-	19.0	21,168	-	7.26	30,410	8.40	13.17
1000	-	-	-	-	-	30,410	10.02	15.51
1500	-	21.0	-	9	15.4	58,476	12.31	18.18
2000	-	21.0	24,948	-	18.2	68,918	13.56	15.76
2500	-	21.0	-	-	-	-	11.18	12.84
3000	-	17.0	-	-	-	85,134	7.20	8.84

Table 4.1: Details of parameters used for DNS of (4.15)–(4.19) for each Reynolds number given in column one. Domain parameters are domain radius r_e and domain height z_e. Mesh parameters are number of elements N_{el}, order of the basis polynomials p for the SEM, and number of degrees of freedom $N_p = N_{el} \cdot p^3$ and N_p/V is the number of computational points in each mesh N_p divided by the volume $V = \pi r_e^2 z_e$, to illustrate that the density of computational points increases with increasing Re. A dashed entry indicates that values are equal to those given above. Finally, results of neutral buoyancy level (NBL) and rise height (RH) from each simulation are included, accurate to two decimal places.

As per the SEM, the domain is spatially discretised into a mesh of N_{el} elements. A mesh in which the elements are clustered towards the centre of the domain and towards the source is specified using a geometric progression. The elements are then fanned outwards from the centre and subsequently re-

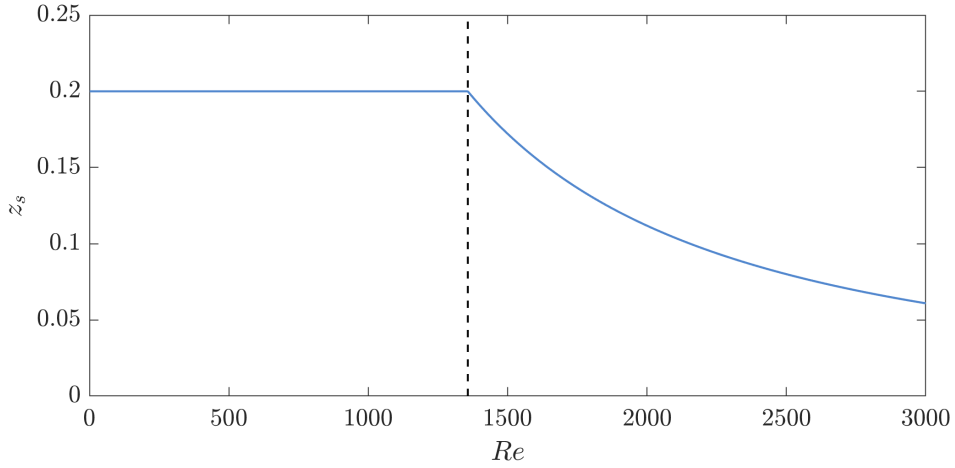

Figure 4.1: Height of the displaced origin z_s, as described by (4.28), with Reynolds number Re. The value is chosen to be constant for $Re \lesssim 1360$ and is decreasing thereafter according to $z_s = \min(0.2, Re^{-3/2} \times 10^4)$.

positioned to reduce aspect ratios of the elements. By virtue of the SEM, the elements are further sub-divided using Legendre polynomials up to pth order. Details can be found in table 4.1. The source condition is specified using the splines for the laminar similarity solution in (4.27).

As in chapters 2 and 3, the zero Neumann boundary conditions (2.34) are applied at the edges of the domain and turbulent eddies are suppressed from moving through these edges by using an adapted Reynolds number (i.e. a numerical sponge layer) at the edge of the domain, given by (2.35).

4.3.3 Mesh sensitivity

Due to the number of simulations required for this study (see table 4.1), it was infeasible to perform a mesh sensitivity study for all Reynolds numbers. It is therefore possible that the results included here do indeed have some dependence on the grid. Nonetheless, however, the qualitative trends uncovered are still interesting and can be verified by further simulations. Checks with scaling analysis and theoretical models later in the chapter also go some way to verifying the DNS, particularly for low Reynolds numbers in the laminar regime.

4.3.4 Illustration of plume evolution and structure

As an illustration of the behaviour of a plume in a stratification, the numerical solutions to the system (4.15)–(4.19) are considered for the cases $Re \in [10, 3000]$ and $Pr = 1$, which by definition means $Pe = Re$.

The time dependent flow behaviour of the solution to (4.15)–(4.19) is illustrated in figures 4.2 to 4.4 for three different Reynolds numbers. In the top rows of each figure snapshots of vertical velocity w, radial velocity u, and temperature T, respectively in each figure, are displayed for $Re = 100$. In this case, the flow is laminar at all heights and quickly reaches its maximum rise height at $z \approx 5.2$ before spreading along the NBL at $z \approx 3.2$. In the middle rows, snapshots for $Re = 500$ are included. Initially, the flow is laminar and travels quickly, but the head undergoes an instability before reaching the maximum rise height. The flow then progresses more slowly while the front of the transient plume is turbulent. The laminar stem pushes through the turbulent head and while the steady plume stem is fully laminar, the maximum rise height fluctuates, averaging out to a value of $z \approx 11.2$, exhibiting turbulent behaviour as the buoyancy reverses while the flow begins to spread laterally along the NBL at $z \approx 7.1$. Finally, in the bottom rows, snapshots are presented for $Re = 3000$. In this case the steady height to instability occurs at $z \approx 6.0$ and there exists a turbulent stem before reaching the NBL at $z \approx 7.2$ and maximum rise height at $z \approx 8.8$.

Images of the flow after the plume has reached its maximum rise height and begun spreading along the NBL (evidenced later in figure 4.8) for vertical velocity w, horizontal velocity u, and temperature T are compared for a variety of Reynolds numbers in figures 4.5 to 4.7, respectively. In each figure the solution to the unstratified laminar similarity solution (2.25)–(2.28) has been added to the region $z < z_s$ (defined for each Re in (4.28)). Remarkably, the global maximum rise height increases up to a Reynolds number of $Re = 1500$ and subsequently decreases thereafter. The overshoot region is larger for simulations that reach the maximum rise height with laminar stem intact. The cone-like spread of the turbulent regime predicted by the turbulent similarity solution (1.35) is evident for high Re plumes.

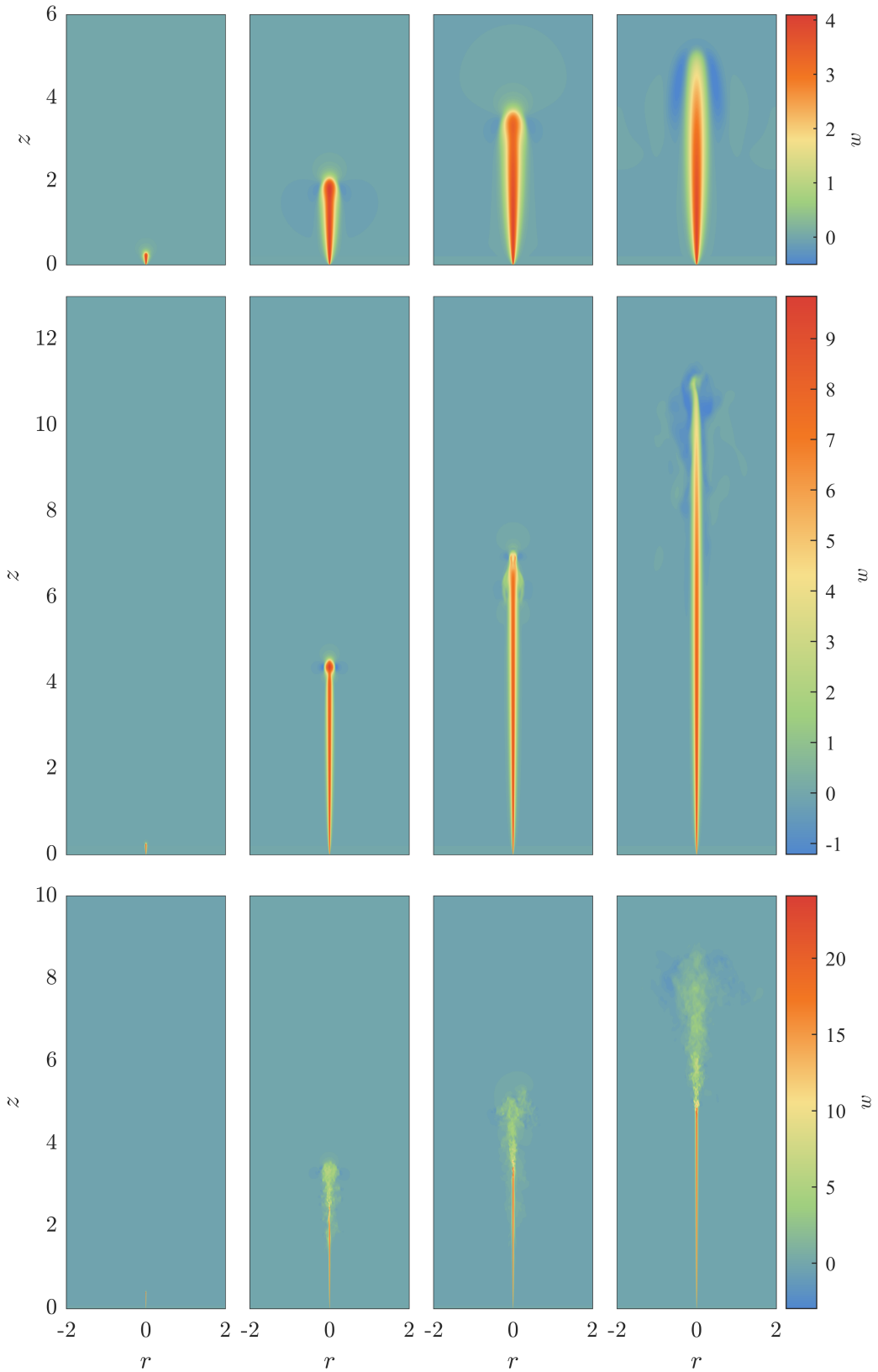

Figure 4.2: Showcase of rz-plane snapshots of vertical velocity w from the DNS of (4.15)–(4.19) at $Re = 100$, 500, 3000 (from top to bottom), with $Pr = 1$, at times $t = 0.01$, 1.0, 2.0, 30.0 (from left to right). In each case the similarity solution (2.25)–(2.28) has been added to the region $z < z_s$, defined in (4.28) for each Re. The final panels are the representation of the statistically steady state of the plume, the neutrally buoyant gravity current regions are indistinguishable from the background because the vertical velocity is close to zero in these regions.

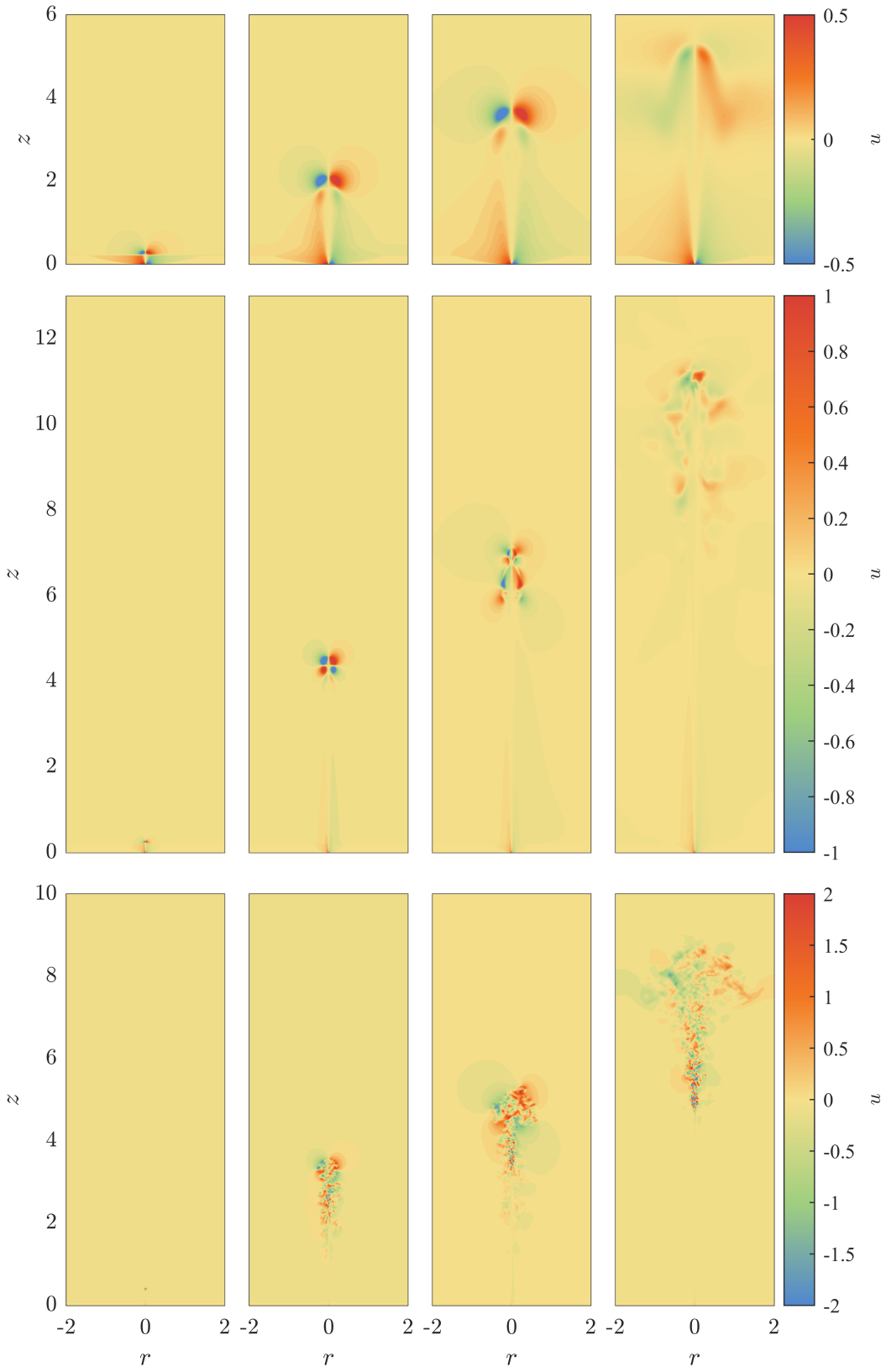

Figure 4.3: Showcase of rz-plane snapshots of radial velocity u from the DNS of (4.15)–(4.19) at $Re = 100$, 500, 3000 (from top to bottom), with $Pr = 1$, at times $t = 0.01$, 1.0, 2.0, 30.0 (from left to right). In each case the similarity solution (2.25)–(2.28) has been added to the region $z < z_s$, defined in (4.28) for each Re. The final panels are the representation of the statistically steady state of the plume.

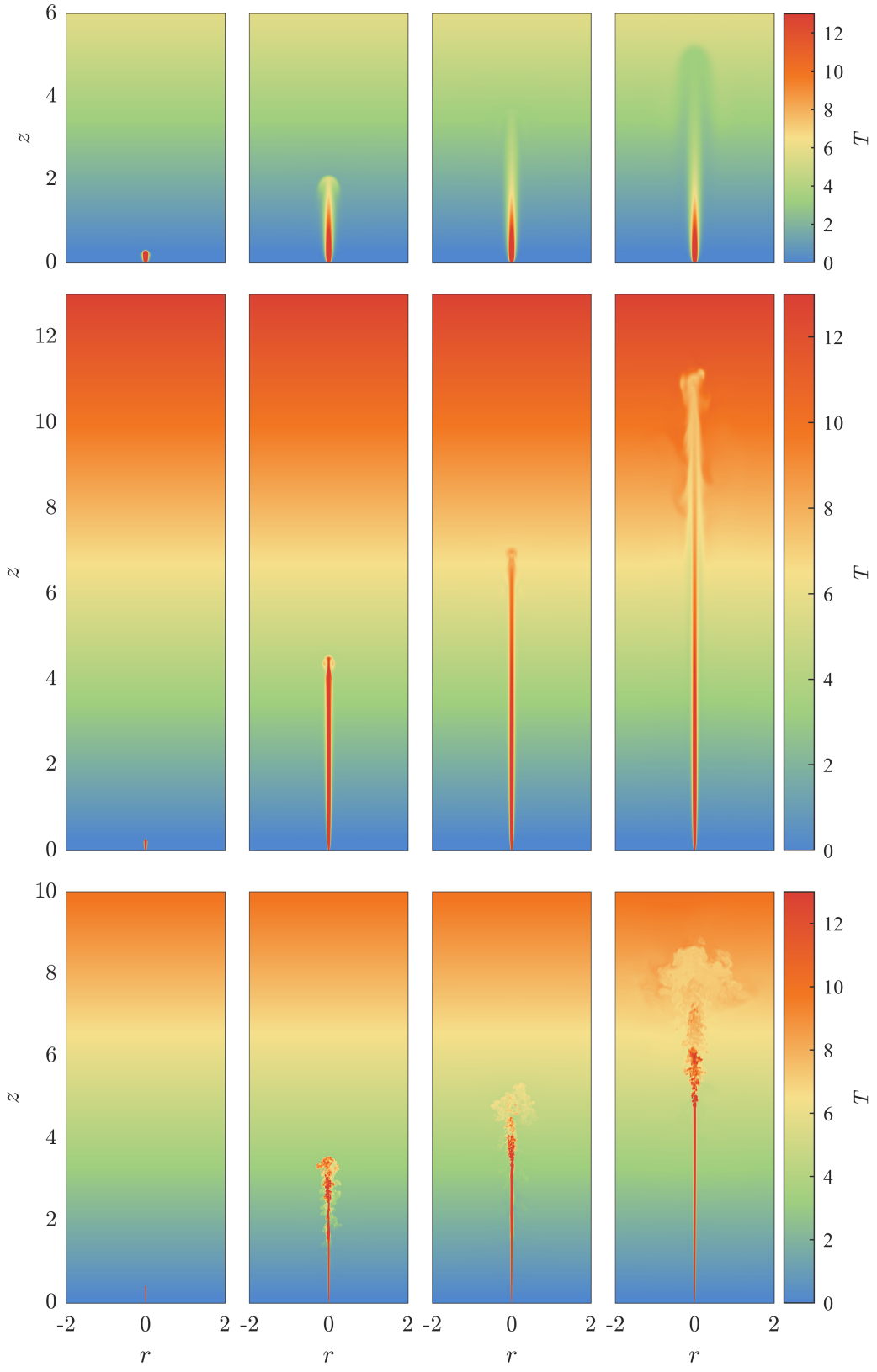

Figure 4.4: Showcase of rz-plane snapshots of temperature T from the DNS of (4.15)–(4.19) at $Re = 100$, 500, 3000 (from top to bottom), with $Pr = 1$, at times $t = 0.01$, 1.0, 2.0, 30.0 (from left to right). In each case the similarity solution (2.25)–(2.28) has been added to the region $z < z_s$, defined in (4.28) for each Re. The final panels are the representation of the statistically steady state of the plume, the gravity current regions are indistinguishable from the background because they are neutrally buoyant.

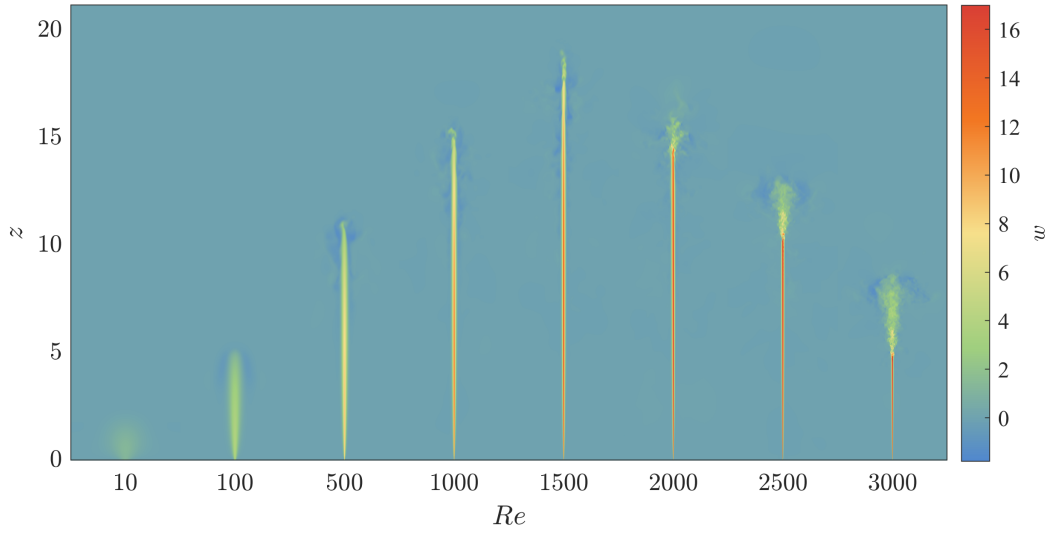

Figure 4.5: Showcase of rz-plane snapshots of vertical velocity w taken from DNS of (4.15)–(4.19) at various Reynolds numbers, all with $Pr = 1$, and all at time $t \approx 30$, after the plume has reached its maximum rise height. The global maximum rise height increases to a maximum at $Re \approx 1500$ and then begins to decrease as $Re \to \infty$. In each case the similarity solution (2.25)–(2.28) has been added to the region $z < z_s$, defined in (4.28) for each Re.

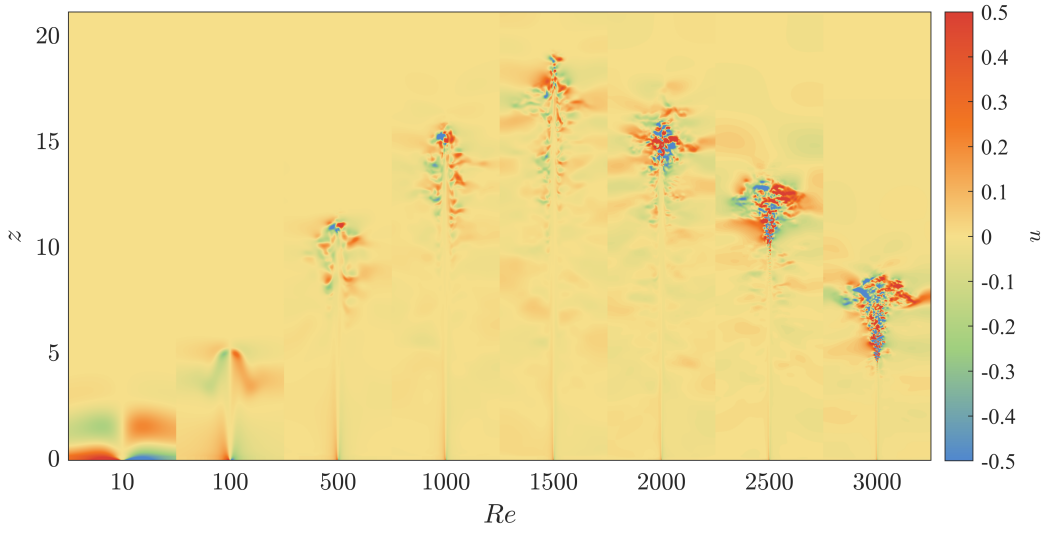

Figure 4.6: Showcase of rz-plane snapshots of radial velocity u taken from DNS of (4.15)–(4.19) at various Reynolds numbers, all with $Pr = 1$, and all at time $t \approx 30$, after the plume has reached its maximum rise height. In each case the similarity solution (2.25)–(2.28) has been added to the region $z < z_s$, defined in (4.28) for each Re.

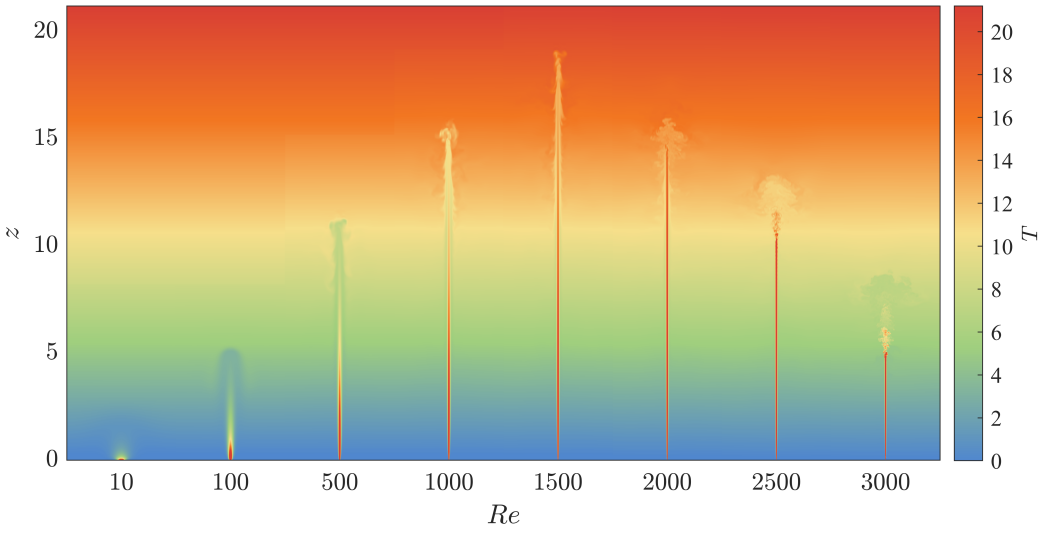

Figure 4.7: Showcase of rz-plane snapshots of temperature T taken from DNS of (4.15)–(4.19) at various Reynolds numbers, all with $Pr = 1$, and all at time $t \approx 30$, after the plume has reached its maximum rise height. In each case the similarity solution (2.25)–(2.28) has been added to the region $z < z_s$, defined in (4.28) for each Re.

The following sections consist of an investigation into the behaviour of plumes in a stratification using scaling analysis. The maximum rise height is investigated in section 4.4, followed by a comparison between the maximum rise height and height to instability in section 4.5, addressing research questions 7 and 8. The behaviour in the low and high Reynolds number regimes is then considered in section 4.6 and section 4.7 and compared to the results of the DNS.

4.4 Rise height

The maximum rise height of plumes modelled using DNS of (4.15)–(4.19) is determined by finding the maximum height at which the vertical velocity of the plume drops below 10% of its value at the displaced origin. A Python script iterates vertically through the azimuthally averaged data at every time step, looking only at the values of vertical velocity along the centreline until it reaches the 10% threshold. These values are then plotted on top of contour plots (like those in figure 4.5) to verify by eye that the correct height was found. The rise height is plotted against time in figure 4.8 for each Re. This value is

subsequently used to find the steady maximum rise height by averaging this height after the curve has been determined to have levelled off, for $t > 15$. In the upper plot of figure 4.8 values of rise height are plotted for $Re \leq 1500$, and in the lower plot for $Re > 1500$. This is to prevent overlapping curves from obscuring the data. The neutral buoyancy level (NBL) of plumes modelled using DNS of (4.15)–(4.19) is determined by calculating the buoyancy flux (4.10) at each height in the domain and finding the height at which it becomes zero.

The values determined by averaging the rise heights, and the time period over which they are averaged, are denoted in figure 4.8 by solid black lines. The values of rise height (white dots) and NBL (black dots) are then plotted in figure 4.9 on log-scale axes of Reynolds number and rise height. The rise height increases for $Re < 1500$, and attains a global maximum at $Re \approx 1500$, after which it begins to decrease. Interestingly, the NBL follows a similar trend but attains a global maximum at $Re \approx 2000$. This description goes part of the way to answering research question 7. The results in the low-Re regime indicate a power law trend. Predictions for the asymptotes of both low and high Reynolds number have been included on this plot, and are developed and discussed in the subsequent sections.

4.5 Comparison of rise height with height to instability

For laminar plumes, the height to instability z_* can clearly be seen to occur higher than the neutral buoyancy level (NBL), as illustrated by the DNS in figures 4.5 to 4.7 for $Re \leq 100$ as the instability does not occur before the plume reaches its NBL. For plumes with $100 < Re \leq 1500$, the plume appears to undergo some form of instability but this would appear to be due to the effect of the stratification. As $Re > 1500$, it is evident from figures 4.5 to 4.7 that the location of the height to instability z_* occurs lower than the NBL, evidenced by the turbulent plume regime occurring in the region beneath the NBL of each plume.

In figure 4.10, the dimensionless plume rise height versus Reynolds number is plotted (as in figure 4.9, but this time on linear axes). Included

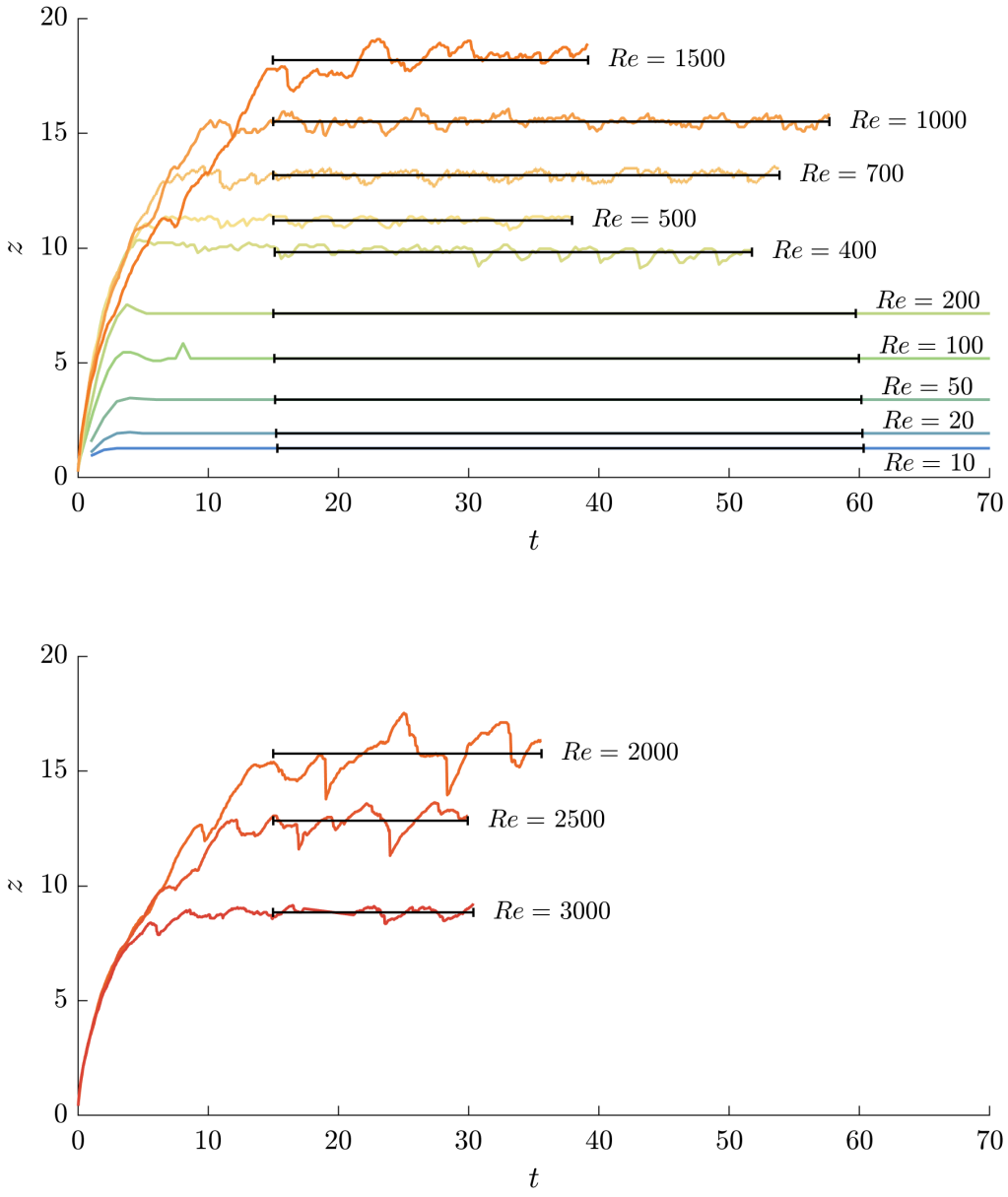

Figure 4.8: Dimensionless plume rise height versus simulation time for DNS of (4.15)–(4.19) for Reynolds numbers $Re \leq 1500$ in the top plot and $Re > 1500$ in the bottom plot. Solid black lines represent the time window over which each simulation has been averaged and the average value. Each curve is labelled with its Reynolds number on the right. There is a monotonic increase in rise height for simulations with $Re \leq 1500$, and a subsequent decrease thereafter. As Reynolds number increases above $Re = 200$ the fluctuations in maximum rise height become more evident, illustrating the introduction of turbulent behaviour.

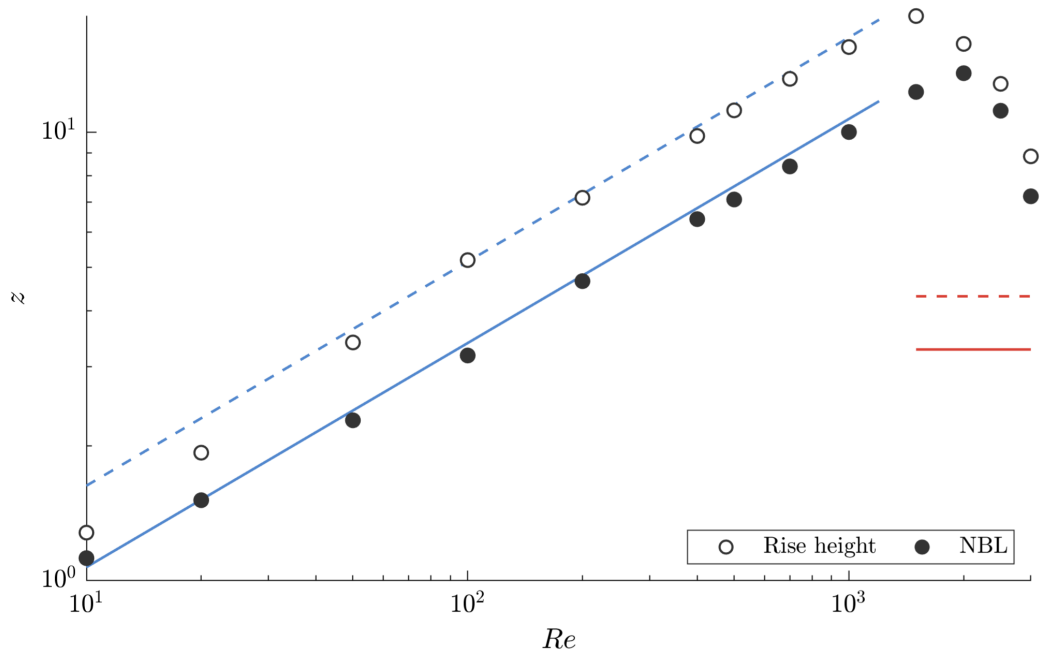

Figure 4.9: Dimensionless plume rise height versus Reynolds number for $Re \in [10, 3000]$, determined from DNS of (4.15)–(4.19). The increase in rise height and neutral buoyancy level (NBL), and subsequent decrease, for simulations across the full range of Reynolds numbers, first illustrated in figure 4.8, is more evident here. A global maximum rise height is attained at $Re \approx 1500$, after which the rise height begins to decrease. Interestingly, a global maximum NBL is attained at $Re \approx 2000$. Lines represent fitted curves, predicting the location of intermediate points. The blue dashed and solid line (on the left) indicate the laminar asymptote for rise height and NBL, calculated using the numerical solution to (4.36), given by $0.52\,Re^{1/2}$ and $0.34\,Re^{1/2}$, respectively. The red dashed and solid line (on the right) indicate the turbulent asymptote for rise height and NBL, given by the solution of the Morton et al. (1956) model, at a height of 4.32 and 3.28, respectively.

on this plot, however, is the scaled height to instability z_* predicted by the unstratified laminar similarity solution (4.25) (thin black dashed curve), and the height to instability predicted by the solution the DNS of (4.15)–(4.19) (crosses). The heights are only plotted for the DNS if they fall below the NBL and are determined using the same process as for the DNS of plumes in an unstratified environment, by the height at which the centreline vertical velocity of the plume drops below $w_0/2$ (see section 2.3.2 for more detail).

There is a clear discrepancy between the height to instability predicted by the unstratified laminar similarity solution and the DNS. The values from the DNS are much higher than those for the unstratified laminar similarity solution, indicating that the stratification delays the onset of instability

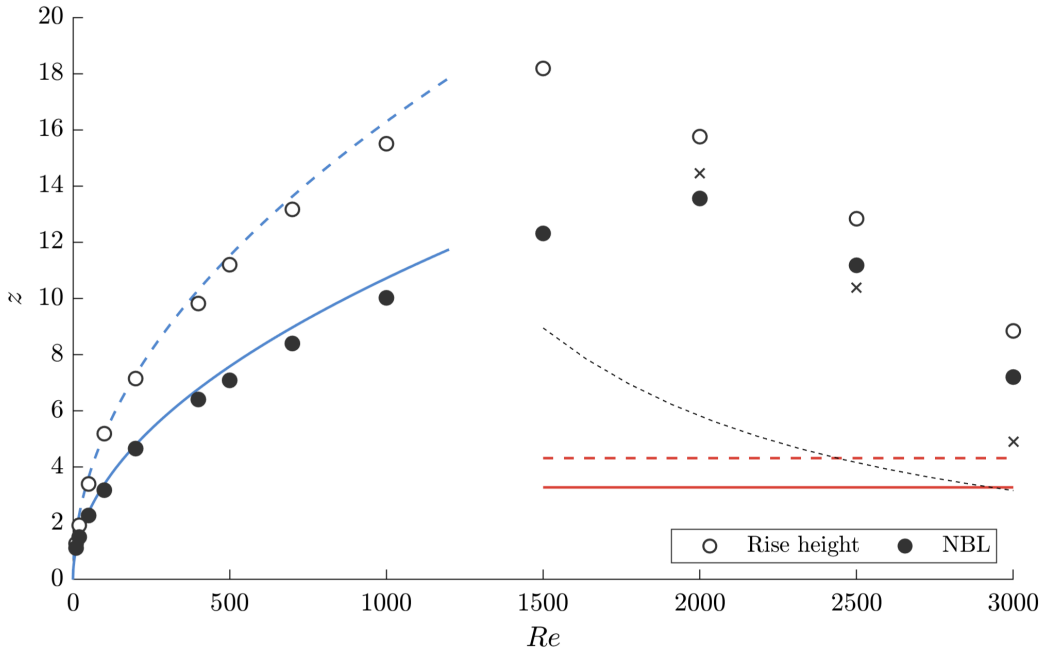

Figure 4.10: Dimensionless plume rise height and NBL versus Reynolds number for $Re \in [10, 3000]$, determined from DNS of (4.15)–(4.19), compared to the scaled height to instability z_* (4.25) predicted by the unstratified laminar similarity solution (2.25)–(2.28) (illustrated by the black dashed curve) and the height to instability extracted from the DNS for values for which it exists. The blue and red curves represent predictions for the laminar and turbulent regimes, respectively, as discussed for figure 4.9. There is a clear discrepancy between the height to instability predicted by the unstratified similarity solution and the DNS, suggesting that the stratification has a big impact on the height to instability.

in the laminar plume regime. It would appear, however, that the height to instability from the DNS is approaching the similarity prediction as the Re increases and further simulations at higher Reynolds numbers would verify this.

The work in this section addresses the relationship between the maximum rise height and height to instability for a plume in a stratification, namely research question 8. The height to instability z_* lies above the NBL for plumes with $Re \leq 1500$ and is lower beneath for $Re > 1500$. It is interesting to note that the unstratified laminar similarity solution cannot be used to predict the height to instability in a stratification.

4.6 Laminar theory

A theory of maximum rise height for a plume in a stratification is developed for the first time using the laminar similarity solution for plumes in an unstratified environment (2.25)–(2.28) (Zeldovich, 1937; Yih, 1951) and adapting it by introducing a stratification. The resulting equations can be solved using a finite differencing method to predict the maximum rise height for laminar plumes in a stratification.

In the low Reynolds number regime, the flow can be approximated as a boundary layer in the slender stem regime prior to the lateral spreading regime at the neutral buoyancy level (NBL). The boundary layer assumptions are applied to the system (4.15)–(4.19), like in section 1.1.1, to simplify the governing equations and result in the system

$$u\frac{\partial w}{\partial r} + w\frac{\partial w}{\partial z} = \frac{1}{Re}\left(\frac{1}{r}\frac{\partial}{\partial r}\left(r\frac{\partial w}{\partial r}\right)\right) + \vartheta, \tag{4.29a}$$

$$\frac{1}{r}\frac{\partial (ru)}{\partial r} + \frac{\partial w}{\partial z} = 0, \tag{4.29b}$$

$$u\frac{\partial \vartheta}{\partial r} + w\frac{\partial \vartheta}{\partial z} = \frac{1}{Pe}\left(\frac{1}{r}\frac{\partial}{\partial r}\left(r\frac{\partial \vartheta}{\partial r}\right)\right) - w. \tag{4.29c}$$

At the centre of plume, the same symmetry conditions (1.18) are

$$\frac{\partial w}{\partial r} = 0, \qquad \frac{\partial T}{\partial r} = 0, \qquad u = 0, \qquad \text{at } r = 0. \tag{4.30}$$

The far-field conditions (1.19) are

$$w \to 0, \qquad T \to 0, \qquad \text{as } r, z \to \infty, \tag{4.31}$$

and the buoyancy flux condition at the point source (1.20) is

$$2\pi \int_0^\infty r(\vartheta + z)w \, \mathrm{d}r = 1. \tag{4.32}$$

4.6.1 Scaling Analysis

A dependence of the low-Re rise height on Re can be established by performing a scaling analysis to determine the relationships between terms in the governing

equations (4.29). By comparing the the advective, diffusive, and forcing terms in the momentum equation (4.29a), the advective and forcing terms in the temperature difference equation (4.29c), and the terms in the source condition (4.32), the following scaling relationships are found

$$\frac{w^2}{z} \sim \frac{1}{Re}\frac{w}{r^2} \sim \vartheta, \qquad \frac{w\vartheta}{z} \sim w, \qquad r^2\vartheta w \sim 1. \tag{4.33}$$

By rearranging these scaling relationships, scales for height, radius, velocity, and temperature difference are found to be

$$z \sim Re^{1/2}, \qquad r \sim Re^{-1/2}, \qquad w \sim Re^{1/2}, \qquad \vartheta \sim Re^{1/2}, \tag{4.34}$$

illustrating that in the low-Re regime, the vertical height scale, and hence the maximum rise height, admits a scaling given by $z \sim Re^{1/2}$. Using the scales from the equation for conservation of mass (4.29b), $u/r \sim w/z$, the scaling for horizontal velocity is found to be $u \sim Re^{-1/2}$. Using the scales in (4.34), a new set of variables, denoted by hats, are formed

$$\begin{aligned} z =& Re^{1/2}\hat{z}, \quad r = Re^{-1/2}\hat{z}, \quad w = Re^{1/2}\hat{w}, \\ \vartheta =& Re^{1/2}\hat{\vartheta}, \quad u = Re^{-1/2}\hat{u}, \end{aligned} \tag{4.35}$$

and substituting into the boundary layer equations (4.29) reveals a system dependent only on the Prandtl number Pr. As a result, the equations describing the laminar regime, for a given Pr, are given by

$$\hat{u}\frac{\partial \hat{w}}{\partial \hat{r}} + \hat{w}\frac{\partial \hat{w}}{\partial \hat{z}} = \frac{1}{\hat{r}}\frac{\partial}{\partial \hat{r}}\left(\hat{r}\frac{\partial \hat{w}}{\partial \hat{r}}\right) + \hat{\vartheta}, \tag{4.36a}$$

$$\frac{\partial(\hat{r}\hat{u})}{\partial \hat{r}} + \frac{\partial \hat{r}\hat{w}}{\partial \hat{z}} = 0, \tag{4.36b}$$

$$\hat{u}\frac{\partial \hat{\vartheta}}{\partial \hat{r}} + \hat{w}\frac{\partial \hat{\vartheta}}{\partial \hat{z}} = \frac{1}{Pr}\left(\frac{1}{\hat{r}}\frac{\partial}{\partial \hat{r}}\left(\hat{r}\frac{\partial \hat{\vartheta}}{\partial \hat{r}}\right)\right) - \hat{w}, \tag{4.36c}$$

with the same boundary, far-field and source conditions as (4.30), (4.31), and (4.32), respectively. All the plumes considered in this chapter have $Pr = 1$, meaning that a solution to these equations for $Pr = 1$ can be scaled using (4.35) to inform the solution at any Re in the laminar regime.

4.6.2 Solving the laminar plume equations with a finite-differencing method

The height scale in (4.34) illustrates that the maximum rise height of a laminar plumes increases as $Re^{1/2}$. This could be fitted to the data from the DNS of (4.15)–(4.19) in figure 4.9, however, in this section the boundary layer equations (4.36) can be solved directly to determine the prefactor.

The boundary layer equations (4.36) with $Pr = 1$ are hence solved using a finite difference marching procedure, treating the vertical coordinate like progressing through time. A theta-scheme is employed to improve stability. Solver details and a description of finite differencing are included in appendix B. The finite differencing solver was verified by solving similar equations using MATLAB's PDEPE solver (Skeel & Berzins, 1990).

Solving (4.36) and terminating as the momentum flux becomes zero results in the solution shown in figure 4.11, where the solution is terminated at $z \approx 0.52$ to two significant figures. Qualitatively similar results are obtained to those from the solutions to the DNS of (4.15)–(4.19) with $Re = 10$. The maximum rise height is found to be $\sim 0.52\,Re^{1/2}$ for values of Re in the laminar plume regime. The neutral buoyancy level (NBL) is determined by calculating the buoyancy flux (4.10) at each height in the domain and finding the height at which it becomes zero, which is $z \approx 0.34$ to two significant figures, and using the height scaling in (4.35) the NBL is found to be $\sim 0.34\,Re^{1/2}$ for values of Re in the laminar plume regime.

Plotting this equation for the maximum rise height of plumes in the laminar regime, $z \approx 0.52\,Re^{1/2}$, in figure 4.9 as a blue dashed curve illustrates an excellent fit for $Re \in [50, 1000]$, thereby addressing research question 7 by developing a theory for maximum rise height of laminar plumes in a stratification. For $Re < 50$, the values of rise height are over-predicted by the laminar theory. Similarly, plotting the equation for the NBL in the laminar regime $z \approx 0.34\,Re^{1/2}$ in figure 4.9 as a blue solid curve, also illustrating a good fit for $Re \in [50, 1000]$. In chapters 2 and 3 the plume was in an unstratified environment and hence the assumptions made in the boundary layer regime became stronger as height increased due to the parabolic nature of the flow scalings. With the introduction of a stratification, however, the boundary layer assumptions may not apply, and in the (very) low-Re regime the height over

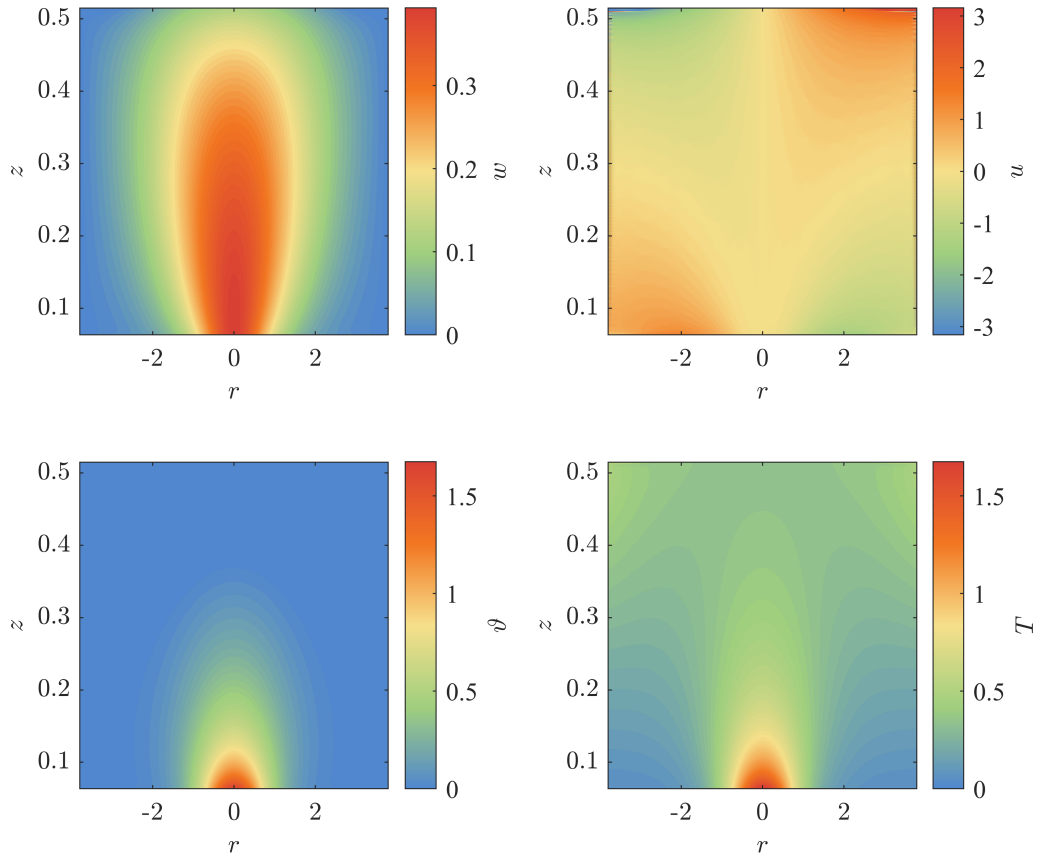

Figure 4.11: Results from the numerical solution to (4.36), solved using a finite differencing scheme described in appendix B. The neutral buoyancy level is found as the buoyancy flux (4.20) becomes zero at $z \approx 0.34$ to two significant figures and the simulation is terminated when the momentum flux (4.21) becomes zero, hence ending just as the plume reaches its maximum rise height at $z \approx 0.52$ to two significant figures.

which the assumptions apply could be minimal or non-existent. It is hence suggested that for $Re < 50$ the boundary layer assumptions may not hold and hence the prediction is inaccurate over this range.

4.7 Turbulent theory

As described in section 1.1.2, Morton et al. (1956) developed a model to describe an axisymmetric, turbulent plume rising from a point source using volume Q, momentum M, and buoyancy F fluxes. After non-dimensionalising

the system of equations (1.37) using (4.14) one finds the system

$$\frac{\mathrm{d}Q}{\mathrm{d}z} = 2\alpha M^{1/2}, \tag{4.37a}$$

$$\frac{\mathrm{d}M}{\mathrm{d}z} = \frac{FQ}{M}, \tag{4.37b}$$

$$\frac{\mathrm{d}F}{\mathrm{d}z} = -Q, \tag{4.37c}$$

with $Q_0 = 0$, $M_0 = 0$, and $F_0 = 1$. The value of the entrainment coefficient is chosen to be $\alpha = 0.1$, as is suggested by a multitude of studies in the literature, a number of which are detailed in Carazzo et al. (2006). Solving (4.37) and terminating when momentum flux M becomes zero results in the dimensionless rise height for a plume emanating from a point source in a stratification to be a constant, namely 4.32. Similarly, the height at which the buoyancy flux becomes zeros results in the dimensionless neutral buoyancy level (NBL) at 3.28.

The fact that the NBL and the maximum rise height become constant as $Re \to \infty$ can also be predicted using a scaling analysis. The value can be found by comparing to values found from DNS of (4.15)–(4.19) at high Re. This process involves comparing the scalings between advective and buoyancy terms in the momentum equation (4.15a), the advective and forcing terms in the temperature difference equation (4.15c), the terms in the advective buoyancy flux (4.20), and using that in turbulent flow $r \sim z$ due to turbulent eddies with order-unity aspect ratio. This results in the scaling relationships $w^2 \sim \vartheta z$, $\vartheta \sim z$, $r^2 \vartheta w \sim 1$, and $r \sim z$. Resolving these scales results in

$$z \sim r \sim w \sim \vartheta \sim 1, \tag{4.38}$$

meaning that in the stratified plume regime, the height, radius, vertical velocity, and temperature difference are all of order 1 in the dimensionless system (4.15)–(4.19). This suggests that as the Reynolds number $Re \to \infty$ the NBL and the maximum rise height tend to constant values, agreeing with the prediction of Morton et al. (1956).

The results from the DNS of (4.15)–(4.19) for values of $Re \geq 1500$ show that the NBL and the maximum rise height are decreasing towards the value of 3.28 and 4.32, respectively, predicted by the model of Morton et al. (1956). Research question 7 is addressed by confirming the result of Morton

et al. (1956) using scaling analysis, with further simulations at higher Reynolds numbers required to independently verify the values of 3.28 and 4.32. The results in figure 4.9 indicate a trend towards the asymptotes for $Re > 3000$. Performing DNS at $Re > 3000$ could result in predictions for the NBL and maximum rise height independent of the entrainment coefficient (Morton et al., 1956).

Further simulations to determine this trend towards constant values of NBL and maximum rise height would also enable the answer to research question 9. Say, for example, that the NBL and the maximum rise height level off at a value of Re_*. Then, to determine the NBL and the rise height in future simulations of plumes in a stratification, for any application, such as a volcanic eruption with $Re = 10^6$, no further information about the NBL and the maximum rise height could be garnered from an increase in Reynolds number beyond Re_*, and hence the simulation should be run at Re_* to conserve computational resources.

4.8 Conclusions

In this chapter, a scaling analysis and direct numerical simulations (DNS) of the governing equations (4.15)–(4.19) of a plume generated by a point source of heat in a stratification were undertaken. Using scaling, the full system was found to be dependent on two dimensionless parameters, the Reynolds number and the Péclet number, formed by grouping the initial buoyancy flux F_0, stratification frequency N, and kinematic viscosity ν or thermal diffusivity κ (Fabregat Tomàs et al., 2016; Rooney & Devenish, 2014) in the following way

$$Re = \left(\frac{F_0}{N\nu^2}\right)^{1/2}, \qquad Pe = \left(\frac{F_0}{N\kappa^2}\right)^{1/2}. \tag{4.39}$$

DNS of plumes arising from a point source in a stratification were performed and the rise height was found to exhibit non-monotonic behaviour with increasing Re, with a global maximum at $Re \approx 1500$, thereby addressing research question 7.

The relationship between the maximum rise height and height to in-

stability for a plume in a stratification was described in section 4.5, addressing research question 8. The height to instability z_* was shown to lie above the maximum rise height for plumes with $Re \leq 1500$ and below for $Re > 1500$. An interesting comparison between the prediction of height to instability from the unstratified laminar similarity solution (2.25)–(2.28) and the DNS revealed that the laminar similarity solution cannot be used to predict the height to instability in a stratification.

Using boundary layer assumptions and scaling arguments, low-Re plumes in a stratification were shown to admit a universal solution for a given Prandtl number up to a scaling by Reynolds number. This solution was calculated using finite differencing and a neutral buoyancy level (NBL) of $z \approx 0.34$ and a maximum rise height of $z \approx 0.52$ were found, both to two significant figures. Using that height scales like $Re^{1/2}$ in the low-Re regime, the curves $z \approx 0.34\, Re^{1/2}$ and $z \approx 0.52\, Re^{1/2}$ were compared to DNS of plumes in a stratification and excellent agreements between the simple scaling theory and DNS for $50 < Re < 1000$ were found, further addressing research question 7 for laminar plumes. There was some discrepancy in NBL and rise height for $Re < 50$, however this is suggested to be due to a failure of the boundary layer assumptions when the aspect ratio of the flow is close to one. The NBL and rise height of a laminar plume can be multiplied with the dimensional length scale in (4.13) to find that the dimensional NBL and rise height for a plume for $50 \lesssim Re \lesssim 1000$ are

$$NBL_L \approx 0.34 \left(F_0 N^{-3}\right)^{1/4} Re^{1/2}, \tag{4.40}$$

$$H_L \approx 0.52 \left(F_0 N^{-3}\right)^{1/4} Re^{1/2}. \tag{4.41}$$

Using scaling arguments, the NBL and maximum rise height of a turbulent plume were both found to be a constant, with the theory of Morton et al. (1956) suggesting a value of 3.28 and 4.32, respectively. The DNS at higher Reynolds numbers are approaching these values, however further simulations at higher Reynolds numbers are required for verification.

4.8.1 Further work and limitations

The DNS for $Re \in [50, 1000]$ were verified by matching the low-Re theory closely, and the trends captured for $Re \geq 1500$ behave as expected. A mesh sensitivity study on the meshes used for the high-Re simulations will be performed for further work, as well as simulations at higher Reynolds numbers to attempt to capture the turbulent asymptote.

Further simulations of plumes in a stratification at Reynolds numbers $Re > 3000$, aiding in the determination of the trends in NBL and maximum rise height towards constant values, would also address research question 9. It would do this by finding a value of the Reynolds number for which further increases induce no significant change in the NBL and the maximum rise height.

Chapter 5

Implications of laminar, turbulent, and hybrid plume theory to aerosol transport

Contents

The field of natural ventilation has been of particular interest in recent years, with a focus on air quality in offices, classrooms, and hospital wards (Tang et al., 2006). Previous studies that have investigated particle transport in plumes have often focused on particle fallout from the stem and neutrally buoyant gravity current stage of a turbulent plume (Sparks et al., 1991; Johnson et al., 2015; Sutherland & Hong, 2016). Few studies, however, have investigated the transport of particles in laminar and hybrid laminar-turbulent plumes (pertaining to research question 10).

The theory of height to instability, discussed in chapters 2 and 3, can be applied to the transport of heat and aerosols within rooms and indoor spaces. In the laminar region before instability, heat (and any particles that may be in the flow) is transported much faster than after instability, as shown by the rapid decrease in vertical velocity as a plume transitions from laminar to turbulent flow in figure 2.13. In this chapter, I will show that this drop

in velocity can have consequences in the field of natural ventilation. If, for example, the height to instability of a plume generated by a source of heat in a room is higher than the height of the ceiling, the vast majority of material in that flow will be transported rapidly to the ceiling in the laminar regime, as opposed to the slower moving turbulent regime, before being dispersed in an axisymmetric gravity current along the ceiling.

Examples of heat sources which have the potential to sustain a low source of heat conducive to forming a laminar regime include a human in a hospital bed, a candle, a computer, or other electrical equipment. The theoretical results in chapters 2 and 3 provide a basis both for assessing the most relevant regime for a given heat flux, as well for determining the rise rate in situations where the flow undergoes a transition from laminar to turbulent flow.

In section 5.1, values of height to instability are calculated for typical household objects. In section 5.2, laminar, turbulent, and hybrid laminar-turbulent plume models for the time taken to reach instability are developed. By applying this hybrid model to particle transport, an answer to research question 10 is provided. Finally, conclusions are drawn in section 5.3.

In the non-dimensionalisation in section 2.2, a hat notation was used, and subsequently dropped to improve readability of the equations when everything was in dimensionless form. In this chapter, hat notation is re-instated for dimensionless variables, leaving dimensional variables without hats.

5.1 Characteristic values

To explore the implications of the height to instability on indoor ventilation, the dimensional initial buoyancy flux F_0 is calculated for a given heat flux q using

$$F_0 = \frac{\beta g}{\rho_0 c_p} q, \tag{5.1}$$

where g is the acceleration due to gravity, β is the coefficient of thermal expansion, ρ_0 is the density, c_p is specific heat capacity, and q is heat flux (measured in watts) (Gill, 1982).

	q (W)	F_0 (10^{-2} m^4 s^{-3})	z_* (cm)
Toaster	1200	3	20
Human	100	0.3	80
Candle	80	0.2	90
LED TV	50	0.1	110
LED lamp	10	0.03	250

Table 5.1: Heat flux q, initial buoyancy flux F_0, and height to instability z_* for a number of household items. Calculated using (5.2).

The dimensionless height to instability was calculated for a number of Prandtl numbers in chapters 2 and 3 using direct numerical simulations (DNS) of (3.2)–(3.5). The Prandtl number of air at room temperature is $Pr \approx 0.7$. However, complete results, including the value of the virtual origin for the turbulent regime, are only available for $Pr = 1.0$. Ideally, the interpolation formula (3.26) would be used to find an approximate value for the dimensionless height to instability, and similarly for the virtual origin $\hat{z}_0$ (used in section 5.2). However, for the work in this chapter, the results from chapter 2 are used to illustrate the theory and the value of dimensionless height to instability for $Pr = 1.0$ is taken to be $\hat{z}_* = 3.9 \times 10^5$.

By combining the length scale in (2.15) and the dimensionless height to instability $\hat{z}_*$, the dimensional height to instability can be determined using

$$z_* = \hat{z}_* \left(\frac{\kappa^3}{F_0} \right)^{1/2} . \tag{5.2}$$

The following material and physical properties are used for the following calculations: $g = 9.8\,\mathrm{m\,s^{-2}}$, $\rho_0 = 1.2\,\mathrm{kg\,m^{-3}}$, $\beta = 3.4 \times 10^{-3}\,\mathrm{K^{-1}}$, $c_p = 1.01 \times 10^3\,\mathrm{m^2\,K^{-1}\,s^{-2}}$, and $\kappa = 2.2 \times 10^{-5}\,\mathrm{m^2\,s^{-1}}$. For $Pr = 1.0$, for which the prediction for $\hat{z}_* \approx 3.9 \times 10^5$, the height to instability is calculated and values of heat flux typical for a variety of household objects (table 5.1).

Typical values of the height to instability are of the order of 0.1 - 1 m, resulting in the location of instability for many household objects being within the height of a room. This relationship is also plotted in figure 5.1, for values of buoyancy flux up to that of a typical volcanic eruption with $F_0 = 5.4 \times 10^4\,\mathrm{m^4\,s^{-3}}$ (Pyle, 1995). It is interesting to note that for values of $F_0 > 1\,\mathrm{m^4\,s^{-3}}$, the height to instability is small, from $z_* = 4\,\mathrm{cm}$ for $F_0 = 1\,\mathrm{m^4\,s^{-3}}$ to the virtually negligible $z_* = 0.2\,\mathrm{mm}$ for $F_0 = 5.4 \times 10^4\,\mathrm{m^4\,s^{-3}}$. In the next section,

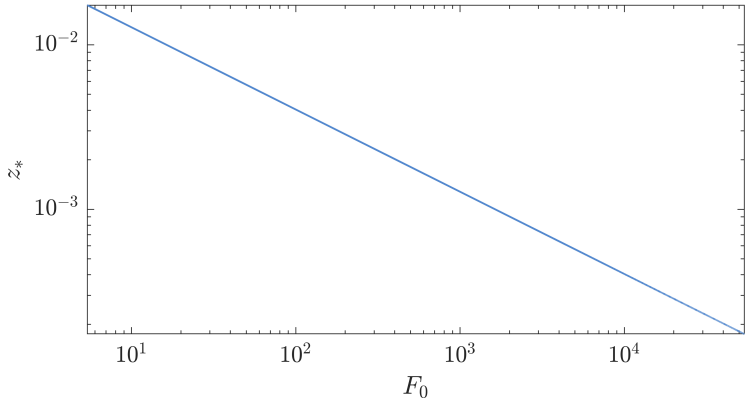

Figure 5.1: Height to instability z_* for a range of initial buoyancy fluxes and $\kappa = 2.2 \times 10^{-5}\,\mathrm{m^2\,s^{-1}}$, given by (5.2). The value of z_* decreases as $F_0^{-1/2}$ and is virtually negligible for large F_0.

theoretical predictions for the time taken for a plume to reach the ceiling of a standard room are developed.

5.2 Vertical transport of aerosols

In the previous section, the height to instability was calculated for a range of buoyancy fluxes. This calculation is now extended to consider the time taken for a particulate in a plume to reach the ceiling, where it would subsequently be transported laterally in a gravity current and dispersed into the room. The vertical transport of aerosols begins by considering the two end-member cases of fully laminar and fully turbulent flows. This is followed up by combining the two in a hybrid laminar-turbulent theory of aerosol transport.

5.2.1 Laminar prediction

The time to reach the ceiling at a height H is calculated by making the initial assumption that the full plume is laminar and ignoring any instability effects. The location of a particle in the centre of the plume $z(t)$ at a given time t is described by

$$\frac{\mathrm{d}z}{\mathrm{d}t} = w_0 = \hat{w}_0 \left(\frac{F_0}{\kappa}\right)^{1/2}, \tag{5.3}$$

where w_0 is the constant dimensional velocity at the plume centre predicted by the laminar similarity solution (3.9)–(3.12), and $\hat{w}_0$ is the dimensionless prefactor $\hat{w}_0 \approx 0.40$ for $Pr = 1.0$. Integrating (5.3), the height $z = w_0 t$ is obtained and, on rearranging for t, the prediction for the minimum time to reach the ceiling is found to be

$$t_c = \frac{H}{w_0} = \hat{w}_0^{-1} \left(\frac{\kappa}{F_0} \right)^{1/2} H, \tag{5.4}$$

for ceiling height H. The prediction for the time of a particle to reach the ceiling t_c above is plotted as a function of source strength F_0 in figure 5.2 (as a black dot-dashed curve), showing that the time to reach the ceiling for a fully laminar plume decreases as $F_0^{-1/2}$. This is an intuitive result, as the initial buoyancy flux grows larger, both the temperature and velocity of a plume will increase, and hence the time taken to transport material will decrease.

5.2.2 Turbulent prediction

In the alternative limit of a fully turbulent plume, the plume is assumed to be fully turbulent for the full height of a room. Similarly to the previous section, a differential equation for the velocity of the particle, using the solution to the turbulent similarity equations (2.25)–(2.28), is considered, while the assumption that the turbulent regime initiates at the source ($z_0 = 0$) must be made. In section 2.5 it was shown that vertical velocity is proportional to $z^{-1/3}$ (2.56). Therefore, the rise rate of the particle is given by

$$\frac{\mathrm{d}z}{\mathrm{d}t} = \phi_0 F_0^{1/3} z^{-1/3}, \tag{5.5}$$

where $\phi_0 \approx 3.3$ is the dimensionless prefactor from the turbulent similarity solution in (2.59) and it is assumed that the particle travels along the centreline of the plume. Integrating this equation subject to the constraint $z(0) = 0$ results in the position of the particle

$$z(t) = \left(\frac{4\phi_0}{3} F_0^{1/3} t \right)^{3/4}. \tag{5.6}$$

On setting $z(t_c) = H$, the time for the particle to reach the ceiling is given by

$$t_c = \frac{3}{4\phi_0} F_0^{-1/3} H^{4/3}. \tag{5.7}$$

The prediction for the time of a particle to reach the ceiling t_c in the turbulent plume regime is plotted as a function of source strength F_0 in figure 5.2 (as a red dashed curve) alongside the prediction for the laminar regime, showing that the time to reach the ceiling decreases as $F_0^{-1/2}$ for the laminar regime and as $F_0^{-1/3}$ for the turbulent regime. The time taken for a particle to reach the ceiling becomes quicker for the turbulent regime than the laminar regime for $F_0 \lesssim 5 \times 10^{-9}\,\mathrm{m}^4\,\mathrm{s}^{-3}$, which is a virtually negligible buoyancy flux for any relevant application of a heat source in a room. For typical values of initial buoyancy flux F_0, the time to reach the ceiling is approximately an order of magnitude greater for the fully turbulent plume compared with the fully laminar plume.

5.2.3 Hybrid laminar-turbulent prediction

Both (5.4) and (5.7) represent different end-member cases of particle transport in a fully laminar and fully turbulent plume. In general, a particle carried by a plume can experience both laminar and turbulent flow (given F_0 is large enough to produce a transition within the height of the room), and travel through the transition between the two. The hybrid laminar-turbulent description of a plume allows for a unifying, consistent bridge connecting these two limiting end-member situations, as well as the conditions under which the switch between them occurs. In that case, the velocity of a particle in the hybrid plume is given by a combination of (5.3) and (5.5), resulting in

$$\frac{\mathrm{d}z}{\mathrm{d}t} = \begin{cases} w_0, & \text{for } z < z_*, \\ \phi_0 F_0^{1/3} (z - z_0)^{-1/3}, & \text{for } z \geq z_*, \end{cases} \tag{5.8}$$

where z_0 is the location of the turbulent virtual origin given by

$$z_0 = \hat{z}_0 \left(\frac{\kappa^3}{F_0} \right)^{1/2}, \tag{5.9}$$

with $\hat{z}_0 = 2.9 \times 10^5$ and the height of instability is given by (5.2), with $\hat{z}_* \approx 3.9 \times 10^5$ for $Pr = 1.0$. For $z < z_*$ the velocity (5.8) is integrated up to z_*

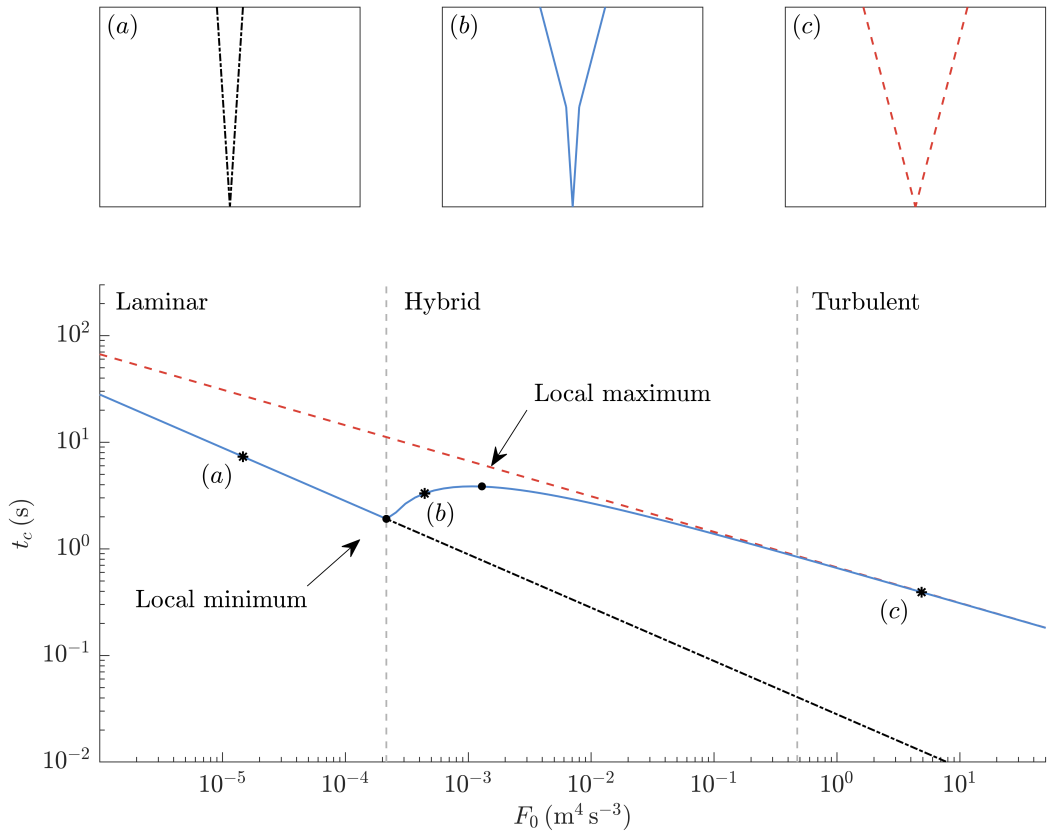

Figure 5.2: Time for a passive tracer (e.g. airborne pathogen) to reach a ceiling t_c of height $H = 2.4\,\mathrm{m}$ in a unified (5.11) plume for a range of initial buoyancy fluxes F_0. The fully laminar (5.4) case (black, dot-dashed) and the fully turbulent (5.7) case (red, dashed) show the approach of the unified theory to each end case. Schematics illustrating the shape of the plume for each regime are included above for laminar (a), unified (b), and turbulent (c) plumes. Filled dots represent the local turning points at the laminar to unified transition and at the maximum time for a tracer to reach the ceiling in the unified regime.

as in the laminar case (5.4). For $z \geq z_*$ the velocity (5.8) is integrated using separation of variables, the constant of integration is evaluated by applying continuity on z at $t = t_*$ to obtain the location of a particle

$$z(t) = \begin{cases} w_0 t, & \text{for } t < t_*, \\ z_0 + \left((z^* - z_0)^{4/3} + \dfrac{4\phi_0}{3} F_0^{1/3} (t - t^*) \right)^{3/4}, & \text{for } t \geq t_*, \end{cases} \tag{5.10}$$

where $t_* = z_*/w_0$ is the time at which the transition to instability occurs. Thus, on setting $z = H$, the general expression for the time to reach the

ceiling is given by

$$t_c = \begin{cases} \dfrac{H}{w_0}, & \text{for } H < z_*, \\ t_* + \dfrac{3F_0^{-1/3}}{4\phi_0}\left((H - z_0)^{4/3} - (z_* - z_0)^{4/3}\right), & \text{for } H > z_*. \end{cases} \tag{5.11}$$

Assuming a typical ceiling height of $H = 2.4\,\mathrm{m}$, the time taken for a particle to reach the ceiling t_c (blue solid curve), and the laminar (5.4) and turbulent (5.7) edge cases, are plotted in figure 5.2 for a range of initial buoyancy fluxes $F_0 \in [10^{-6}, 10^{2}]\,\mathrm{m^4\ s^{-3}}$. For values of $F_0 \lesssim 2.1 \times 10^{-4}\,\mathrm{m^4\ s^{-3}}$, the time to reach the ceiling is dependent purely on the laminar regime, as the time to instability is greater than the time taken to reach the ceiling. For the turbulent regime, for values of $F_0 \gtrsim 0.48\,\mathrm{m^4\ s^{-3}}$, the tranisiton to instability occurs almost at the point source of heat, meaning the plume is fully turbulent effectively for the fully height of the room.

As the height to instability decreases below the height of the ceiling, the time to reach the ceiling sharply increases due to the decay in vertical velocity in the turbulent plume. Remarkably, this results in two local turning points. There is a local minimum at $F_0 = 2.1 \times 10^{-4}\,\mathrm{m^4\ s^{-3}}$ where the turbulent regime is first realised in the flow. As the buoyancy flux increases, the time to reach the ceiling increases as the slower moving turbulent regime increases in size. There is a local maximum at $F_0 = 1.3 \times 10^{-3}\,\mathrm{m^4\ s^{-3}}$ beyond which the increasing buoyancy flux results in a larger vertical velocity despite the turbulence, and the time to reach the ceiling begins to decrease again. The model in (5.11) predicts that for an aerosol being transported by a hybrid laminar-turbulent plume in an unstratified environment, the time taken to reach the ceiling varies non-monotonically with initial buoyancy flux, thereby providing an answer to research question 10.

An important caveat is that the above theory assumes that a plume starts from a point source and in reality, all sources of heat will have a finite area. This could result in either an increase or a decrease to the height of instability, dependent on whether the plume is lazy or forced (Morton, 1959; Hunt & Kaye, 2005). Another assumption is a still environment. Draughts or other air disturbances would potentially induce an earlier transition to turbulence (Linden, 1999). It was also assumed that a particle in a turbulent plume takes the fastest velocity at the centreline. Reducing the velocity of a particle

in this regime, however, would increase the time taken for a particle to reach the ceiling height and therefore increase the sharpness of the non-monotonic region. Despite these assumptions, these calculations can still be used to make reasonable predictions of height to instability in an indoor environment.

5.3 Conclusions

In this chapter, an application of plume theory to the field of natural ventilation was investigated. It has been shown that the height to instability z^*, calculated using direct numerical simulations (DNS) of a plume emanating from a point source in an unstratified environment (2.17)–(2.20), plays a role in the transport and dispersal of aerosols within in a room. Using scaling, the height to instability has been shown to be of a height that is within a typical room, illustrating that both laminar and turbulent plume flow is likely to occur for plumes generated by everyday objects.

Further to the location of instability, the time taken for a weightless particle to reach the ceiling was calculated using laminar (2.29) (Zeldovich, 1937; Yih, 1951) and turbulent (2.57) (Zeldovich, 1937; Schmidt, 1941) similarity theory. A remarkable non-monotonic relationship between initial buoyancy flux and particle transport in plumes was discovered using a hybrid theory of laminar and turbulent plumes, thereby addressing research question 10. Two turning points in the relationship were uncovered, with the first occurring when the height to instability becomes less than the ceiling height, and the second when the increasing buoyancy flux induces a larger vertical velocity in the turbulent regime, both are illustrated in figure 5.2. This work also highlights the importance of the laminar regime in particle transport, predicting that a turbulent plume requires an initial buoyancy flux over two orders of magnitude larger than a laminar plume to transport a particle to the ceiling in the same amount of time.

5.3.1 Further work

Further work on this could involve performing DNS of the governing equations (3.2)–(3.5) at $Pr = 0.7$ to ensure that more accurate values of $\hat{z}_*$ and $\hat{z}_0$ are

found. Currently, the modelling assumes that transported aerosols take on the highest velocity in the plume, namely that at the plume centre, whereas in reality they would not travel this fast, especially in the turbulent regime. Some would likely settle out of the plume stem and others would take longer to reach the ceiling. The modelling of aerosol transport in plumes could be improved by taking this into account, as well as considering other aspects such as introducing areal sources to the model or advection due to air currents.

Chapter 6

Conclusions

Contents

The main aim of the work in this thesis was to investigate the fundamental behaviour and structure of plumes emanating from a point source. Previous studies have often explored simplified models or specifics. The novelty in this work has broadly been to apply the relatively recent development of direct numerical simulations (DNS) to fundamental plume behaviour.

In chapter 2, I performed DNS of the incompressible Boussinesq equations (2.17)–(2.20) of a plume generated at a point source of heat in an unstratified environment for the case of $Pr = 1$ and found a value for the dimensionless height to instability $\hat{z}_*$. I also described the full structure of a plume, including the turbulent regime and its dimensionless virtual origin $\hat{z}_0$. Using the length scale $L = (\kappa^3/F_0)^{1/2}$ (2.15), the dimensional height to instability z_* for a plume rising from a point source of heat in an unstratified environment with any initial buoyancy flux F_0 and thermal diffusivity κ for $Pr = 1$, thereby addressing research question 1, is given by

$$z_* = \hat{z}_* \left(\frac{\kappa^3}{F_0}\right)^{1/2}, \tag{6.1}$$

for dimensionless height to instability $\hat{z}_* \approx 5.1 \times 10^5$ (as determined by the DNS), in a domain with radius $r_e = 1.6 \times 10^5 \, (\kappa^3/F_0)^{1/2}$ and height $z_e = 8 \times 10^5 \, (\kappa^3/F_0)^{1/2}$, subject to the anticipated error bound described in the mesh sensitivity analysis in section 2.3.2.

Secondly, I described the full structure and location of a plume emanating from a point source for $Pr = 1$, addressing research question 2. This was achieved by describing the transition from a point source of heat to a laminar plume with the laminar similarity solution (1.30)–(1.33) (Zeldovich, 1937; Yih,

1951), subsequently finding the value for the dimensionless height to instability $\hat{z}_*$, and quantifying the dimensionless turbulent virtual origin $\hat{z}_0 = 2.9 \times 10^5$, along with the turbulent similarity solution (1.35) (Zeldovich, 1937; Schmidt, 1941). The height to instability $\hat{z}_*$ was shown to differ from the virtual origin for the turbulent regime $\hat{z}_0 \neq \hat{z}_*$, indicating the existence of a spatial range over which the plume transitions from laminar to turbulent flow.

Two further sub-conclusions were drawn from the work in chapter 2. The first was that a laminar plume can be initialised at a displaced origin with the laminar similarity solution (1.30)–(1.33), by emulating a point source. This was undertaken using a DNS study, presented in section 2.3.3, which showed the flow approaching the laminar similarity solution, addressing research question 3. The second was to uncover a new scaling of head width in the initial transient flow, showing that the head grows as time $t^{2/3}$, while the stem grows with time as $t^{1/2}$ (Batchelor, 1954; Moses et al., 1993), therefore illustrating that the head region must go unstable before the stem and hence addressing research question 4.

The work in chapter 2 was extended to a range of Prandtl numbers in chapter 3. I performed DNS of plume rise from a point source in an unstratified environment, solving the similarity system (3.9)–(3.12), over a range of Prandtl numbers and found an interpolation formula for height to instability in the studied Pr range at time $t = 1.4 \times 10^7(\kappa^2/F_0)$. This formula is given by

$$z_* \approx \left(\frac{\kappa^3}{F_0}\right)^{1/2} (-0.66Pr^2 + 3.09Pr + 2.04) \times 10^5, \tag{6.2}$$

addressing research question 5. This forms the first prediction of height to instability of plumes generated at a point source in an unstratified environment over a range of Prandtl numbers $Pr \in [0.1, 2.0]$. As the Prandtl number is a description of material properties only, this result significantly generalises the result for $Pr = 1$ to predict the height to instability of plumes for a range of Prandtl numbers covering almost all gases.

Using a constraint on the total buoyancy in the plume, a new theory for the time-dependent initial rise speed of a laminar plume, covering the full spectrum of Prandtl numbers, was developed in section 3.3.3, further addressing research question 4. The head ascent velocity was found to become proportional to $Pr^{-0.25}$ as $Pr \to 0$ and predictions were compared to previous

studies (Kaminski & Jaupart, 2003), showing excellent agreement in the high Pr limit. The results from the DNS were compared to this new theory of initial rise speed in a laminar plume and excellent agreement was found for $Pr = 0.5$, 1.0, and 2.0. For the case $Pr = 0.1$, however, the transition to instability occurred too early to capture almost any laminar plume rise. Finally, the low and high (Worster, 1986) Prandtl number regimes were reviewed and compared to a numerical study of the laminar similarity system (3.9)–(3.12) for $Pr \in [10^{-3}, 10^{2}]$, thereby addressing research question 6.

Extending the plume modelling further in chapter 4, with the introduction of a linearly stratified environment, led to the introduction of another length scale alongside the height to instability, namely the maximum rise height. DNS of plumes generated at a point source in a stratification for $Re \in [10, 3000]$ were performed and, interestingly, a non-monotonic relationship between Reynolds number and rise height was discovered, with a global maximum at $Re \approx 1500$. This result addresses research question 7.

The relative behaviour of the maximum rise height compared to the height to instability z_* for a plume in a stratification was described in section 4.5, addressing research question 8. Using the results of the DNS, the height to instability was shown to be greater than the maximum rise height for plumes with $Re \leq 1500$ and less than the maximum rise height for $Re > 1500$. Comparing the height to instability derived from solving the unstratified laminar similarity system (2.25)–(2.28) with that predicted by the DNS revealed that the laminar similarity solution significantly under-predicts the height to instability in a stratification.

In the low-Re regime, using scaling analysis and boundary layer theory to develop a theory of plume rise in a stratification resulted in a system dependent only on the Prandtl number. Solving this system using a finite differencing scheme for $Pr = 1$ resulted in a prediction for the neutral buoyancy level (NBL) and the rise height, up to a scaling with Re, in low-Re plumes given by

$$NBL_L \approx 0.34 \left(F_0 N^{-3}\right)^{1/4} Re^{1/2}, \tag{6.3}$$

$$H_L \approx 0.52 \left(F_0 N^{-3}\right)^{1/4} Re^{1/2}, \tag{6.4}$$

for stratification frequency N, further addressing research question 7 for the

laminar regime. Making a comparison of this theory with the results of the DNS indicated an excellent agreement for $50 \leq Re \leq 1000$, with a divergence from the prediction for $Re < 50$ which is likely caused by a failure of the boundary layer assumptions in the near aspect ratio one flow.

In the high-Re regime, scaling analysis was used to show that the NBL and the maximum rise height of a turbulent plume as $Re \to \infty$ are constant. This analysis checks the result of Morton et al. (1956), namely that for fully turbulent plumes the NBL is given by and $NBL_T = 3.28\,(F_0/N^3)^{1/4}$ and the rise height is given by $H_T = 4.32\,(F_0/N^3)^{1/4}$. DNS of plumes at $Re > 1500$ illustrate both the NBL and the maximum rise height approaching the values predicted by Morton et al. (1956). Further simulations at higher Reynolds numbers would enable the independent determination of maximum rise height without using the assumption of a parametrisation on the entrainment at the edges of the plume, addressing research question 9.

Finally, in chapter 5, the unstratified theory of height to instability in chapters 2 and 3 was used in an application to aerosol transport in a room. Typical values of height to instability for a number of household objects was shown to be of a significant size within the height of a room. A hybrid laminar-turbulent theory of particle transport was developed using the laminar (1.30)–(1.33) and turbulent (1.35) similarity solutions. Remarkably, a non-monotonic relationship between the time for a particle to reach the ceiling t_H and initial buoyancy flux with two turning points was discovered, providing an answer to research question 10. The first turning point occurs when the plume undergoes instability within the height of the room, thereby introducing turbulent flow and increasing the time to transport a particle to the ceiling. The second occurs when the increasing buoyancy flux causes the vertical velocity in the turbulent regime to become large enough to start decreasing the time taken in transport to the ceiling. The theory also highlights the importance of the laminar regime in particle transport in plumes at low source buoyancy fluxes, predicting that the initial buoyancy flux of a turbulent plume needs to be over two orders of magnitude larger than that of a laminar plume in order to transport a particle to the ceiling in the same amount of time.

6.1 Further work

The work presented in this thesis has provided several interesting insights into the fundamental behaviours of plumes. There still remain a number of unanswered questions, however. In chapter 2, it was found that the height to instability $\hat{z}_*$ from the DNS of (2.17)–(2.20) was insensitive to a changing mesh. In comparison, the investigation into the turbulent plume regime was not feasible on this mesh as the height to instability was too near to the top of the domain. Further work could apply all the methods and practices developed in chapter 2 to further simulations in a larger domain to result in a robust, full description of a plume in an unstratified environment.

DNS of plumes in unstratified environments for a wider range of Prandtl numbers, especially for critical values for air $Pr = 0.7$ and water $Pr = 10$, would provide complete descriptions of plume flow from a point source in a wide range of materials and would allow the improvement of the interpolation formula defined in chapter 3. Eventually, this could lead to a complete description of any plume emanating from a point source in any material. Although not a focus of this study, there have been plenty of studies of varied source conditions, combining the results from those studies with the fundamental description of plumes developed here would further increase the applicability of this work to real-world scenarios.

Furthering the DNS of plumes in a stratification across the full spectrum of Reynolds numbers could be another fruitful avenue of study. Beyond this, the work could be extended into the second dimensionless parameter space to study the effect of Prandtl number on plume rise height in a stratification. As before, this would be very useful for the Prandtl numbers of air and water.

All of these studies were performed with a quiescent ambient. However, there are few applications where this assumption is completely true. The study of height to instability could also be undertaken with a low-level background field of vortices to represent background air disturbances, or with a background wind profile. These adjustments may improve predictions of height to instability for applications such as the straightforward aerosol transport model in chapter 5. This model could also be improved by introducing finite areal sources, as few objects approximate a point source, for example a television would more likely approximate a line plume. Other improve-

ments could include removing the assumption that particles travel along the centreline (Ernst et al., 1996) or introducing a stratification to the model, which could lead to aerosols being transported along a neutral buoyancy level within the room rather than reaching the ceiling.

Appendices

Nomenclature

In this thesis, non-dimensionalisations are performed introducing variables with hats or bars to denote dimensionless variables. Often, these identifying marks are subsequently dropped when the vast majority of the rest of the chapter is in dimensionless form. Unless otherwise stated, the variables in the majority of the text are dimensionless (excluding chapter 5). As a consequence, no distinction is made between dimensional and dimensionless variables in the following.

Variables

ψ	Stokes stream function, page 12.
ϑ	Temperature difference from the environment (distinct from turbulent similarity variable in chapters 2 and 3), page 110.
$\boldsymbol{q}$	Heat flux, page 45.
$\boldsymbol{u}(\boldsymbol{x}, t) = (u, v, w)$	Vector of velocity, in particular w is vertical velocity used frequently in similarity theory, page 6.
$\boldsymbol{x} = (x, y, z)$	Position vector, can also be given in terms of cylindrical coordinates (r, φ, z), page 6.
F	Buoyancy flux, subscripts A and C relate to advective and convective terms, respectively, page 46.
F_0	Initial buoyancy flux, page 7.
M	Momentum flux, page 47.
p	Pressure, page 6.
Q	Volume flux, page 47.
$R = \sqrt{x^2 + y^2 + z^2}$	Spherical radial coordinate, page 7.

$r = \sqrt{x^2 + y^2}$	Cylindrical radial coordinate, page 7.
t	Time, page 6.
$T(\boldsymbol{x}, t)$	Temperature, page 6.

Material properties and physical constants

β	Coefficient of thermal expansion, page 6.
κ	Thermal diffusivity, page 6.
ν	Kinematic viscosity, page 6.
ρ_0	Reference density, page 6.
c_p	Specific heat capacity, page 45.
g	Acceleration due to gravity, page 6.
N	Brunt-Väisälä frequency, page 110.

Plume specifc parameters

$\dot{h}_p$	Rise rate of the plume head, page 99.
$B(t)$	Total buoyancy in the plume, page 99.
z_*	Height to instability, page 72.
z_0	Virtual origin for the turbulent plume regime, page 78.

Scales

$\mathcal{T}$	Intrinsic temperature scale (unstratified), page 47.
τ	Intrinsic time scale (unstratified, with a different value for the stratified theory), page 47.
Θ	Intrinsic temperature difference scale (stratified), page 112.
L	Intrinsic length scale (unstratified, with a different value for the stratified theory), page 47.

Dimensionless parameters

Pe	Péclet number, page 113.
Pr	Prandtl number, page 48.
Re	Reynolds number, page 113.

Similarity variables

α_T	Constant representing temperature Gaussian profile width in the turbulent similarity solution, page 79.
α_w	Constant representing vertical velocity Gaussian profile width in the turbulent similarity solution, page 79.
$\eta = rz^{-1/2}$	Laminar similarity variable, page 12.
ϕ	Turbulent similarity variable for vertical velocity w, page 78.
ϕ_0	Constant representing centreline vertical velocity in the turbulent similarity solution, page 79.
ϑ	Turbulent similarity variable for temperature T (distinct from temperature difference in chapter 4), page 78.
ϑ_0	Constant representing centreline temperature in the turbulent similarity solution, page 79.
$\xi = r/(z - z_0)$	Turbulent similarity variable, page 78.
f	Laminar similarity variable for vertical velocity w, page 13.
h	Laminar similarity variable for temperature T, page 13.
h_0	Constant representing centreline temperature in the laminar similarity solution, page 72.

w_0	Constant representing centreline velocity in the laminar similarity solution, page 72.

Simulation specific parameters

N_{el}	Number of elements in numerical grid, page 56.
N_p	Total number of computational points in numerical grid, page 56.
p	Order of polynomials for spectral element method (SEM), page 56.
w_s, u_s, T_s	Source values of velocity and temperature, page 63.

Particle transport

H	Ceiling height, page 144.
t_c	Time for a particle to reach the ceiling in a hybrid laminar-turbulent plume, page 144.

Appendix A

Running a simulation in Nek5000

To run a simulation using Nek5000, the source code must first be downloaded from the code repository (Fischer et al., 2008). Once installed, there are three main files of importance used to solve the governing equations (2.17)–(2.20) in this thesis, the `.rea` file, the `.usr` file, and the `SIZE` file. This appendix serves as a brief tutorial for running a simulation of a plume in Nek5000.

A.1 The `.rea` file

The `.rea` file is used to house certain simulation parameters, the mesh and boundary data, and a link to a restart file for continuing a simulation from a previous time-step. At the top of the `.rea` file is some simulation parameters such as Reynolds number, Péclet number, time-step, write-step, and Courant number, as well as user-defined parameters. In the code snippet provided, the value of the density is chosen to be 1, and the Reynolds number is defined as 100 (viscosity defines the Reynolds number if the value is negative).

```
****** PARAMETERS *****
  2.60999990      NEKTON VERSION
  3 DIMENSIONAL RUN
        145  PARAMETERS FOLLOW
  1.00000      p001 DENSITY
 -100.000      p002 VISCOS
```

Directly after the parameters section we find the element data, followed by the boundary data (below). It is here that all the information about the mesh and in-built boundary conditions is stored. The element data section can be used, however, to double check the number of elements in the mesh. In the example

case below, there are 54,000 elements in the mesh, given by NEL. The mesh data are created separately using an alternative script which will be discussed later.

```
**MESH DATA** 6 lines are X,Y,Z;X,Y,Z. Columns corners 1-4;5-8
      54000  3        54000 NEL,ldim,NELV
     ELEMENT              1 [    1a]    GROUP     0
  1.000000        4.474500        4.322040       0.9659260
 0.6069408E-10  0.1957846E-09    1.206275       0.5193350
  0.000000        0.000000        0.000000        0.000000
  2.075376        4.743275        4.582087        2.006779
```

Finally, after the mesh data at the end of the .rea file, there is some further information. It is here that a restart file can be included. This ability to restart enables the simulation to be started from a previous time step (of the same mesh), rather than starting from zero. This is important for many researchers using high performance computing (HPC), as simulations are often limited to a certain time to ensure that all users have equal access to the machine. A typical DNS run of a plume in this thesis can take up to ten restarts, requiring multiple submissions to the HPC. This simulation is restarted from the file plume0.restart which is saved in the case directory.

```
           1  PRESOLVE/RESTART OPTIONS  *****
plume0.restart
```

A.2 The SIZE file

The SIZE file contains runtime parameters integral to the running of the simulation. It is here that the polynomial order of the spectral element mesh, the dimension, and the decomposition onto separate cores (for running in parallel, critical for use in HPC) is set. In this example, the simulation is three dimensional, the polynomial order of the simulation is set to 7 (given by lx1 - 1), the number of elements is set to 54,000, and the simulation will be decomposed to run as 480 processes.

```
      integer ldim,lx1,lxd,lx2,lx1m,lelg,lelt,lpmin,lpmax,ldimt

      ! BASIC
      parameter (ldim=3)      ! domain dimension (2 or 3)
      parameter (lx1=8)
```

```
      parameter (lxd=12)      ! p-order for over-integration
      parameter (lx2=lx1-2)   ! p-order for pressure

      parameter (lelg=54000) ! max total number of elements
      parameter (lpmin=480)   ! min MPI ranks
      parameter (lpmax=480)   ! max MPI ranks
      parameter (ldimt=2)     ! max auxiliary fields

      ! INTERNALS
      include 'SIZE.inc'
```

A.3 The `.usr` file

The `.usr` file is used to specify material dependent properties, set source and forcing terms, set initial and boundary conditions, set any operations that may run each time-step, and modify the spectral element mesh. It is in this file that splines representing the source (2.42) and the sponge layer condition (2.35) are set. It consists of a number of different subroutines, each performing a different task. User-defined parameters from the `.rea` file can be read into this file by defining `param(i)`, where `i` is the index of the parameter. The `uservp` subroutine is used to specify solution dependent material properties, in the code snippet included the Reynolds number is artificially modified to damp turbulent eddies that leave the domain and cause instabilities at the boundaries.

```
      subroutine uservp (ix,iy,iz,eg)
      include 'SIZE'
      include 'TOTAL'
      include 'NEKUSE'

      real r_min,r_max,z_min,z_max
      common /domsizes/ r_min,r_max,z_min,z_max

c.....Reynolds number in the Sponge region
      responge = param(3)
c.....Fluid density
      utrans = 1.0

      scoefr_z = 10/(z_max-z_min)
      scoefr_r = 20/(r_max-r_min)
```

```
      radial = (x**2 + y**2)**0.5

c.....Viscosity (ifield = 1 specifies velocity)
      if(ifield.eq.1)then

        udiff = param(2)
     $       +(1./responge)*(1.+derf(scoefr_z*(z - z_max)))
     $       +(1./responge)*(1.+derf(scoefr_r*(radial - r_max)))

c.....Conductivity (ifield > 1: temperature or passive scalar)
      else if(ifield.gt.1)then

        udiff = param(8)
     $       +(1./responge)*(1.+derf(scoefr_z*(z - z_max)))
     $       +(1./responge)*(1.+derf(scoefr_r*(radial - r_max)))

      endif

      return
      end
```

The `userf` and `userq` subroutines are used to set the source terms for the momentum and temperature equations, respectively. In the code in `userq` the commented lines represent the case for the stratified simulations.

```
      subroutine userf  (ix,iy,iz,eg)
      include 'SIZE'
      include 'TOTAL'
      include 'NEKUSE'

      ffx = 0.0
      ffy = 0.0
      ffz = temp

      return
      end
```

```
      subroutine userq  (ix,iy,iz,eg)
      include 'SIZE'
      include 'TOTAL'
      include 'NEKUSE'

c      real verVel
c      integer e,eg
c      e = gllel(eg)
```

```
      qvol = 0.0

c      vertical_velocity = vz(ix,iy,iz,e)
c      if(ifield.eq.2)then
c       qvol = -verVel
c      endif

      return
      end
```

The `userchk` subroutine is used by the user to specify any operations that are required every time-step. For example, some initial research (that did not make it into this thesis) included running a Lagrangian particle tracking code to track the spread and dispersal of passive-tracers in the flow. The example shown in the following code-snippet calls an azimuthal averaging routine on each write-step.

```
      subroutine userchk
      include 'SIZE'
      include 'TOTAL'
      include 'NEKUSE'

c.....Do azimuthal averages.
      if (mod(istep,iostep).eq.0) then
          if (nid.eq.0) write(6,*) 'Get azimuthal average...'
          call azimuthal_average(istep/iostep)
          if (nid.eq.0) write(6,*) 'Done.'
      endif

      return
      end
```

In the `userbc` and `useric` subroutines the user-defined boundary and initial conditions are set. It is in `userbc` that the splines representing the source (2.42) are read in and specified. As the code for that is fairly long, however, included is a simple top-hat profile for the source. In the `useric` subroutine shown, the initial state is set to zero (this is overwritten if a restart file is included in the `.rea` file).

```
      subroutine userbc (ix,iy,iz,iside,eg)
      include 'SIZE'
      include 'TOTAL'
      include 'NEKUSE'
```

```
      ux=0.0
      uy=0.0
      uz=0.0
      temp=0.0

      r = (x**2 + y**2) ** 0.5
      radius = param(105)

c.....Source condition
      if ( z.eq.z_min ) then
        if ( R.lt.radius ) then

          uz=1.0
          temp=1.0

        endif
      endif

      return
      end
```

```
      subroutine useric (ix,iy,iz,ieg)
      include 'SIZE'
      include 'TOTAL'
      include 'NEKUSE'

      ux=0.0
      uy=0.0
      uz=0.0
      temp=0.0

      return
      end
```

Finally, the `usrdat` subroutines are used to modify the spectral element mesh or initialise case or user specific data. Further subroutines such as those for azimuthal averaging or Lagrangian particle tracking are included on the end of this file, to be called from `userchk`.

A.4 Meshing

Meshing in Nek5000 can be done using a tool called `genbox` which takes a `.box` file as input which describes simple regions and the boundary conditions applied at the edge of those regions. This is a useful tool if modelling certain simple shapes such as a box or a pipe.

In this project, an alternative tool called `pretex` (combined with `genbox`) is used to build the mesh. This tool is used to generate a cylindrical domain by connecting circular outer rings onto an interior square-shaped mesh. This technique is beneficial as it removes degenerate cells at the very centre of the mesh, which otherwise would consist of triangles (degenerate squares) all pointing into the centre of the cylinder.

The output of `pretex` is an `.rea` file in which relevant parameters should be filled in the above sections. Following the generation of the mesh using `pretex`, the mesh is modified by making use of a script that fans the mesh into a cone-shape and subsequently 'smooths' the spectral elements to reduce the aspect ratios of each element.

A.5 Compiling and running

Once the simulation files have been set up correctly, the environment must first be compiled before it can be run. Initially the spectral element mesh is decomposed onto each processor using `genmap`. Subsequently, to compile the case, the command `makenek plume` is used, where `plume` is the name given to each of the files in the case directory (e.g. `plume.rea` and `plume.usr` (`SIZE` is a complete file name and has no prefix)).

Finally, to run the simulation the command `nekmpi plume 480` is used, where `480` is the number of cores on which to run the simulation in parallel (this command will often be in a submission script for use in HPC).

A.6 Post-processing

As the simulation runs, files of the form `plume0.f00001` are generated and numbered incrementally at each write-step. After the simulation data is produced, it can be read into other programs in order to interpret the results - this is called post-processing. For example, to generate figure 2.9, each data file is read into Python and subsequently reformatted from element data to coordinate data, a vertical slice in the xz-plane is extracted and a filled contour plot is produced. To generate the lower plots in figure 2.10, the azimuthally averaged data is read into MATLAB and the vertical line in the z-direction at the centre of the domain is extracted and plotted against time. To generate figure 2.13 the azimuthally averaged data files are again read into MATLAB and time averaged to compute the standard deviation over that period of time.

A.7 Data management

It is important to monitor the size of each data file and the frequency of the write-step. By the nature of DNS, each data file can sizeable. If the write-step is too low this can result in generating quite a serious amount of data in a short space of time. A single Nek5000 simulation, at 54,000 elements with a polynomial order of 7, on 480 cores could quite easily produce 80 terabytes of data in 48 hours. When running multiple simulations for parameter or mesh sensitivity studies, it is therefore important to be aware of the storage space available and to only write data at the frequency required.

Appendix B

Finite differencing scheme for solving partial differential equations

In this appendix, the method used for modelling the axisymmetric boundary layer equations for plume flow in a stratification (4.29)–(4.32) is described. Firstly, the process is introduced by considering a simple differential equation such as the diffusion equation in section B.1, and subsequently the case fo the axisymmetric boundary layer equations is considered in section B.2.

B.1 The Crank-Nicolson method for solving the heat equation

The Crank-Nicolson method is a finite difference method used for numerically solving partial differential equations. It involves making the approximation of both first and second order derivatives in the following way:

$$\frac{\mathrm{d}u}{\mathrm{d}t} \approx \frac{u^{n+1} - u^n}{\Delta t}, \qquad \frac{\mathrm{d}^2u}{\mathrm{d}x^2} \approx \frac{u_{j+1} - 2u_j + u_{j-1}}{(\Delta x)^2}, \tag{B.1}$$

where n and j represent discrete steps in time and space, respectively. A simple linear diffusion problem in one spatial dimension, often called the heat equation, for $u(x,t)$ with $x \in [x_0, x_L]$ and $t \geq 0$, has the form

$$\frac{\mathrm{d}u}{\mathrm{d}t} = c\frac{\mathrm{d}^2u}{\mathrm{d}x^2}, \tag{B.2}$$

for some constant c, with Dirichlet and symmetry boundary conditions

$$\frac{\mathrm{d}u(x_L,t)}{\mathrm{d}x} = 0, \quad \text{and} \quad u(x_R,t) = u_R, \tag{B.3}$$

at the left and right boundaries, respectively.

To solve this numerically, the approximations in (B.1) are substituted into the governing equations (B.2). The discretised equations can be solved either explicitly or implicitly, the former involves representing the second order derivative at time n, the latter at $n+1$. These two methods are also known as the forward Euler (explicit), or backward Euler (implicit) method. The Crank-Nicolson method takes both of these methods and averages them. Then (B.2) becomes

$$\frac{u_j^{n+1} - u_j^n}{\Delta t} = \frac{c}{2}\left(\frac{u_{j+1}^{n+1} - 2u_j^{n+1} + u_{j-1}^{n+1}}{(\Delta x)^2} + \frac{u_{j+1}^{n} - 2u_j^{n} + u_{j-1}^{n}}{(\Delta x)^2}\right). \tag{B.4}$$

Grouping terms with time equal to $n+1$ on the left hand side, and n on the right, while letting $\alpha = c\Delta t/(\Delta x)^2$, results in,

$$-\alpha u_{j+1}^{n+1} + (2+2\alpha)u_j^{n+1} - \alpha u_{j-1}^{n+1} = \alpha u_{j+1}^{n} + (2-2\alpha)u_j^{n} + \alpha u_{j-1}^{n}. \tag{B.5}$$

This system can then be solved using the matrix equation,

$$A\boldsymbol{u}^{n+1} = B\boldsymbol{u}^{n}, \tag{B.6}$$

for

$$A = \begin{pmatrix} 1 & 0 & 0 & 0 & 0 & \cdots & 0 & 0 & 0 & 0 \\ -\alpha & 2+2\alpha & -\alpha & 0 & 0 & \cdots & 0 & 0 & 0 & 0 \\ 0 & -\alpha & 2+2\alpha & -\alpha & 0 & \cdots & 0 & 0 & 0 & 0 \\ 0 & 0 & -\alpha & 2+2\alpha & -\alpha & \cdots & 0 & 0 & 0 & 0 \\ \vdots & \vdots & \vdots & \vdots & \vdots & \ddots & \vdots & \vdots & \vdots & \vdots \\ 0 & 0 & 0 & 0 & 0 & \cdots & -\alpha & 2+2\alpha & -\alpha & 0 \\ 0 & 0 & 0 & 0 & 0 & \cdots & 0 & -\alpha & 2+2\alpha & -\alpha \\ 0 & 0 & 0 & 0 & 0 & \cdots & 0 & 0 & 0 & 1 \end{pmatrix},$$

$$B = \begin{pmatrix} 0 & 1 & 0 & 0 & 0 & \cdots & 0 & 0 & 0 & 0 \\ \alpha & 2-2\alpha & \alpha & 0 & 0 & \cdots & 0 & 0 & 0 & 0 \\ 0 & \alpha & 2-2\alpha & \alpha & 0 & \cdots & 0 & 0 & 0 & 0 \\ 0 & 0 & \alpha & 2-2\alpha & \alpha & \cdots & 0 & 0 & 0 & 0 \\ \vdots & \vdots & \vdots & \vdots & \vdots & \ddots & \vdots & \vdots & \vdots & \vdots \\ 0 & 0 & 0 & 0 & 0 & \cdots & \alpha & 2-2\alpha & \alpha & 0 \\ 0 & 0 & 0 & 0 & 0 & \cdots & 0 & \alpha & 2-2\alpha & \alpha \\ 0 & 0 & 0 & 0 & 0 & \cdots & 0 & 0 & 0 & 1 \end{pmatrix},$$

$$\boldsymbol{u}^n = \begin{pmatrix} u_0^n & u_1^n & u_2^n & u_3^n & \cdots & u_{m-1}^n & u_m^n & u_{m+1}^n \end{pmatrix}^T,$$

for m points in space, where u_0^n and u_{m+1}^n represent the value of u at each boundary. The first line of A, B represents the symmetry boundary condition $u_0^{n+1} = u_1^n$, and the last line represents the Dirichlet condition $u_{m+1}^{n+1} = u_R^n$.

B.2 Solving the axisymmetric boundary layer equations using a theta-scheme

The axisymmetric boundary layer equations for a plume generated from a point source (4.29)–(4.32) are given by

$$u\frac{\partial w}{\partial r} + w\frac{\partial w}{\partial z} = \frac{1}{Re}\left(\frac{1}{r}\frac{\partial}{\partial r}\left(r\frac{\partial w}{\partial r}\right)\right) + \vartheta, \tag{B.7a}$$

$$\frac{1}{r}\frac{\partial (ru)}{\partial r} + \frac{\partial w}{\partial z} = 0, \tag{B.7b}$$

$$u\frac{\partial \vartheta}{\partial r} + w\frac{\partial \vartheta}{\partial z} = \frac{1}{Pe}\left(\frac{1}{r}\frac{\partial}{\partial r}\left(r\frac{\partial \vartheta}{\partial r}\right)\right) - w, \tag{B.7c}$$

with symmetry conditions

$$\frac{\partial w}{\partial r} = 0, \qquad \frac{\partial T}{\partial r} = 0, \qquad u = 0, \qquad \text{at } r = 0, \tag{B.8}$$

far-field conditions

$$w \to 0, \qquad T \to 0, \qquad \text{as } r, z \to \infty, \tag{B.9}$$

and source buoyancy flux condition

$$2\pi \int_0^\infty r(\vartheta + z) w \, \mathrm{d}r = 1. \tag{B.10}$$

It can be seen that these equations are in a similar form to the heat equation, thus a similar solution method can be used to find their solution. By treating height z as the time variable from section B.1, the system can be solved in a similar way. Firstly, discretisations of the relevant derivatives are chosen to be

$$\frac{\partial w}{\partial z} \approx \frac{w_j^k - w_j^{k-1}}{\Delta z}, \tag{B.11a}$$

$$\frac{\partial w}{\partial r} \approx \phi \frac{w_{j+1}^k - w_{j-1}^k}{2\Delta r} + (1-\phi)\frac{w_{j+1}^{k-1} - w_{j-1}^{k-1}}{2\Delta r}, \tag{B.11b}$$

$$\frac{\partial^2 w}{\partial r^2} \approx \phi \frac{w_{j+1}^k - 2w_j^k + w_{j-1}^k}{\Delta r^2} + (1-\phi)\frac{w_{j+1}^{k-1} - 2w_j^{k-1} + w_{j-1}^{k-1}}{\Delta r^2}, \tag{B.11c}$$

where replacing ϑ for w produces the same discretisations for temperature difference. The parameter ϕ (often given by ϑ but chosen here as ϕ so as not to confuse with temperature difference) is the theta-scheme parameter which controls how explicit or implicit the equations are. This is a generalisation from the previous section where the Crank-Nicolson method was used, which is equivalent to $\phi = 0.5$. Focusing on the momentum equation (B.7a) for now (as the process is almost identical for the temperature difference equation), the equation is rearranged by expanding the bracket in the diffusion term to write

$$\left(u - \frac{1}{Re}\frac{1}{r}\right)\frac{\partial w}{\partial r} + w\frac{\partial w}{\partial z} = \frac{1}{Re}\frac{\partial^2 w}{\partial r^2} + \vartheta. \tag{B.12}$$

Values of u and w outside of derivatives also need to be discretised, and are

chosen to be

$$w \approx \phi w_j^k + (1-\phi) w_j^{k-1}, \tag{B.13a}$$
$$u \approx \phi u_j^k + (1-\phi) u_j^{k-1}, \tag{B.13b}$$
$$\vartheta \approx \phi \vartheta_j^k + (1-\phi) \vartheta_j^{k-1}. \tag{B.13c}$$

In order to prevent too much over-cluttering of the equations, parameters

$$\alpha = \frac{1}{Re}\frac{\Delta z}{\Delta r}, \tag{B.14}$$
$$\bar{\alpha} = \frac{\Delta z}{2\Delta r}\left(\phi u_j^k + (1-\phi) u_j^{k-1} - \frac{1}{Re}\frac{1}{r_i}\right), \tag{B.15}$$
$$\alpha^* = \phi w_j^k + (1-\phi) w_j^{k-1}, \tag{B.16}$$

are introduced. The discretisations (B.11) and (B.13) are substituted into (B.12) to find

$$\begin{aligned} &\bar{\alpha}\left(\phi\left(w_{j+1}^k - w_{j-1}^k\right) + (1-\phi)\left(w_{j+1}^{k-1} - w_{j-1}^{k-1}\right)\right) + \alpha^*\left(w_j^k - w_j^{k-1}\right) \\ &\quad = \alpha\left(\phi\left(w_{j+1}^k - 2w_j^k + w_{j-1}^k\right) + (1-\phi)\left(w_{j+1}^{k-1} - 2w_j^{k-1} + w_{j-1}^{k-1}\right)\right) \\ &\qquad + \Delta z\left(\phi\vartheta_j^k + (1-\phi)\vartheta_j^{k-1}\right). \end{aligned} \tag{B.17}$$

Then, rearranging so that k terms are on the left-hand side and $k-1$ terms on the right, and collating j terms on each side, the equation in (B.12) can be written in matrix form (like in section B.1). The tri-diagonal slice of A and B are hence given by

$$A = \begin{pmatrix} \phi(-\bar{\alpha} - \alpha) & \alpha^* + 2\phi\alpha & \phi(\bar{\alpha} - \alpha) \end{pmatrix},$$
$$B = \begin{pmatrix} (1-\phi)(\bar{\alpha} + \alpha) & \alpha^* - 2(1-\phi)\alpha & (1-\phi)(-\bar{\alpha} + \alpha) \end{pmatrix}.$$

The entries of A and B at the zero Neumann boundaries are found by noting that the approximation of the derivative at the boundary is given by (B.11b) and that setting this to zero (ignoring the theta-scheme) results in $w_2^k = w_0^k$ (and similarly for the right-hand side). Substituting this into (B.17) results in the diagonal and triangular entry, given by

$$A_{1,1} = \alpha^* + 2\phi\alpha, \qquad A_{1,2} = -2\phi\alpha, \tag{B.18}$$
$$B_{1,1} = \alpha^* - 2(1-\phi)\alpha \qquad B_{1,2} = -2(1-\phi)\alpha, \tag{B.19}$$

for the left-hand boundary and

$$A_{n,n} = \alpha^* + 2\phi\alpha, \qquad A_{n,n-1} = -2\phi\alpha, \tag{B.20}$$

$$B_{n,n} = \alpha^* - 2(1-\phi)\alpha \qquad B_{n,n-1} = -2(1-\phi)\alpha, \tag{B.21}$$

for the right-hand boundary. The values of vertical velocity and temperature difference at time-step k are computed by solving the matrix inversion problem

$$\boldsymbol{w}^k = A^{-1}\left(B\boldsymbol{w}^{k-1} + \Delta z\left(\phi\boldsymbol{\vartheta}^k + (1-\phi)\boldsymbol{\vartheta}^{k-1}\right)\right), \tag{B.22a}$$

$$\boldsymbol{\vartheta}^k = A^{-1}\left(B\boldsymbol{\vartheta}^{k-1} - \Delta z\left(\phi\boldsymbol{w}^k + (1-\phi)\boldsymbol{w}^{k-1}\right)\right). \tag{B.22b}$$

Before this equation can be solved, an approximation for the horizontal velocity u must be found. This is done by discretising the mass conservation equation

$$\frac{\partial(ru)}{\partial r} + \frac{\partial(rw)}{\partial z} = 0, \tag{B.23}$$

with similar approximations to (B.11a) and (B.11b), such that

$$u_j^k = \frac{1}{r_j}\Bigg(r_{j-1}u_{j-1}^k - \frac{1}{\phi}\Big(\alpha_u\Big(\phi\left(r_j w_j^k - r_{j-1}w_{j-1}^k\right) + (1-\phi)\left(r_j w_j^{k-1} - r_{j-1}w_{j-1}^{k-1}\right)\Big)\Big)\Bigg), \tag{B.24}$$

where $\alpha_u = \Delta r/\Delta z$. The system (B.22) and (B.24) is then solved for height step k, given previous knowledge of height step $k-1$. The initial conditions for w, u, and ϑ are set using the splines (4.27) to represent the unstratified similarity solution (2.25)–(2.28), such that the source buoyancy flux condition (B.10) is satisfied.

Bibliography

Atkinson K., 1991, *"An introduction to numerical analysis"*. John wiley & sons

Batchelor G., 1954, *"Heat convection and buoyancy effects in fluids"*, Quarterly Journal of the Royal Meteorological Society, 80, 339

Bejan A., 2013, *"Convection heat transfer"*. John Wiley & Sons

Bhagat R. K., Wykes M. D., Dalziel S. B., Linden P., 2020, *"Effects of ventilation on the indoor spread of COVID-19"*, Journal of Fluid Mechanics, 903

Bhamidipati N., Woods A. W., 2017, *"On the dynamics of starting plumes"*, Journal of Fluid Mechanics, 833

Boström E., 2015, *"Investigation of outflow boundary conditions for convection-dominated incompressible fluid flows in a spectral element framework"*

Boyd J. P., 2001, *"Chebyshev and Fourier spectral methods"*. Courier Corporation

Brand R., Lahey F., 1967, *"The heated laminar vertical jet"*, Journal of Fluid Mechanics, 29, 305

Carazzo G., Kaminski E., Tait S., 2006, *"The route to self-similarity in turbulent jets and plumes"*, Journal of Fluid Mechanics, 547, 137

Carazzo G., Kaminski E., Tait S., 2008, *"On the rise of turbulent plumes: Quantitative effects of variable entrainment for submarine hydrothermal vents, terrestrial and extra terrestrial explosive volcanism"*, Journal of Geophysical Research: Solid Earth, 113

Chakravarthy R., Lesshafft L., Huerre P., 2018, *"Global stability of buoyant jets and plumes"*, Journal of Fluid Mechanics, 835, 654

Courant R., 1943, *"Variational methods for the solution of problems of equilibrium and vibrations"*, Bulletin of the American Mathematical Society, 49, 1

Craven B. A., Settles G. S., 2006, *"A computational and experimental investigation of the human thermal plume"*, Journal of Fluids Engineering, 128, 1251

Davaille A., Limare A., Touitou F., Kumagai I., Vatteville J., 2011, *"Anatomy of a laminar starting thermal plume at high Prandtl number"*, Experiments in Fluids, 50, 285

Devenish B., Rooney G., Thomson D., 2010, *"Large-eddy simulation of a buoyant plume in uniform and stably stratified environments"*, Journal of Fluid Mechanics, 652, 75

Deville M. O., Fischer P. F., Fischer P. F., Mund E., et al., 2002, *"High-order methods for incompressible fluid flow"*. Vol. 9, Cambridge University Press

Dombrowski C., Lewellyn B., Pesci A. I., Restrepo J. M., Kessler J. O., Goldstein R. E., 2005, *"Coiling, entrainment, and hydrodynamic coupling of decelerated fluid jets"*, Physical Review Letters, 95, 184501

Ernst G. G., Sparks R. S. J., Carey S. N., Bursik M. I., 1996, *"Sedimentation from turbulent jets and plumes"*, Journal of Geophysical Research: Solid Earth, 101, 5575

Ezhova E., Cenedese C., Brandt L., 2017, *"Dynamics of a turbulent buoyant plume in a stratified fluid: An idealized model of subglacial discharge in Greenland Fjords"*, Journal of Physical Oceanography, 47, 2611

Fabregat Tomàs A., Poje A. C., Özgökmen T. M., Dewar W. K., 2016, *"Effects of rotation on turbulent buoyant plumes in stratified environments"*, Journal of Geophysical Research: Oceans, 121, 5397

Fischer P., Lottes J., Tufo H., 2007, Technical report, *"Nek5000"*. Argonne National Lab.(ANL), Argonne, IL (United States)

Fischer P. F., Lottes J. W., Kerkemeier S. G., 2008, *"Nek5000 web page"*

Fischer P., Lottes J., Kerkemeier S., Marin O., Heisey K., Obabko E., Merzari E., Peet Y., 2016, *"Nek5000 user documentation"*, Argonne National Laboratory, Lemont, IL, Report No. ANL/MCS-TM-351

Fox D. G., 1970, *"Forced plume in a stratified fluid"*, Journal of Geophysical Research, 75, 6818

Galántai A., 2000, *"The theory of Newton's method"*, Journal of Computational and Applied Mathematics, 124, 25

George Jr W. K., Alpert R. L., Tamanini F., 1977, *"Turbulence measurements in an axisymmetric buoyant plume"*, International Journal of Heat and Mass Transfer, 20, 1145

Gill A. E., 1982, *"Atmosphere-ocean dynamics"*. Vol. 30, Academic Press

Henderson S. B., Burkholder B., Jackson P. L., Brauer M., Ichoku C., 2008, *"Use of MODIS products to simplify and evaluate a forest fire plume dispersion model for PM10 exposure assessment"*, Atmospheric Environment, 42, 8524

Hewett T., Fay J., Hoult D., 1971, *"Laboratory experiments of smokestack plumes in a stable atmosphere"*, Atmospheric Environment (1967), 5, 767

Hewitt R. E., Duck P. W., 2011, *"Pulsatile jets"*, Journal of fluid mechanics, 670, 240

Hunt G., Kaye N., 2001, *"Virtual origin correction for lazy turbulent plumes"*, Journal of Fluid Mechanics, 435, 377

Hunt G., Kaye N., 2005, *"Lazy plumes"*, Journal of Fluid Mechanics, 533, 329

Hunt G., Van den Bremer T., 2011, *"Classical plume theory: 1937–2010 and beyond"*, IMA journal of applied mathematics, 76, 424

Jiang X., Luo K., 2000, *"Direct numerical simulation of the puffing phenomenon of an axisymmetric thermal plume"*, Theoretical and Computational Fluid Dynamics, 14, 55

Johnson C. G., Hogg A. J., Huppert H. E., Sparks R. S. J., Phillips J. C., Slim A. C., Woodhouse M. J., 2015, *"Modelling intrusions through quiescent and moving ambients"*, Journal of Fluid Mechanics, 771, 370

Jordan O. H., Rooney G. G., Devenish B. J., van Reeuwijk M., 2022, *"Under pressure: turbulent plumes in a uniform crossflow"*, Journal of Fluid Mechanics, 932

Kaminski E., Jaupart C., 2003, *"Laminar starting plumes in high-Prandtl-number fluids"*, Journal of Fluid Mechanics, 478, 287

Kotsovinos N. E., 2000, *"Axisymmetric submerged intrusion in stratified fluid"*, Journal of Hydraulic Engineering, 126, 446

Lesshafft L., 2015, *"Linear global stability of a confined plume"*, Theoretical and Applied Mechanics Letters, 5, 126

Linden P. F., 1999, *"The fluid mechanics of natural ventilation"*, Annual Review of Fluid Mechanics, 31, 201

Liu F., Zhao Y., Liu Y.-Q., Liu Y., Sun J., Huang M.-M., Liu Y., Dong G.-H., 2014, *"Asthma and asthma related symptoms in 23,326 Chinese children in relation to indoor and outdoor environmental factors: the Seven Northeastern Cities (SNEC) Study"*, Science of the Total Environment, 497, 10

Lombardi M., Caulfield C.-C. P., Cossu C., Pesci A. I., Goldstein R. E., 2011, *"Growth and instability of a laminar plume in a strongly stratified environment"*, Journal of Fluid Mechanics, 671, pp

Loper D. E., 1991, *"Mantle plumes"*, Tectonophysics, 187, 373

Loper D. E., Stacey F. D., 1983, *"The dynamical and thermal structure of deep mantle plumes"*, Physics of the Earth and Planetary Interiors, 33, 304

López Moscat J. M., Marqués Truyol F., 2013, *"Instability of plumes driven by localized heating"*, Journal of Fluid Mechanics, 736, 616

Maxworthy T., 1999, *"The flickering candle: transition to a global oscillation in a thermal plume"*, Journal of Fluid Mechanics, 390, 297

Mirajkar H. N., Balasubramanian S., 2017, *"Effects of varying ambient stratification strengths on the dynamics of a turbulent buoyant plume"*, Journal of Hydraulic Engineering, 143, 04017013

Mitchell M., 1996, *"An introduction to genetic algorithms mit press"*, Cambridge, Massachusetts. London, England, 1996

Morton B., 1959, *"Forced plumes"*, Journal of Fluid Mechanics, 5, 151

Morton B., 1967, *"Entrainment models for laminar jets, plumes, and wakes"*, The Physics of Fluids, 10, 2120

Morton B., Middleton J., 1973, *"Scale diagrams for forced plumes"*, Journal of Fluid Mechanics, 58, 165

Morton B., Taylor G., Turner J., 1956, in Proceedings of the Royal Society of London A: Mathematical, Physical and Engineering Sciences. pp 1–23

Moses E., Zocchi G., Libchaberii A., 1993, *"An experimental study of laminar plumes"*, Journal of Fluid Mechanics, 251, 581

Nakagome H., Hirata M., 1977, in Proc. 1976 ICHMT Seminar on Turbulent Buoyant Convection. pp 361–372

Navier M., 1827, *"Mémoire sur les lois du mouvement des fluides"*, Mém. de l'Acad. d. Sci, 6, 389

Oden J. T., 1991, *"Finite elements: Introduction"*, Handbook of Numerical Analysis Volime II: Finite Element Methods (Part1)

Offermans N., et al., 2016, in Proceedings of the Exascale Applications and Software Conference 2016. pp 1–10

Pant C. S., Bhattacharya A., 2016, *"A viscous sponge layer formulation for robust large eddy simulation of thermal plumes"*, Computers & Fluids, 134, 177

Papanicolaou P. N., List E. J., 1988, *"Investigations of round vertical turbulent buoyant jets"*, Journal of Fluid Mechanics, 195, 341

Patera A. T., 1984, *"A spectral element method for fluid dynamics: laminar flow in a channel expansion"*, Journal of Computational Physics, 54, 468

Pegler S. S., Ferguson D. J., 2021, *"Rapid heat discharge during deep-sea eruptions generates megaplumes and disperses tephra"*, Nature Communications, 12, 1

Peplinski A., Schlatter P., Fischer P., Henningson D. S., 2014, in , Spectral and High Order Methods for Partial Differential Equations-ICOSAHOM 2012. Springer, pp 349–359

Pham M., Plourde F., Doan K., 2007, *"Direct and large-eddy simulations of a pure thermal plume"*, Physics of Fluids, 19, 125103

Plourde F., Pham M. V., Kim S. D., Balachandar S., 2008, *"Direct numerical simulations of a rapidly expanding thermal plume: structure and entrainment interaction"*, Journal of Fluid Mechanics, 604, 99

Priestley C., Ball F., 1955, *"Continuous convection from an isolated source of heat"*, Quarterly Journal of the Royal Meteorological Society, 81, 144

Pyle D. M., 1995, *"Mass and energy budgets of explosive volcanic eruptions"*, Geophysical Research Letters, 22, 563

van Reeuwijk M., Craske J., 2015, *"Energy-consistent entrainment relations for jets and plumes"*, Journal of Fluid Mechanics, 782, 333

van Reeuwijk M., Salizzoni P., Hunt G. R., Craske J., 2016, *"Turbulent transport and entrainment in jets and plumes: A DNS study"*, Physical Review Fluids, 1, 074301

Roberts G., 1977, *"Fast viscous convection"*, Geophysical & Astrophysical Fluid Dynamics, 8, 197

Rooney G., Devenish B., 2014, *"Plume rise and spread in a linearly stratified environment"*, Geophysical & Astrophysical Fluid Dynamics, 108, 168

Rouse H., Yih C., Humphreys H., 1952, *"Gravitational convection from a boundary source"*, Tellus, 4, 201

Scase M., Hewitt R., 2012, *"Unsteady turbulent plume models"*, Journal of fluid mechanics, 697, 455

Schlichting H., Gersten K., 2003, *"Boundary-layer theory"*. Springer Science & Business Media

Schmidt W., 1941, *"Turbulente ausbreitung eines stromes erhitzter luft"*, ZAMM-Journal of Applied Mathematics and Mechanics/Zeitschrift für Angewandte Mathematik und Mechanik, 21, 265

Shabbir A., George W. K., 1994, *"Experiments on a round turbulent buoyant plume"*, Journal of Fluid Mechanics, 275, 1

Shampine L. F., Reichelt M. W., 1997, *"The MATLAB ODE suite"*, SIAM Journal on Scientific Computing, 18, 1

Skeel R. D., Berzins M., 1990, *"A method for the spatial discretization of parabolic equations in one space variable"*, SIAM Journal on Scientific and Statistical Computing, 11, 1

Sparks R., Carey S., Sigurdsson H., 1991, *"Sedimentation from gravity currents generated by turbulent plumes"*, Sedimentology, 38, 839

Speer K. G., Rona P. A., 1989, *"A model of an Atlantic and Pacific hydrothermal plume"*, Journal of Geophysical Research: Oceans, 94, 6213

Stokes G. G., 1849, *"On the theories of the internal friction of fluids in motion, and of the equilibrium and motion of elastic solids"*, Trans. Cambr. Phil. Soc., 8, 287

Sutherland B. R., Hong Y. S. D., 2016, *"Sedimentation from particle-bearing plumes in a stratified ambient"*, Physical Review Fluids, 1, 074302

Tang J., Li Y., Eames I., Chan P., Ridgway G., 2006, *"Factors involved in the aerosol transmission of infection and control of ventilation in healthcare premises"*, Journal of Hospital Infection, 64, 100

Turner J., 1962, *"The 'starting plume'in neutral surroundings"*, Journal of Fluid Mechanics, 13, 356

Vatteville J., Van Keken P. E., Limare A., Davaille A., 2009, *"Starting laminar plumes: Comparison of laboratory and numerical modeling"*, Geochemistry, Geophysics, Geosystems, 10

Whittaker R. J., Lister J. R., 2006, *"Steady axisymmetric creeping plumes above a planar boundary. Part 1. A point source"*, Journal of Fluid Mechanics, 567, 361

Woodhouse M., Hogg A., Phillips J., Sparks R., 2013, *"Interaction between volcanic plumes and wind during the 2010 Eyjafjallajökull eruption, Iceland"*, Journal of Geophysical Research: Solid Earth, 118, 92

Worster M. G., 1986, *"The axisymmetric laminar plume: asymptotic solution for large Prandtl number"*, Studies in Applied Mathematics, 75, 139

Wriggers P., 2008, *"Nonlinear finite element methods"*. Springer Science & Business Media

Xue N., Khodaparast S., Stone H. A., 2019, *"Fountain mixing in a filling box at low Reynolds numbers"*, Physical Review Fluids, 4, 024501

Yih C.-s., 1951, *"Comparative study of momentum transfer, heat transfer, and vapor transfer. Part III, Free convection, A"*, PhD thesis, Colorado State University. Libraries

Yih C., 1977, *"Fluid Mechanics: A Concise Introduction to the Theory. West River"*. Ann Arbor

Zeldovich Y. B., 1937, *"The asymptotic laws of freely-ascending convective flows"*, Zhur. Eksper. Teor. Fiz, 7, 1463

Zeldovich Y. B., 1992, *"Selected Works of Yakov Borisovich Zeldovich, Volume I: Chemical Physics and Hydrodynamics"*. Princeton University Press

Zimin V., Frik P., 1977, *"Averaged temperature fields in asymmetrical turbulent streams over localized heat sources"*, Fluid Dynamics, 12, 335